



## THESIS APPROVAL

### GRADUATE SCHOOL, KASETSART UNIVERSITY

Doctor of Philosophy (Chemistry)

-----  
**DEGREE**

Chemistry

Chemistry

-----  
**FIELD**

-----  
**DEPARTMENT**

**TITLE:** Computational and Theoretical Studies of Ionic Systems: From Gas Phase via  
Solutions to Heterogeneous Catalysis

**NAME:** Miss Natcha Injan

**THIS THESIS HAS BEEN ACCEPTED BY**

-----  
**THESIS ADVISOR**

( Professor Jumras Limtrakul, Ph.D. )

-----  
**THESIS CO-ADVISOR**

( Professor Michael Probst, Dr.rer.nat. )

-----  
**COMMITTEE MEMBER**

( Assistant Professor Piboon Pantu, Ph.D. )

-----  
**COMMITTEE MEMBER**

( Ms. Pensri Bunsawansong, Ph.D. )

-----  
**DEPARTMENT HEAD**

( Assistant Professor Noojaree Prasitpan, Ph.D. )

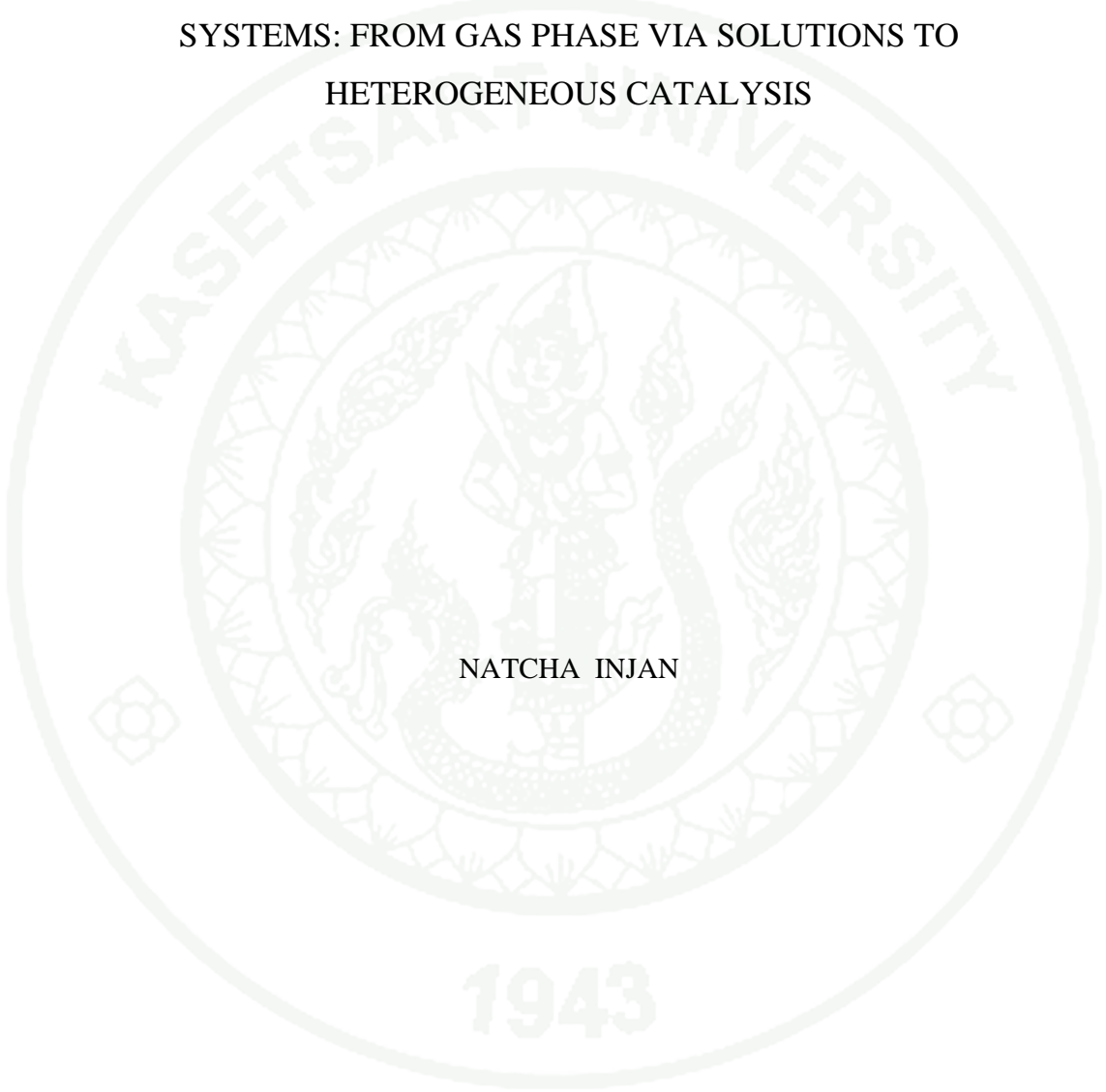
**APPROVED BY THE GRADUATE SCHOOL ON** \_\_\_\_\_

-----  
**DEAN**

( Associate Professor Gunjana Theeragool, D.Agr. )

THESIS

COMPUTATIONAL AND THEORETICAL STUDIES OF IONIC  
SYSTEMS: FROM GAS PHASE VIA SOLUTIONS TO  
HETEROGENEOUS CATALYSIS



NATCHA INJAN

A Thesis Submitted in Partial Fulfillment of  
the Requirements for the Degree of  
Doctor of Philosophy (Chemistry)  
Graduate School, Kasetsart University

2010

Natcha Injan 2010: Computational and Theoretical Studies of Ionic Systems: From Gas Phase via Solutions to Heterogeneous Catalysis. Doctor of Philosophy (Chemistry), Major Field: Chemistry, Department of Chemistry. Thesis Advisors: Professor Jumras Limtrakul, Ph.D. 143 pages.

Ionic systems covering from the gas phase via solutions to heterogeneous catalysis have been investigated using electronic structure theory and molecular dynamics studies.

Dissociative electron attachment (DEA) on the gas phase purine (Pu) and its derivatives (adenine (Ad) and 6-fluoropurine (6-fPu)) was studied by means of quantum chemical calculations. The resulting DEA products are dehydrogenated anions and hydrogen. The energies required for removing one hydrogen atom from the purine ring were calculated with the G2MP2 method. It was found that the hydrogen atom at the N9 site needs the least energy for dissociation (0.54 eV (6-fPu), 0.72 eV (Pu) and 0.94 eV (Ad)), which are in good agreement with experimental values. Adiabatic neutral and anionic potential energy surfaces were calculated at the UB3LYP/cc-pVTZ level of theory. From these the vibrational energy levels of the stretching vibrations were calculated in order to obtain the energy levels for the DEA reaction.

Potential energy functions for the interaction between  $\text{Au}^+$  cation and dicyanoaurate (I) anion ( $\text{Au}(\text{CN})_2^-$ ) and nitromethane (NM) were constructed and then used in molecular dynamics simulations of  $\text{Au}^+/\text{Au}(\text{CN})_2^-$  ion in liquid NM. It was found that the first solvation shell around the ion contains 9-10 and 15-16 NM molecules, respectively for the  $\text{Au}^+$  and  $\text{Au}(\text{CN})_2^-$  cases. An X-ray diffraction measurement on a diluted solution of  $\text{KAu}(\text{CN})_2$  in NM was in good agreement with the simulated one. Complementary, extensive quantum chemical calculations on  $\text{Au}^+-\text{NM}_n$  and  $\text{Au}(\text{CN})_2^--\text{NM}_n$  clusters were performed as well. They show the especially strong binding between Au and NM in  $\text{AuNM}_2^+$ . For higher values of n, the resulting geometries reflect the fact that the NM-NM interaction dominates over  $\text{Au}^+-\text{NM}$  and  $\text{Au}(\text{CN})_2^--\text{NM}$  interactions.

The direct benzene-to-phenol conversion on Fe-ZSM-5 was elucidated via density functional theory at M06/6-31G (d,p) level of theory. From the results, benzene is favorably activated by  $\alpha$ -oxygen of the active dioxo-Fe center via electrophilic substitution to form the  $\sigma$ -adduct. This adduct can further transform into the very stable hydroxo-phenoxo intermediate by either via the proton shuttle of the  $\sigma$ -adduct or via the 1,5-H shift of 2,4-cyclohexadienone which is produced from 1,2-H shift of the  $\sigma$ -adduct. Finally, the hydroxo hydrogen shifts to the phenoxo oxygen to form phenol which is proposed to be a rate-determining step with the activation energy of 45.7 kcal/mol.

---

Student's signature

---

Thesis Advisor's signature

## ACKNOWLEDGEMENTS

I would like to gratefully thank my advisors, Prof. Dr. Jumras Limtrakul and Prof. Dr. Michael Probst, for their advice, encouragement and valuable suggestions during my graduate study. Without their help and support, I would not be here today.

I would sincerely like to thank the members of my defensive examination committee, Assist. Prof. Dr. Piboon Pantu and Dr. Pensri Bunsawansong and the Graduate School Representative, Assoc. Prof. Saman Mongkolsakulvong, for their valuable comments and suggestions.

Of course, without various funding organizations, my graduation day would never have come. I want to state my acknowledgement to the Commission on Higher Education (the University Development Commission Scholarship) for giving me the opportunity to spend 5 years to study in the Ph.D. program, including doing research work at Innsbruck University, Austria, for 1 year. I also thank the National Science and Technology Development Agency (NSTDA Chair Professor and NANOTEC Center of Excellence), National Center of Excellence for Petroleum, Petrochemicals and Advanced Materials, the Thailand Research Fund, the Kasetsart University Research and Development Institute (Center of Nanotechnology) as well as the Graduate School of Kasetsart University because without their support my work at Kasetsart University would have been just a dream.

I cannot even begin to explain how thankful I am to all of these people who have always been there for me and supported me: Dr. Boonruen Sunphet, Dr. Pipat Khongpracha, Dr. Somkiat Nokbin, Dr. Jakkapan Sirijaraensre, Dr. Tanin Nanok, Dr. Supawadee Namuangruk, Dr. Chompunuch Warakulwit, Dr. Bundet Boekfa, Mr. Chadchalerm Raksakoon, Mr. Sombat Ketrat, and Ms. Panvika Pannopard.

Finally, I am especially indebted to my parents (Mr. Anun and Mrs. Nopparat), my elder sister (Ms. Annapa) and younger brother (Mr. Rattapon) for their continuing encouragements.

Natcha Injan

March 2010

**TABLE OF CONTENTS**

	<b>Page</b>
TABLE OF CONTENTS	i
LIST OF TABLES	ii
LIST OF FIGURES	iv
LIST OF ABBREVIATIONS	x
INTRODUCTION	1
LITERATURE REVIEW	10
METHODS OF CALCULATIONS	25
RESULTS AND DISCUSSION	43
CONCLUSIONS	114
LITERATURE CITED	116
APPENDIX	136
CURRICULUM VITAE	141

## LIST OF TABLES

<b>Table</b>		<b>Page</b>
1	Atomic partial charge (NPA) and electronic configurations (NEC) of the atoms in NM, AuNM <sup>+</sup> and AuNM <sub>2</sub> <sup>+</sup> . See text for details.	59
2	Atomic partial charges (NPA) and 6s and 5d populations (NEC) of Au in AuNM <sub>3</sub> <sup>+</sup> : geometry-optimized (left) and forced C <sub>3h</sub> -symmetric structure (right).	61
3	Atomic partial charge (NPA) and electronic configurations (NEC) of the atoms in Au(I), CN <sup>-</sup> , AuCN and Au(CN) <sub>2</sub> <sup>-</sup> . See text for details.	65
4	Charges and fitted parameters (kcal/mol and Å <sup>-1</sup> ) for the Au <sup>+</sup> -NM pair potential. See text for explanations.	71
5	Atomic partial charges in Au(CN) <sub>2</sub> <sup>-</sup> , K <sup>+</sup> and NM used in equations 15-17.	73
6	Values of the fitted parameters (kcal/mol) for the Au(CN) <sub>2</sub> <sup>-</sup> -NM pair potential.	74
7	Fitted parameters (kcal/mol) for the K <sup>+</sup> -NM pair potential.	76
8	Values of the parameters of the K <sup>+</sup> -Au(CN) <sub>2</sub> <sup>-</sup> pair potential. Energies are given in kcal/mol.	77
9	Values of the parameters of the NM-NM pair potential (equation 18). Energies are given in kcal/mol.	78
10	Characteristic values of the radial distribution functions for the Au <sup>+</sup> -nitromethane system with the new (a) and the generic (b) NM-NM potential energy function.	85
11	Characteristic values of the radial distribution functions for the (a) Au(CN) <sub>2</sub> <sup>-</sup> -NM, (b) KAu(CN) <sub>2</sub> -NM systems.	90

**LIST OF TABLES (Continued)**

<b>Table</b>		<b>Page</b>
12	Bond dissociation energies (BDEs) of hydrogen atoms in neutral molecules and the energies required for the dissociative electron attachment $MH + e^- \rightarrow M^- + H^+$ ( $E_{DEA}$ ) from G2(MP2) calculations. The values (in eV) include electronic energy and zero-point vibration energy.	94
13	Vibrational frequencies ( $\text{cm}^{-1}$ ) of neutral adenine (Ad), purine (Pu) and 6-fluoropurine (6-fPu).	96
14	Dipole moment of 6-dimethyladenine (6-dimAd), adenine (Ad), purine (Pu), 6-fluoropurine (6-fPu) and 8-fluoropurine (8-fPu) calculated with three methods and basis sets.	98

## LIST OF FIGURES

Figure		Page
1	Structure of 70T cluster model of Fe-ZSM-5 is taken from the straight channel (a) and the zigzag channel (b) views. Inner layer is presented as a stick style and a ball-and-stick style which is optimized. Outer layer is shown as a line style.	26
2	Electrostatic potential (right) and the surface of zero ESP (left) of a) NM and b) $\text{Au}(\text{CN})_2^-$ .	29
3	Positions of $\text{Au}^+/\text{K}^+$ around NM used for the construction of the $\text{Au}^+ \text{-NM}/\text{K}^+ \text{-NM}$ potential energy function. The solid lines refer to movement of $\text{Au}^+/\text{K}^+$ . The numbers of the lines refer to the energy curves in Figure 20 and 23.	30
4	Positions of $\text{K}^+$ around $\text{Au}(\text{CN})_2^-$ anion used for the construction of the $\text{K}^+ \text{-Au}(\text{CN})_2^-$ potential energy function. The numbers of the lines refer to the energy curves of Figure 24.	31
5	Directions of the atom of $\text{Au}(\text{CN})_2^-$ approaching to NM via a) the end-on by N atom of $\text{Au}(\text{CN})_2^-$ and via b) the side-on of $\text{Au}(\text{CN})_2^-$ where $\mathbf{X} = \text{Au}, \text{C}$ and $\text{N}$ .	32
6	Structure and standard numbering of all studied purines.	35
7	Charge-stabilization plot of electron affinity (eV) as functions of the added nuclear charge ( $\delta q$ ) for each N9-H bond length.	40
8	Dashed line: metastable part of anionic potential energy curve obtained by the extrapolation method, see text.	41
9	Relative energies and optimized structure together with some selected parameters of $\text{Z}^+[\text{FeO}_2]^+$ , $\text{Z}^+[\text{OFeO}]^+$ and transition state (TS_1) taken from zigzag channel of ZSM-5. Energies are given in kcal/mol and distances are given in angstroms.	45

## LIST OF FIGURES (Continued)

Figure		Page
10	Optimized structure of <b>1d1a</b> (left) and <b>2d1a</b> (right) adsorption complex together with the Fe...C distances. Distances are given in angstroms.	46
11	Energy profiles of the <b>1d1a</b> activation via H-abstraction (—••) and electrophilic substitution (- - -). Energies are obtained from the single point calculation at UM06//ONIOM2(UM06:UFF) level. Optimized structures are taken from the ONIOM2(UM06:UFF) level. Energies, distances and angles are given in kcal/mol, angstroms and degree.	49
12	Energy profiles: a) 1,2-H transfer (- - -), NIH shift (—) and proton-shuttle (••••) of the $\sigma$ -adduct (Int_2) and b) keto-enol tautomerization (—••) and proton shuttle (—) of 2,4-cyclohexadienone (Int_3). Energies are obtained from the single point calculation at UM06//ONIOM2(UM06:UFF) level and given in kcal/mol. Optimized structures with selected parameters are taken from the ONIOM2(UM06:UFF) level. Distances and angles are given in angstroms and degree.	52
13	Upper panel: Total ligand-cation binding energies of the most stable structure defined as $E = E(\text{Au}(\text{NM})_n^+) - E(\text{Au}^+) - n E(\text{NM})$ in the $\text{Au}(\text{NM})_n^+$ clusters with $n = 1$ to 10. Lower panel: Incremental energy for the same clusters, as defined as equation (11).	57
14	Geometries of $C_{3h}$ - symmetric (left) and fully geometry-optimized (right) $\text{AuNM}_3^+$ , together with Au-O distances (Å).	60
15	Optimized geometries together with the total ligand-cation binding energies ( $E$ ) of $\text{AuNM}_n$ with $1 \leq n \leq 10$ calculated at HF level. Energies are given in kcal/mol.	63

## LIST OF FIGURES (Continued)

Figure		Page
16	Electron density difference between $\text{Au}(\text{CN})_2^-$ complex and its constituents, Au(I) and the $\text{CN}^-$ . Isosurface plot (upper part) and integral of $\Delta\rho(x,y,z)$ over y and z (lower part). The excess density (purple color, at $\Delta\rho = 0.4 \times 10^{-3} \text{ e}/\text{\AA}^3$ ) is located around Au(I) while the $\text{CN}^-$ groups loose some electron density. (brown color, isosurface plotted at $\Delta\rho = -0.4 \times 10^{-3} \text{ e}/\text{\AA}^3$ ).	66
17	(Upper) Total ligand-cation binding energies of the most stable structure defined as $E = E(\text{Au}(\text{CN})_2^- \text{-NM}_n) - E(\text{Au}(\text{CN})_2^-) - n E(\text{NM})$ in the $\text{Au}(\text{CN})_2^- \text{-NM}_n$ clusters with $1 \leq n \leq 10$ . (Lower) Incremental energy defined as similar as equation (11).	68
18	Optimized geometries and binding energies of the stable conformations of $\text{Au}(\text{CN})_2^- \text{-NM}_n$ with $1 \leq n \leq 10$ calculated at the HF level. Energies are given in kcal/mol.	69
19	Potential energy surface of $\text{Au}^+ \text{-NM}$ along direction 1 as shown in Figure 3.	70
20	a) Au-NM interaction: Quantum chemical (x) and fitted (solid lines) energies. The numbers 1-8 refer to Figure 3. b) Fitting accuracy of the $\text{Au}^+ \text{-NM}$ potential energy function.	72
21	$\text{Au}^+ \text{-NM}$ Potential energy according to equation (14) in the $C_s$ plane of NM (right) and $2\text{\AA}$ above (left). Energies in kcal/mol and x/y coordinates in $\text{\AA}$ .	72
22	(Upper part) $\text{Au}(\text{CN})_2^- \text{-NM}$ interaction: Quantum chemical (x) and fitted (solid lines) energies. (Lower part) Fitting accuracy of the $\text{Au}(\text{CN})_2^- \text{-NM}$ potential energy function.	75
23	(Upper part) $\text{K}^+ \text{-NM}$ interaction: Quantum chemical (x) and fitted (solid lines) energies. The numbers 1-8 refer to Figure 3. (Lower part) Fitting accuracy of the $\text{K}^+ \text{-NM}$ potential energy function.	76

## LIST OF FIGURES (Continued)

Figure		Page
24	(Right) $K^+$ - $Au(CN)_2^-$ interaction: Quantum chemical (x) and fitted (solid lines) energies. (Left) Fitting accuracy of the $K^+$ - $Au(CN)_2^-$ potential energy function.	77
25	(Upper part) NM-NM interaction: Quantum chemical (x) and fitted (solid lines) energies. (Left) Fitting accuracy of the the NM-NM potential energy function.	79
26	Comparison of the various atom – atom terms of this work (solid lines) and the generic (dashed lines) NM-NM potential energy functions.	81
27	Au–NM radial distribution functions from the simulation utilizing the newly constructed NM-NM potential energy function.	83
28	Typical configuration of NM around $Au^+$ .	84
29	$Au(CN)_2^-$ -NM radial distribution functions from the simulation utilizing the newly constructed NM-NM potential energy function. a) free $Au(CN)_2^-$ ion and b) ion-pair $KAu(CN)_2$ complex.	87
30	Two dimensional projection of the distribution of nitromethane molecules around the central dicyanoaurate(I) ion, $Au(CN)_2^-$ .	87
31	Angular distribution function of $Au(CN)_2^-$ -NM system. $\Theta$ : angle between the dipole moment vector of the center of NM and Au(I) atom.	88
32	NM coordinated around $Au(CN)_2^-$ anion.	88
33	(Left) $K^+$ -NM and (right) NM-NM radial distribution functions of $KAu(CN)_2$ -NM.	89
34	Comparison of the radial distribution function obtained from the X-ray diffraction experiment and MD simulation of $KAu(CN)_2$ -NM.	91

## LIST OF FIGURES (Continued)

<b>Figure</b>		<b>Page</b>
35	(Left) LUMO of adenine neutral and (right) HOMO of dipole-bound state adenine anion, see text.	97
36	Molecular dipole moment (results from UB3LYP/cc-pVTZ calculations) of 6-dimethyladenine (6-dimAd), adenine (Ad), purine (Pu), 6-fluoropurine (6-fPu) and 8-fluoropurine (8-fPu). Arrows point to the positive end of dipole moment.	99
37	Electrostatic potential maps of the neutral 6-dimethyladenine (6-dimAd), adenine (Ad), purine (Pu), 6-fluoropurine (6-fPu) and 8-fluoropurine (8-fPu) molecules obtained from UB3LYP/cc-pVTZ calculations.	100
38	Isodensity maps (isovalue = 0.02) of the first four virtual $\sigma^*$ molecular orbitals at equilibrium geometry of the neutral 6-dimethyladenine (6dimAd), adenine (Ad), purine (Pu), 6-fluoropurine (6-fPu) and 8-fluoropurine (8-fPu) molecules obtained from UB3LYP/cc-pVTZ calculations. LUMO+7 of 6-dimAd is shown instead of its LUMO+6.	102
39	Isodensity maps (isovalue = 0.08) of the first four virtual $\sigma^*$ molecular orbitals at equilibrium geometry of the neutral 6-dimethyladenine (6-dimAd), adenine (Ad), purine (Pu), 6-fluoropurine (6-fPu) and 8-fluoropurine (8-fPu) molecules obtained from UB3LYP/cc-pVTZ calculations. LUMO+7 of 6-dimAd is shown instead of its LUMO+6.	103
40	Electron affinity curves of adenine as a function of N9-H bond length.	106

**LIST OF FIGURES (Continued)**

<b>Figure</b>		<b>Page</b>
41	a) Electron affinity curve of Ad obtained by using; 1) charge-stabilization and 2) extrapolation method, together with LUMOs of $\text{AdH} \rightarrow \text{Ad}^- + \text{H}^+$ reaction. Isovalue of orbital plot = $0.004 e/\text{\AA}$ . b) Neutral potential energy curve for $\text{AdH} \rightarrow \text{Ad}^- + \text{H}^+$ . c) A resulted anionic potential energy curve of Ad. d) Neutral curve for $\text{AdH} \rightarrow \text{Ad}^- + \text{H}^+$ together with anionic curve.	107
42	Upper panel: Adiabatic potential energy curves with zero-point energy (ZPE) correction of ground state of neutral adenine (Ad), purine (Pu) and 6-fluoropurine (6-fPu) molecules (blue line) and their corresponding anions (excess electron in the $\sigma^*$ MO, red line) obtained from UB3LYP/cc-pVTZ calculations. Lower panel: Spin density of anions.	110
43	Spin density surface (isovalue = $0.004 e/\text{\AA}$ ) of adenine anion obtained from UB3LYP/cc-pVT calculations.	111

## LIST OF ABBREVIATIONS

6-dimAd	=	6-dimethyladenine
6-fPu	=	6-fluoropurine
8-fPu	=	8-fluoropurine
Å	=	Angstrom
Ad	=	Adenine
Ads	=	Adsorption
AEA	=	Adiabatic electron affinity
B3LYP	=	Becke's three-parameters hybrid functional using the Lee-Yang-Parr correlation functional
BDE	=	Bond dissociation energies
BSSE	=	Basis set superposition error
CAS-SCF	=	Complete active space self-consistent field
CP-MD	=	Car-Parrinello Molecular dynamics
D	=	Debye
DBEA	=	Dipole-bound electron affinities
DBS	=	Dipole-bound state
DEA	=	Dissociative electron attachment
DFT	=	Density functional theory
DSB	=	Double-strand break
$e^-$	=	Electron
EA	=	Electron affinity
ECP	=	Effective-core pseudopotential
$E_{DEA}$	=	Energy required for the dissociative electron attachment
ESP	=	Electrostatic potential
ESR	=	Electron spin resonance
eV	=	Electron Volt
EXAFS	=	Extended X-rays absorption fine structure
fs	=	Femtosecond

**LIST OF ABBREVIATIONS (Continued)**

HF	=	Hartree-Fock
HOMO	=	Highest occupied molecular orbital
Int	=	Intermediate
IP	=	Ionization potential
K	=	kelvin
kcal/mol	=	kilocalories per mole
KIE	=	Kinetic isotope effects
kJ/mol	=	kiloJoules per mole
LEE	=	Low-energy electron
LUMO	=	Lowest unoccupied molecular orbital
MC	=	Monte Carlo
MC-SCF	=	Multi-configurational self-consistent field
MD	=	Molecular dynamics
MH	=	Molecule
MM	=	Molecular mechanics
MP2	=	The second-order Møller-Plesset perturbation theory
M <sup>•</sup>	=	Dehydrogenated molecule
NEC	=	Natural electronic configurations
NM	=	Nitromethane
NMR	=	Nuclear magnetic resonance
NPA	=	Natural population analysis
O <sub>α</sub>	=	α-oxygen
ONIOM	=	Our own N-layered integrated molecular orbital and molecular mechanics
OVGF	=	Outer Valence Green's Function
PEC	=	Potential energy curve
PES	=	Potential energy surface
Pro	=	Product
ps	=	Picosecond

**LIST OF ABBREVIATIONS (Continued)**

Pu	=	Purine
QM	=	Quantum mechanics
r[N9-H]	=	Distance between N9 atom and its own H
RDF	=	Radial distribution functions
SCF	=	Self-consistent field
SOMO	=	Singly occupied molecular orbital
SSBs	=	Single-stand breaks
T	=	Tetrahedral
TMA	=	Transient molecular anion
TS	=	Transition state
UFF	=	Universal force field
XD	=	X-ray diffraction
Z	=	Zeolite
ZPE	=	Zero-point energy

# COMPUTATIONAL AND THEORETICAL STUDIES OF IONIC SYSTEMS: FROM GAS PHASE VIA SOLUTIONS TO HETEROGENEOUS CATALYSIS

## INTRODUCTION

Nowadays, theoretical and computational chemistry has become a powerful tool for studying various systems and reactions. It can elucidate them over a wide range of system sizes -- macroscale, microscale and even molecular/atomic scale. Specially, it can perform in certain conditions that present experimental technologies cannot yet operate such as in very low pressure, extreme low temperature near a zero kelvin, and in studying an individual molecule. Many theories have been developed for giving accurate and reliable results on each scale. Theoretical studies can reliably provide information for all states -- gas, liquid and solid phases. Moreover, the synergy of experimental and theoretical studies indeed gives a deeply fundamental knowledge. This thesis investigates theoretically the following reactions and systems:

The first topic is ‘mechanisms and energetic of the direct benzene-to-phenol conversion on Fe-ZSM-5 zeolite: M06 density functional calculation’. This computational study investigates in the heterogeneous catalysis. It concerns to the partial oxidation of benzene to produce phenol as a product by using Fe-ZSM-5 as a solid catalyst. The reaction mechanisms and energetic have been elucidated via quantum chemistry at M06 level of theory which is one of Minnesota density functionals. These functionals have been developed to include the dispersion term which cannot be explained by the generic functionals including the popular B3LYP one.

‘Au(I) cation and Au(CN)<sub>2</sub><sup>-</sup> anion in liquid nitromethane: quantum chemical calculations and molecular dynamics simulations’ is the second one. It deals with the study of the behavior of gold ion and gold cyanide complex in liquid nitromethane.

Quantum chemical calculations reveal the energetic and the buildup of gold-nitromethane clusters while molecular dynamics (MD) simulations give the information about the dynamics of gold ion/complex in the solution. The resulting radial distribution function (RDF) of  $\text{Au}(\text{CN})_2^-$  in liquid nitromethane obtained from the MD simulation will compare with the one obtained from an X-ray diffraction experiment.

The last topic is ‘effect of substituent group on dissociative electron attachment of purines: quantum chemical study’. The motivation of this work came from the experimental study of Denifl *et al.* (2007) on low-energy electrons attacking to purine derivatives (purine, adenine, etc.). They found an interesting spectrum of the dehydrogenated anion amount as a function of the electron energy. Importantly, the results showed the butterfly effect of the different substituents at the C6 site of purine strongly affects the spectra of the dehydrogenated anion, although the dissociated hydrogen comes from the distant N9 position. This thesis work has studied on the effect of electron-donating (adenine) and electron-withdrawing (6-fluoropurine) groups at C6 position of gas phase purine on the dissociative electron attachment (DEA) process by means of quantum chemical calculations.

Theoretical studies have been investigated on three above topics in order to get deeply insight of them. The details are shown in the followings.

### **Mechanisms and energetic of the direct benzene-to-phenol conversion on Fe-ZSM-5 zeolite: M06 density functional calculation**

Environmental issues have high priority with every activity in the chemical industry. Some multi-step reactions cause huge problems because they leave undesirable and unusable by-products like greenhouse gases behind. Even reactions at high temperature are not environmentally-friendly due to their energy requirements. Therefore, new ‘green’ reactions with fewer processing steps and giving higher productivity (in terms of high quantity of both reactant conversion and of product selectivity) and reactions that work at lower temperatures are required. Ideally, in

terms of effective resource utilization by-products coming from the other (or even the same) reactions are used as a reactant or reagent. Of course, in such cases also the operating cost is lowered.

One possible solution is to find new catalyst which works like enzymes in biology. An interesting enzymatic reaction is the methane-to-methanol conversion by methanomonooxygenase (sMMO) enzyme, one of the monooxygenases (MOs), using  $O_2$  as an oxidant. Another MO enzyme is cytochrome P450 which can oxidize a variety of aromatic and aliphatic compounds. These partial oxidation reactions run at room temperature. Therefore, many researchers have investigated possibilities to design and to develop non-enzymatic catalysts that can mimic the ability of enzyme for catalyzing various reactions.

The selective oxidation of hydrocarbon is one of the most interesting reactions, especially the hydroxylation of benzene to phenol. Phenol is one of the most important chemicals in the fields of resin, fiber and medicine. Nowadays, phenol is industrially produced by the three-step oxidation of cumene which is formed in the Friedel-Crafts alkylation of benzene by propene. Although the cumene process illustrates the benefit of chemical engineering in merely converting two relatively cheap starting materials, benzene and propene into a more valuable one, phenol, it also creates acetone as a by-product of this process. As a consequence, the cost of phenol is strongly dependent on the market demand for the unavoidable by-product acetone, which is much smaller than that of phenol. Additionally, the reaction produces an explosive intermediate, cumene hydroperoxide. In the quest to produce phenol with high selectivity and without any by-products, the direct oxidation of benzene to phenol is one potential candidate for the chemical industry.

Zeolite is a porous aluminosilicate crystal that comes in many different diameters of pore size and also in different dimensionalities of its channel system. For instance, chabazite and SAPO-34 have a small pore of  $3.8 \times 3.8 \text{ \AA}$  and three-dimensional (3-D) channel. The medium pore zeolite are, for example, ZSM-5 ( $5.3 \times 5.6 \text{ \AA}$  pore size and 3-D channel), ferrierite ( $4.2 \times 5.4 \text{ \AA}$  pore size and 2-D

channel),  $\text{AlPO}_4\text{-11}$  ( $3.9 \times 6.3$  Å pore size and 1-D channel). The 3-D channel faujasite and the 2-D channel mordenite consist of a large pore size ( $7.4$  Å for faujasite and  $6.5 \times 7.0$  Å for mordenite). Zeolites are used as shape-selective molecular sieves.

Their unique property is that their own active sites can be modified by adding various cations into the framework or on extra-framework. This modification leads to zeolite that can catalyze a wide range of reactions. Particularly, transition-metal cation addition lets zeolite act as catalyst in several oxidation-reduction reactions. For example, iron ion added onto the extra-framework site of zeolite or so-called Fe-exchanged zeolite can react with an oxidant forming an unique iron-oxide active site, called  $\alpha$ -site. This active site which looks like the effective active site of sMMO enzyme can catalyze the partial oxidation reaction of methane and other hydrocarbons such as benzene (Panov *et al.*, 1990; Panov *et al.*, 1992; Panov *et al.*, 1993; Sobolev *et al.*, 1993; Sobolev *et al.*, 1995; Dubkov *et al.*, 1997; Kharitonov *et al.*, 1993) at low temperature.

In the last decade, experimental studies showed that 100% selectivity to phenol can be obtained by oxidizing benzene with  $\text{N}_2\text{O}$  over Fe-ZSM-5 catalyst at about 20-25% conversion rate (Panov *et al.*, 1993). This reaction can be called a green process because it uses  $\text{N}_2\text{O}$ , a greenhouse gas and a by-product in the production of adipic acid which is an intermediate for Nylon-6,6 synthesis. These findings have motivated an interest in identifying the structure of the active site for the hydroxylation of benzene and the reaction mechanism.

This work theoretically investigates on the hydroxylation of benzene over the dioxo-mononuclear iron species on ZSM-5 zeolite,  $\text{Z}[\text{OFeO}]^+$  in order to find the structure of active site of Fe-ZSM-5 zeolite, to determine the most possible mechanism of this partial oxidation of benzene, and to explore the energetic profiles of this reaction.

### **Au(I) cation and Au(CN)<sub>2</sub><sup>-</sup> anion in liquid nitromethane: quantum chemical calculations and molecular dynamics simulations**

A renewed interest in the properties of gold ions (Pyykko, 2004a) in non-aqueous solution can be noticed and stems from various new applications and problems. New applications of gold solutions in nanotechnology and cluster science deal, for example, with gold nanowires and with the catalytic properties of gold nanoclusters. Many applications utilize the ability of gold to change easily between the oxidation states 0, 1 and 3. Potentially useful nanostructures can also be formed by self-assembly of ligands around gold ions. Some building blocks can be constructed by a solution of gold or the mixture of various metals (Au, Pt or Pd etc.) and then make triangle, squares, etc. For example, dicyanoaurate(I) anion (Au(CN)<sub>2</sub><sup>-</sup>) can act as a building block and is used to construct the new cyanide-bridged heterobimetallic coordination polymers. These polymers feature various networks such as 3-D network, 1-D zigzag chain structure and an extended supramolecular 2-D array. Some of them exhibit a strong green emission band ( $\lambda_{\text{max}} = 524 \text{ nm}$ ) at room temperature (Guo *et al.*, 2009). Gold surfaces are often needed in industry, for instance, as catalyst and also the gold comes from non-aqueous solution. Gold surfaces in contact with various solvents play an important role in electrochemistry and in technology and gold is a biocompatible metal. Moreover, gold derivatives can be applied in drug transportation. On the other side, gold – like it is the case for other heavy metals - is an environmental liability. Since it is omnipresent in electronics devices it has to be separated and recovered before dumping or burning outdated boards and other scrap. Gold withdrawal from old electric circuits is a very important economic due to it is one of the precious metals and environmental topic.

For almost applications as mentioned above gold must be oxidized into Au(I) or Au(III) and form complexes in solution then extract it from the solution into Au(0) or any oxidation state or complex in solid state. Normally all of these gold ions, Au(I) and Au(III), mostly exists in non-aqueous solution due to the high tendency for complexation of gold ions. Specially, aurous ion (Au(I)) is rare to exist. Normally it

forms complex with any ligand such as dicyanoaurate(I) anion ( $\text{Au}(\text{CN})_2^-$ ).  $\text{Au}(\text{CN})_2^-$  is an especially stable and well-known gold complex. It can, for example, be prepared as an alkaline salt,  $\text{NaAu}(\text{CN})_2$  or  $\text{KAu}(\text{CN})_2$ , by cyanidation of gold cluster (Cui and Zhang, 2008). Gold itself is non-toxic and it is even used as food decoration and ingredient in the form of gold leaf. However, gold in solution or gold salts such as potassium gold cyanide,  $\text{KAu}(\text{CN})_2$ , which is used in gold electroplating are toxic to the liver and kidneys. Therefore, to bring gold into solution, optimal processes for retrieving gold under such circumstances are still under investigation (Cui and Zhang, 2008; Pyykko, 2005).

These applications and facts make it desirable to know how the gold ions “live” in the solvent and nitromethane (NM) is one of the premier solvents for gold complexes. The solvation of metal ions is important in understanding, for example, the role of metals in the catalytic activity, the dynamics of host-guest chemistry, the selective ion transport through membranes, and so forth. On the theoretical side, molecular dynamics (MD) and Monte Carlo (MC) simulations and *ab initio* calculations have been performed in order to elucidate the structures, energetic and dynamics of solvated ions at the molecular level. Most of these theoretical studies have attempted to answer the question how the solvent molecules build up about the central ion in distinct shells.

In general, little is known about the microscopic details of solutions of gold complexes. Therefore this work is investigated to the specific properties of  $\text{Au}(\text{I})\text{-NM}_n$  clusters via quantum chemical calculations and the behaviors of  $\text{Au}(\text{I})$  as a free ion and in a gold-ligand  $\text{Au}(\text{CN})_2^-$  complex in liquid nitromethane by means of molecular dynamics simulations.

### **Effect of substituent group on dissociative electron attachment of purines: quantum chemical study**

It is well-known that an ionizing radiation (UV, X-rays, etc.) can damage DNA. The damage can be found as, for example, a mismatch, a stacking formation

and a wrong sequence of nucleic acid bases in DNA helix including single-stand breaks (SSBs) and double-stand breaks (DSBs) of the DNA helix. Such damages can be found for both reversible alteration and complete alteration. If irreversible changes have been reached, these events then lead to genetic mutation, tumor or even cancer, since DNA contains the genetic information. Not only the first impact of high-energy radiation can cause the injury of DNA but especially the secondary particles (i.e. ions, radicals, and secondary electrons) created by photoionization of living cells,  $h\nu + M \rightarrow M^+ + e^-$ , are harmful. This is the case because these particles with energies below 30 eV are produced in large extent ( $\sim 10^5$ /MeV of incident electron energy). Among them, secondary electrons, called low-energy electrons (LEEs), are the most abundant. In the last decade, experimental (Boudaiffa *et al.*, 2000a; Boudaiffa *et al.*, 2000b; Martin *et al.*, 2004) and theoretical (Li *et al.*, 2003) investigations have found that LEEs with energies of  $\sim 3$ -20 eV can induce DNA damage. An understanding of the mechanism of DNA damage by LEEs is of importance in many fields and, especially, in radiotherapy. This may help researchers to develop and improve the method and the instrument that increase the damage to cancer issues and decrease the damage to normal cells. Therefore, one line of the current research on radiation damage focuses on the interaction of LEEs having a kinetic energy below 30 eV with DNA complex and its building blocks --the nucleic acid bases, the sugar, and the phosphate units.

Focus on the field of low-energy electrons (LEEs) attacking on DNA, the group of Sanche (Boudaiffa *et al.*, 2000b) was the first one who discovered, by using electrophoresis technique, that single-strand breaks (SSBs) and double-strand breaks (DSBs) of the plasmid DNA strands can take place by LEEs (3-20 eV). Their findings revealed that this even occurs at subionization energies (ionization limit of DNA  $\sim 7.5$ -10 eV). The damage of DNA is indeed a function of the initial kinetic energy ( $E_0$ ) of the incident electron. The mechanism of DNA damage was thought to occur via the formation of a temporary bound anion or a transient molecular anion (TMA) of the normal DNA after exposing it to LEEs. The TMA then can lose its extra energy by either releasing the electron (autodetachment -- elastic or inelastic scattering) or by dissociating certain bonds to form stable fragments. The dissociation pathway

corresponds to DNA-stand breaks because the TMA has a repulsive potential along the coordinate of the breaking bond. This reaction is therefore a typical dissociative electron attachment (DEA).

Dissociative electron attachment (DEA) is one type of electron-molecule reactions. A brief overview of the various kinds of such reactions together with the basic concept of the quantum chemical techniques required for these systems is given in Appendix.

The fundamentals of DEA on DNA can also be obtained by studying LEEs attacking the isolated nucleic acid bases (also called nucleobases), the sugar and the phosphate units. This basic knowledge can help researchers to understand the DEA mechanism of larger or more complicated units. Nucleobases act as antennas to induce LEE because of their large dipole moments ( $>2$  Debye) which can capture an excess electron in a dipole-bound state and that can then tunnel into other valence molecular orbitals (Sommerfeld, 2004). Therefore, many studies have investigated in detail the interaction of LEEs and nucleobases -- adenine, guanine, cytosine, thymine and uracil.

In order to get basic experimental information about electron-molecule reactions a “clean” and well-prepared experimental situation is needed. Recently this has become possible by performing low-energy electron-molecule reaction crossed-beam gas-phase experiments with high resolution of the electronic energy and an accurate determination of the kind and the energy of the resulting species, normally in specialized mass spectrometers, for example, (Abdoul-Carime *et al.*, 2004; Abdoul-Carime and Sanche, 2002; Burrow *et al.*, 2006; Denifl *et al.*, 2004b; Denifl *et al.*, 2004c; Fiegele *et al.*, 2001; Flosadottir *et al.*, 2007; Gluch *et al.*, 2004; Panajotovic *et al.*, 2007; Park *et al.*, 2006; Shafranyosh *et al.*, 2006). Therefore, gas-phase experiments are the natural choice to investigate the isolated DNA bases. Still, experimentally the ultimate goal of identifying all species with arbitrary energy resolution is not achieved, and custom-made experimental setups are handled worldwide by a few groups only.

On the side of theoretical calculations the situation is rather difficult: there is no unified treatment of electron-molecule reactions for all systems and energies. The problem lies in the complications that arise when going from static to time-dependent descriptions and in treating bound states and continuum states together. Depending on the energy of the incoming electron various approximate treatments can be applied. One extreme is the high-energy situation: in plasma physics one is often interested in the rate with which electrons react with a molecular gas for a wide range of electron energies, typically 0 to 104 eV. The reaction rate as a function of the energy can be displayed in a cross section curve. Accurate calculations would require integrating over states and orientations for each energy state. Often a calculation of the reaction of a molecule with an electron for a single molecular state and orientation is difficult. Fortunately, at least for higher energies, semi-empirical expressions have been derived from which cross sections can be calculated. Their accuracy is often sufficient for technological applications (Deutsch *et al.*, 2003a; Deutsch *et al.*, 2003b; Deutsch *et al.*, 2003c; Scheier *et al.*, 2004).

This work is motivated by the experiments of Denifl and co-workers that the substituent groups at the C6 site of the purine ring affect the DEA process and lead to quite different mass spectra (Denifl *et al.*, 2007). The ion yield shows narrow peaks at 0.72, 0.84, and 1.07 eV (all values  $\pm 0.07$  eV) for purine, adenine and 6-dimethyladenine, respectively. They discussed this phenomenon on the basis of the different electrostatic potential (ESP) of each molecule. Therefore, this study investigates in detail of the effect of substituent groups on DEA of purine (Pu), adenine (Ad) and 6-fluoropurine (6-fPu) by means of quantum chemical calculations.

## LITERATURE REVIEW

### **Mechanisms and energetic of the direct benzene-to-phenol conversion on Fe-ZSM-5 zeolite: M06 density functional calculation**

Several theoretical and experimental studies have tried to elucidate the structure of the active site in Fe-ZSM-5. Chen and co-workers proposed four possible positions of iron active species in Fe-ZSM-5 zeolite: (i) a mononuclear at the extra-framework of zeolite, (ii) a mononuclear in the tetrahedral positions (substituting silicon in zeolite framework), (iii) nanoclusters of iron-oxide, (iv) oxygen-bridged binuclear iron ions (Chen *et al.*, 2000). Panov and co-workers originally proposed that the catalytic site of Fe-ZSM-5, exhibiting high reactivity towards hydroxylation reaction, is in the extra-framework position which is called  $\alpha$ -sites (Kharitonov *et al.*, 1993). Experimental study by Kubanek and co-workers uphold the results of Panov and co-workers that the extra-framework of iron-oxo species is essential for the hydroxylation of benzene (Kubanek *et al.*, 1993). The presence of Fe-O-Al entity is necessary for N<sub>2</sub>O decomposition leading formation of surface oxygen which is named  $\alpha$ -oxygen (Hensen *et al.*, 2003, Hensen *et al.*, 2004). The work of Starokon and co-workers revealed that the  $\alpha$ -oxygen is an anion-radical (O <sub>$\alpha$</sub> <sup>-</sup>) which has a remarkably different oxidation property from the generic O<sup>-</sup> species in which the former can cause selective oxidation of hydrocarbon while the latter complete oxidation to CO<sub>2</sub> and H<sub>2</sub>O occurs (Starokon *et al.*, 2003). Additionally, they also proposed that the structure of the  $\alpha$ -sites is oxygen-bridged binuclear iron ions located in the extra-framework position of zeolite in which each Fe ion acts as the  $\alpha$ -site (Starokon *et al.*, 2003). However, Choi and co-workers reported EXAFS studies of Fe-ZSM-5 samples with the Fe:Al ratio < 1, which were prepared in the solid-state in a form of mononuclear ion complexes as either [FeO<sub>2</sub>]<sup>+</sup> or [Fe(OH)<sub>2</sub>]<sup>+</sup> (Choi *et al.*, 2003; Choi *et al.*, 2004). EXAFS measurements for the dioxide forms of mononuclear iron species, Z[FeO<sub>2</sub>]<sup>+</sup>, or the dihydroxide, Z[Fe(OH)<sub>2</sub>]<sup>+</sup> showed that the distance between Fe and Al is about 2.9 Å. Sun and co-workers suggested that oligonuclear, perhaps binuclear, iron sites are most favorable for nitrous oxide decomposition, whereas the mononuclear iron sites are active for benzene hydroxylation to phenol

(Sun *et al.*, 2008). Theoretically, the extra-framework oxo-Fe intermediates, such as peroxy-iron  $[\text{Fe}^{\text{III}}\text{O}_2]^+$  (Ryder *et al.*, 2002; Ryder *et al.*, 2003), high-valency dioxo-iron  $[\text{OFe}^{\text{III}}\text{O}]^+$  (Pantu *et al.*, 2004), high-valency monooxo-iron  $([\text{Fe}^{\text{III}}=\text{O}]^+)$  (Shiota *et al.*, 2005; Shiota *et al.*, 2006; Yoshizawa *et al.*, 2003; Yoshizawa *et al.*, 2000a; Yoshizawa *et al.*, 2000b; Yoshizawa *et al.*, 1999) and  $[\text{Fe}^{\text{IV}}=\text{O}]^+$  (Kachurovskaya, 2004; Kachurovskaya *et al.*, 2003), had been proposed to be the  $\alpha$ -site of zeolite for hydrocarbon hydroxylation. Ryder and co-worker suggested that the hydroxylation of benzene preferably occurs at the peroxy-iron species,  $[\text{FeO}_2]^+\text{Z}^-$  rather than monooxo-iron species,  $[\text{FeO}]^+\text{Z}^-$  in which  $\text{N}_2\text{O}$  decomposition mostly takes place (Ryder *et al.*, 2003).

Many experimental and theoretical studies on the benzene to phenol conversion had been published. One important information on the mechanism was obtained from the study of kinetic isotope effects (KIE) by Dubkov and co-workers (Dubkov *et al.*, 1997). The authors studied KIE of the conversion of methane to methanol and benzene to phenol on Fe-ZSM-5. Symmetrically deuterium-labeled methane ( $\text{CH}_2\text{D}_2$ ) and benzene (1,3,5- $\text{d}_3$  benzene) were used in this study. KIE ( $K_{\text{H}}/K_{\text{D}}$ ) values were calculated from the intensity of  $^1\text{H}$  NMR signal. The results showed that the intramolecular KIE values of methane to methanol are in the range 1.9-5.5 depending on the temperature (100 to  $-50^\circ\text{C}$ ) while those of benzene to phenol is unity. Consequently, they concluded that the C-H bond breaking is the rate-determining step for methane conversion while it is not for benzene hydroxylation. According to KIE experiments, the benzene to phenol conversion should proceed via the formation of arene oxide, which is an unstable compound, and then the C-H bond breaks rapidly to form the phenol product. They suggested the rate-determining step of benzene conversion may be the epoxidation of the aromatic ring or unstable arene oxides. According to experiment of the cytochrome P450 enzyme, the aromatic hydroxylation occurs via an electrophilic aromatic substitution (de Visser *et al.*, 2007).

An apparent activation energy of 126 kJ/mol for the benzene to phenol conversion over Fe-ZSM-5 using N<sub>2</sub>O as an oxidant was reported by Ivanov *et al.* (2003). The rate-determining step deals with the  $\alpha$ -oxygen generation by N<sub>2</sub>O decomposition which takes place simultaneously with the phenol desorption at the same  $\alpha$ -site.

Quantum chemistry is a tool for understanding the structure of active site in Fe-ZSM-5 zeolite and its activity in several selective oxidation reactions. Kachurovskaya and co-workers (Kachurovskaya *et al.*, 2003) performed calculations of intermediates of benzene to phenol oxidation by N<sub>2</sub>O on Fe-ZSM-5 at the B3LYP/6-31G\* level of theory. The  $\alpha$ -position of ZSM-5 consisting of two intersecting five-membered rings in which forms six-membered ring was chosen in a 10T cluster model. Two Al atoms replaced two distant Si atoms and therefore the iron species of this work is formally Fe(II) ion with a total spin of 2. In this work, no transition states participating in the reaction but they proposed a mechanism by estimating the stability of possible intermediates. The  $\alpha$ -oxygen was generated by the deposition of the N<sub>2</sub>O oxygen on Fe(II) ion. The dissociation energy of Fe=O was calculated to be 232.0 kJ/mol which is in good agreement with the experimental data of  $250.8 \pm 41.8$  kJ/mol (Panov *et al.*, 1998). They found only the adsorbed benzene oxide but the adsorbed benzene complex was not found. This would indicate a very low activation energy of the reaction towards benzene oxide. Therefore, they believed that step (1) of Dubkov (1997) concerning the formation of arene oxide should not be the rate-determining step. The transfer of arene oxide to its zwitterions, which oxygen of FeO<sup>+</sup> is bonded to one carbon atom of benzene or so-called the  $\sigma$ -complex in the work of Yoshizawa (2000), had been proposed as a rate-determining step in zeolitic system. Kachurovskaya (2004) investigated the benzene to phenol conversion over Fe-Ferrierite performed by periodic ab initio calculations, using VASP program. Taking into account the framework effect, the sorbed benzene was found while the cluster calculation of previous work (Kachurovskaya *et al.*, 2003) had not been observed. In this work they confirmed their previous work (Kachurovskaya *et al.*,

2003) that the transformation from benzene oxide to the zwitterion is the rate-limiting step.

Ryder and co-workers (Ryder *et al.*, 2003) performed density functional theory (DFT) calculations of the mechanism of benzene to phenol conversion. The reaction rates of N<sub>2</sub>O decomposition and of the partial oxidation of benzene were also calculated. A 5T cluster model in which Al was placed at T12 position represented the active site. The peroxy-iron [FeO<sub>2</sub>]<sup>+</sup> and the monooxy-iron [Fe=O]<sup>+</sup> represented the α-site. According to their previous study (Ryder *et al.*, 2002) the peroxy-iron species [FeO<sub>2</sub>]<sup>+</sup> was the most abundant one among all possible oxo-iron species. They proposed that an oxygen atom of the oxo-iron center can directly insert into the C-H bond of benzene. This mechanism is a one-step process. For both oxo-iron species, the potential energy surface of sextet state lies below those of doublet and quartet states. The activation energy concerning the α-oxygen inserts into C-H bond was 45.7 and 60.1 kcal/mol for [FeO<sub>2</sub>]<sup>+</sup> and [FeO]<sup>+</sup>, respectively. The authors calculated the rate of benzene oxidation and of N<sub>2</sub>O decomposition on [FeO<sub>2</sub>]<sup>+</sup> and [FeO]<sup>+</sup> sites. These findings indicated that the hydroxylation of benzene preferably occurs at the peroxy-iron species, [FeO<sub>2</sub>]<sup>+</sup>Z<sup>-</sup> rather than monooxy-iron species, [FeO]<sup>+</sup>Z<sup>-</sup>. On the other hand, N<sub>2</sub>O decomposition mostly takes place at [FeO]<sup>+</sup> site. Due to the absence of KIE of benzene to phenol conversion the C-H cleavage should not be the rate-limiting step (Dubkov *et al.*, 1997). Therefore, they also performed KIE calculations resulting in a KIE value corresponding the active oxygen inserts into the C-H bond of ≈1 which is in good agreement with the experiment. As a result, the proposed mechanism of oxygen insertion is a plausible rate-determining step in the oxidation of benzene.

Yoshizawa and co-workers did a series of theoretical studies of benzene-to-phenol conversion (Yoshizawa *et al.*, 1999; Yoshizawa *et al.*, 2000a; Yoshizawa *et al.*, 2000b; Yoshizawa *et al.*, 2003; Shiota *et al.*, 2005; Shiota *et al.*, 2006). They proposed three possible pathways for the benzene-to-phenol conversion by using the FeO<sup>+</sup> species in the gas phase and the zeolitic system. Three proposed reaction pathways were: i) a radical mechanism that creates a phenyl radical and a FeOH

fragment as an intermediate, ii) an oxygen-insertion of adsorbed benzene  $\sigma$ -complex that occurs via an arenium intermediate, and iii) non-radical mechanism to form a hydroxo intermediate,  $\text{HO-Fe}^+-\text{C}_6\text{H}_5$ . They found that the quartet state played a vital role in benzene oxidation than the sextet state.

The radical mechanism is well-known as a radical rebound mechanism for the catalytic mechanism of alkane hydroxylation by cytochrome P450 (Groves *et al.*, 1981). It was proposed for the 3T cluster of ZSM-5 (Yoshizawa *et al.*, 2000b). The oxygen of  $[\text{FeO}]^+$  moiety was weakly bonded to the hydrogen of benzene. As a result, an adsorbed benzene  $\sigma$ -complex was found for this mechanism. The transition state's structure of H-abstraction is a linear  $\text{C}\cdots\text{H}\cdots\text{O}$  angle structure. The phenyl radical bound to hydrogen atom of the FeOH fragment is obtained as an intermediate. The energy barrier for this step was calculated to be 10.4 and 8.1 kcal/mol for the sextet and quartet states, respectively. Then the bound phenyl radical shifted in order to form phenol and energies of 12.4 and 3.3 kcal/mol was necessary for the sextet and quartet states, respectively.

The second mechanism proposed by Yoshizawa and co-workers is the oxygen-insertion (Yoshizawa *et al.*, 2000b). The adsorbed benzene was found in the nonplanar geometry which H atom of carbon attached by O of  $[\text{FeO}]^+$  is out-of-plane. At this stage the O-C bond did not form yet. Next the C-O bond was formed to obtain the benzene  $\sigma$ -complex as an intermediate and the  $\text{sp}^2$  carbon transforms into the  $\text{sp}^3$  carbon. This stage needs barrierless (0.1 kcal/mol for the quartet and 0.6 kcal/mol for the sextet). The lack of resonance of the  $\sigma$ -complex causes smaller adsorption energy than the  $\pi$ -complex  $\sim 23$  kcal/mol for both spin states. Then 1,2-H shift takes place to form phenol. The activation energy of this stage was evaluated to be 25.2 kcal/mol on the sextet surface and 21.9 kcal/mol on the quartet surface. However the  $\sigma$ -complex can be transformed easily into cyclohexadienone. Therefore, they concluded that the oxygen-insertion mechanism is not preferably for benzene to phenol conversion over Fe-zeolite due to the branch reaction of cyclohexadienone. Additionally, the formation of a  $\sigma$ -complex is also found in the enzymatic cytochrome P450 system (de Vasser

and Shaik, 2003). The  $\sigma$ -complex can be a cationic or radical intermediate but the dominant channel proceeds via the cationic  $\sigma$ -complex (de Vasser and Shaik, 2003).

For the non-radical mechanism the authors assumed that the gas-phase benzene-phenol conversion by  $\text{FeO}^+$  should take place in a manner identical to the methane to methanol conversion (Yoshizawa *et al.*, 1998) with respect to essential features of the bonding:  $\text{FeO}^+ + \text{C}_6\text{H}_6 \rightarrow \text{OFe}^+(\text{C}_6\text{H}_6) \rightarrow [\text{TS1}] \rightarrow \text{HO-Fe}^+-\text{C}_6\text{H}_5 \rightarrow [\text{TS2}] \rightarrow \text{Fe}^+(\text{C}_6\text{H}_5\text{OH}) \rightarrow \text{Fe}^+ + \text{C}_6\text{H}_5\text{OH}$  where TS stands for transition state (Yoshizawa *et al.*, 1999). Benzene was adsorbed via a  $\pi$ -complex. The H atom abstraction proceeded via a four-centered TS1 while the phenyl migration occurred via a three-centered TS2. The bend  $\text{C}\cdots\text{H}\cdots\text{O}$  angle structure was found for TS1. Normally the direct H atom abstraction found in enzymatic system, cytochrome P450, occurs via a linear  $\text{C}\cdots\text{H}\cdots\text{O}$  angle transition state (Groves *et al.*, 1981). However, the previous publication of Yoshizawa (2000a) showed that the singly occupied  $3\sigma$  orbital and the partially filled  $2\pi$  orbitals of  $[\text{FeO}]^+$  played a vital role in H atom abstraction. The  $2\pi$  set are composed of d orbital of Fe and of  $\pi$  orbital of O. This leads to a bend  $\text{C}\cdots\text{H}\cdots\text{O}$  angle structure. The femtosecond dynamics simulation of the benzene-phenol conversion by monooxo-iron cation species in the gas phase was investigated (Yoshizawa *et al.*, 2000a). They found that the H atom abstraction of benzene required about 200 fs to be completed while it needed only 100 fs for phenyl migration to form phenol product. The simulations revealed that the H atom abstraction and the phenyl shift occurred via a one-step or concerted transition state. This reaction did not proceed via radical or ionic intermediates. This was confirmed by a model of mononuclear iron oxide cation in 3T zeolite cluster calculated by Yoshizawa (2000b). It was, however, in contrast to the mechanism for partial oxidation of benzene proposed by Burch and Howitt in which the reaction occurred via radical cation intermediate (Burch and Howitt, 1992). For the quartet state, the energy required for H-abstraction was 37.5 and 15.4 kcal/mol for gas phase (Shiota *et al.*, 2005) and the 3T cluster of ZSM-5 (Yoshizawa *et al.*, 2000b), respectively. The phenyl migration needed energy of 20.1 and 31.1 kcal/mol for gas phase (Shiota *et al.*, 2005) and the 3T cluster of ZSM-5 (Yoshizawa *et al.*, 2000b), respectively. For the

gas phase in the sextet state, energies of 48.4 and 32.0 kcal/mol were required for H-abstraction and phenyl shift, respectively (Yoshizawa *et al.*, 2000b). The authors concluded that among three pathways the non-radical mechanism is the most possible one.

Yoshizawa and co-workers suggested a model of mononuclear iron oxide cation in 3T zeolite cluster and demonstrated the reaction mechanism of direct oxidation of benzene-to-phenol as mentioned above (Yoshizawa *et al.*, 2000b). But in their model, an unrealistic conversion of  $\text{Fe}^{3+}$  to  $\text{Fe}^+$  species has not been experimentally proven in the condense phase. To avoid the present of  $\text{Fe}^+$  ion in zeolite,  $\text{N}_2\text{O}$  was loaded after the formation of  $\text{HO-Fe}^+-\text{C}_6\text{H}_5$  intermediate (Yoshizawa *et al.*, 2003). Then the  $(\text{O})(\text{OH})\text{Fe}^+(\text{C}_6\text{H}_5)$  intermediate was formed. This intermediate can transform to phenol via two pathways: i) phenyl group migrates to hydroxo group (OH) forming a phenol product, and ii) phenyl moiety shifts to oxo group (O) to form phenoxo group ( $\text{OC}_6\text{H}_5$ ) at iron center and then H transfers from OH group to  $\text{OC}_6\text{H}_5$  moiety obtaining phenol as the final product. The latter pathway preferred to take place because the activation energy of 7.0 kcal/mol for the  $\text{OC}_6\text{H}_5$  ligand formation was smaller than that of the phenol formation (13.9 kcal/mol) for the former pathway. However, the H-transfer of OH to  $\text{OC}_6\text{H}_5$  group was the rate-determining step with an energy barrier of 33.6 kcal/mol. While the phenol desorption needed energy of 23.8 kcal/mol. After the release of phenol, the  $[\text{FeO}]^+$  cluster of zeolite was generated. As a result,  $\text{N}_2\text{O}$  decomposition can play a vital role in starting a new cycle of benzene to phenol conversion. When the framework effect was taken into account, the transformation of the phenoxo ligand ( $\text{OC}_6\text{H}_5$ ) into phenol was the rate-limiting step with energy barriers of 22.1 and 16.1 kcal/mol for the sextet and the quartet, respectively (Shiota *et al.*, 2006).

### **Au(I) cation and $\text{Au}(\text{CN})_2^-$ anion in liquid nitromethane: quantum chemical calculations and molecular dynamics simulations**

Gold exists in solutions predominantly as colloidal gold, as Au(I) and as Au(III) cations. Au cations in both of these oxidation states are normally complexed

in solution and can easily transform or disproportionate into each other with Au(III) being normally the more stable and more strongly complexed oxidation state. Gold ions can also easily be reduced to neutral gold atoms which can form nanoclusters. There exist a large number of experimental works on gold ions in connection to nanotechnology but very few molecular dynamics studies on solutions of gold ions have been performed, however.

Au(I) and Au(III) is usually found in the gold complexes. Their structures have been studied via various experimental techniques. Farges et al. performed an EXAFS study on aqueous Au(III) chloride and found that gold exists as  $AuX_4$  complexes ( $X=Cl, OH$ ) at higher and at  $AuCl_4^-$  at lower pH values (Farges *et al.*, 1993). Bryce et al. studied gold(I) thiosulfate in aqueous solution by means of EXAFS measurements and density functional (Bryce *et al.*, 2003). They found a linear S-Au(I)-S coordination. Similar to  $[Au(NH_3)_2]^+$ ,  $[Au(P(OC_2H_5)_3)_3]^+$  and  $[Au(P(C_4H_9)_3)_3]^+$  cases, the Au-N and Au-P distances of these linear complexes were measured to be 2.02, 2.37 and 2.40 Å, respective, for  $[Au(NH_3)_2]^+$ ,  $[Au(P(OC_2H_5)_3)_3]^+$  and  $[Au(P(C_4H_9)_3)_3]^+$  (Kersti *et al.*, 2006). Recently, Cimatu and Baldelli studied the reaction of cyanide ions on gold surface by Sum Frequency Generation (SFG) technique. They assigned the peaks at 2140 and 2170  $cm^{-1}$  to symmetric and asymmetric  $Au(CN)_2^-$  stretches, and 2190-2225  $cm^{-1}$  to  $Au(CN)_4^-$  stretch. The peak at 2105  $cm^{-1}$  is the vibrational mode of linear  $CN^-$  adsorbed on Au surface (Cimatu and Baldelli, 2008).

The energetic, catalytic and electronic properties of Au(I) ion are usually compared with Cu(I) and Ag(I) cations because these monovalent ions have similar electronic configuration of fully-filled  $d^{10}$  orbitals. Therefore, clustering or solvation together with dynamics properties of Au(I) ion in any solvent can be compared with Cu(I) and Ag(I) cations as well. However, no theoretical studies of  $Au^+/Cu^+/Ag^+$  and nitromethane (NM) have been performed yet, although the hydration of these ions was elucidated by several groups (Iino *et al.*, 2007; Lee *et al.*, 2005; Reveles *et al.*, 2007; Rosi and Bauschlicher, 1989, 1990). Theoretical calculation is capable to obtain the knowledge of how to make up the cluster of  $Au^+/Cu^+/Ag^+$  and solvent. For alkali-

metal ions ( $\text{Na}^+$ ,  $\text{Mg}^+$ ,  $\text{Al}^+$ ), the clustering enthalpy is larger for the smaller ions and decreases monotonically with increasing number of solvent molecules (Dalleska *et al.*, 1994). In contrast, the first two solvent molecules, which then form a twofold linear coordination, are bound to  $\text{Au}^+/\text{Cu}^+/\text{Ag}^+$  much more strongly than the third and further ones (Iino *et al.*, 2007; Nilsson *et al.*, 2006). This result was explained in terms of the *sd*-orbital hybridization of  $\text{Au}^+/\text{Cu}^+/\text{Ag}^+$  (Ohashi *et al.*, 2009; Rosi and Bauschlicher, 1990, 1989). In the case of Au(I) case ten water molecules were needed to form a half sphere (Reveles *et al.*, 2007).

The structure of nitromethane (NM) had been studied by neutron diffraction (Megyes *et al.*, 2007). The intramolecular distances were determined to be  $1.19 \pm 0.01$ ,  $1.47 \pm 0.03$ ,  $2.12 \pm 0.02$ , and  $2.26 \pm 0.02$  Å for the N-O, C-N, O-O, and C-O bonds, respectively. Least-squares refined values for the X-H distances were  $1.07 \pm 0.01$  Å for C-H,  $2.06 \pm 0.03$  Å for N-H, and  $1.74 \pm 0.01$  Å for H-H.

No molecular dynamics (MD) simulations of gold ion in NM solution seem to have been published before but neat of solid/liquid NM has been studied by these means. Sorescu and co-workers (1997) developed an intermolecular potential for describing the structure of the  $\alpha$ -form of the hexahydro-1,3,5-trinitro-1,3,5-*s*-triazine (RDX) crystal which is a relative nitro compound. The potential formula of Buckingham (6-exp) and Coulomb (charge-charge) interactions were used for representing the intermolecular potential of this system. The atomic charges were obtained from ab initio calculations at MP2/6-31G(d,p) level. The values of the potential parameters were obtained by non-linear least-squares fitting and then were adjusted to reproduce the experimental data. The resulting parameter set was tested for checking its quality via isothermal-isobaric Monte Carlo (MC) and isothermal-isobaric molecular dynamics (MD) simulations. This potential function showed an accurate reproduction of the crystal properties (lattice dimensions, molecular orientation, and lattice energy). Additionally, the Buckingham parameters of the  $\alpha$ -form RDX can be applied for the intermolecular repulsion-dispersion force of nitramines and several classes of nitro compounds such as nitroalkanes, nitroaromatics, nitrocubanes, polynitroadamantanes, polynitropolycycloundecanes,

hydroxynitro derivatives, nitrobenzotriones, nitrobenzotriazoles, and nitrate esters (Sorescu *et al.*, 1998; Sorescu *et al.*, 1999). MC and MD simulations of such compounds showed that this potential model is able to accurately reproduce the experimentally determined crystallographic structures and lattice energies of these crystals. Therefore, the Buckingham potential function developed from the  $\alpha$ -form RDX can describe the properties of other nitro compound. This ability is called transferability. An intramolecular potential for solid nitromethane was developed in 2000 (Sorescu *et al.*, 2000). The data required for fitting the intramolecular potential were calculated at the B3LYP/6-31G(d) level while the published intermolecular function (Sorescu *et al.*, 1997) was chosen for testing the newly developed intramolecular potential. For simulations of liquid nitromethane (NM) and the resulting properties it can be referred to a recent paper (Megyes *et al.*, 2007) where classical and Car-Parrinello simulation results are compared with diffraction data. They found that ~13 NM molecules are in the first solvation shell. MD and CP-MD results also give the information concerning the orientations of the neighboring NM molecules. In liquid nitromethane only the first nearest neighbors tend to be oriented in an antiparallel form. For N-N distances  $>4.0 \text{ \AA}$ , NM molecules freely orientate.

#### **Effect of substituent group on dissociative electron attachment (DEA) of purines: quantum chemical study**

In gas phase experiments of DEA on nucleobases it was found that the bases may fragment into many species, depending on the incident electron energies (Abdoul-Carime *et al.*, 2001; Abdoul-Carime *et al.*, 2003; Abdoul-Carime *et al.*, 2004; Abdoul-Carime *et al.*, 2005; Denifl *et al.*, 2003a; Denifl *et al.*, 2003b; Denifl *et al.*, 2004a; Denifl *et al.*, 2004b; Denifl *et al.*, 2004c; Denifl *et al.*, 2007; Denifl *et al.*, 2008). The suggested mechanism of this is that the incoming electron is captured in a dipole-bound state due to a large dipole moment of such molecules and then it transfers to an antibonding  $\sigma^*$  orbital to form a metastable anion (Sommerfeld, 2004, 2005). Such an antibonding  $\sigma^*$  orbital is characteristically repulsive, meaning that it weakens the bond to which that orbital responds. As many as 6 product anions had been found for thymine (Denifl *et al.*, 2004b) e.g. dehydrogenated thymine anions

which lose mono- or more hydrogen atoms,  $C_4H_5N_2O^-$ ,  $OCN^-$ ,  $CN^-$  and  $O^-$  anion, and as 16 anions for adenine (Huber *et al.*, 2006), for example, dehydrogenated adenine anions, deaminated anion, deaminated anion,  $C_5HN_4^-$ ,  $C_2H_3N^-$ ,  $CN^-$  and  $H^-$ . It was also found that the N-H and C-H bonds dissociate more easily than the others (Denifl *et al.*, 2004b; Huber *et al.*, 2006). These bonds can be broken to form i) dehydrogenated anion + H atom or ii) dehydrogenated radical +  $H^-$  anion. However, only the H atom removal from nucleobases can be done by using very small electron energies below 1 eV (Abdoul-Carime *et al.*, 2004; Denifl *et al.*, 2007; Huber *et al.*, 2006). Electron energies of at least 6 eV were required for  $H^-$  anion detachment (Huber *et al.*, 2006). The most abundance of product anions was the H atom and its probability was  $\sim 230$  times higher than that of the  $H^-$  anion (Huber *et al.*, 2006).

More important, cross-section gas phase experiments of DEA on nucleobases also showed that the loss of H/ $H^-$  is a site- and bond-selective reaction. In order to clarify the bond-selectivity, pyrimidine nucleobases (thymine and uracil) were deuterated at carbon positions and after exposing LEEs, compared to undeuterated nucleobases, the peaks appearing above 7.5 eV and  $>2$  eV in the mass spectra correspond to the loss of  $D^-$  and D radical (or can be considering as the formation of dedeuterated anion) at carbon sites, respectively. While the peaks relating to DEA at nitrogen positions exist at 5.5-6.8 eV for  $H^-$  loss and at  $\sim 0.6$ -2 eV for the dehydrogenated anion formation of the deuterated molecule (Abdoul-Carime *et al.*, 2004; Ptasinska *et al.*, 2005a; Ptasinska *et al.*, 2005b; Ptasinska *et al.*, 2005c). Methylation at N1 site for thymine and at N3 site for uracil was performed for confirming site-selectivity of DEA on nucleobases. The peak of H losing from N1 site existed at lower energy ( $\sim 1$  eV) in mass spectra than at N3 site ( $\sim 1.8$  eV) (Ptasinska *et al.*, 2005d) while the  $H^-$  abstraction was recorded at 5.5 and 6.8 eV, respective, for N1 and N3 sites (Ptasinska *et al.*, 2005b). The study of DEA on deuterated and methylated pyrimidine bases at different carbon and nitrogen sites by Ptasinska *et al.* can identify that the resonance peaks appearing at 5.5, 6.8, 8.5 and 10 eV correspond to the  $H^-$  loss at N1, N3, C6 and  $CH_3$ , respectively (Ptasinska *et al.*, 2005a). This clearly revealed that DEA on pyrimidine nucleobases is both bond- and site-selective. The theoretical investigation of DEA on purine base (adenine) also confirmed this.

The electron energies needed for H atom lesion calculated at G2MP2 method were 0.94, 1.72, 2.53 and 3.63 eV for losing H at N9, N6, C8 and C2, respectively (Denifl *et al.*, 2007).

Additionally, the most easily dissociating H atom is the H at N1 position for pyrimidines (~0.6 eV; Abdoul-Carime *et al.*, 2004). Purine base (adenine) requires a slightly higher electron energy for losing its H atom at the N9 site, 0.7 eV (Abdoul-Carime *et al.*, 2004) and  $0.84 \pm 0.07$  eV (Denifl *et al.*, 2007).

Sommerfeld *et al.* showed that electron can transfer from dipole-bound to valence orbitals (Hendricks *et al.*, 1998; Sommerfeld, 2004). To study the dipole-bound state anion, the diffuse functions are necessary for calculating the extra electron in the molecule because the electron in the dipole-bound state stays out of the molecular framework. Hence, a special basis set which can represent a very diffuse orbital is needed. Even-tempered sequences of diffuse *s*, *p*, *d*, and *f* functions with the *n*th exponent  $\alpha_n$  given by  $\alpha_n = \alpha_1 q^{n-1}$ ,  $n = 1, 2, \dots$  (where  $\alpha_1$  is the value of the lowest exponent, *q* is the geometry progression parameter and *n* is the length of the sequence--*i.e.* the number of additional *sp* sets) are chosen to study the dipole-bound anions by several groups (Gu *et al.*, 2007; Gutowski *et al.*, 1998; Skurski *et al.*, 2000; Svozil *et al.*, 2005). Adamowicz's group always used the standard 6-31++G\*\*(5d) basis --which is augmented with six very diffuse Gaussian *sp* shell, with the exponents equal to 0.01, 0.002, 0.0004, 0.00008, 0.000016, and 0.0000032, and a *p* orbital with the exponent 0.036-- to study various nucleic acid base systems which have dipole moment larger than 3 debye (Jalbout and Adamowicz, 2001a, 2001b; Stepanian *et al.*, 2003).

As mentioned earlier, one channel, that transient molecular ion ( $A-B^*$  where A and B is covalented) obtained from LEEs attacking on nucleic acid bases can pass, is the dissociation pathway.  $A-B^*$  can be fragmented into  $A^-$  anion and  $B^\cdot$  radical. So neutral and anionic potential energy curves (PECs) as a function of the A-B bond coordinate indeed provide the knowledge of reaction mechanism. The neutral PEC is

of Morse character while a purely repulsive character is found for the anionic PEC. This is due to the fact that the incoming electron is captured and then located in the antibonding  $\sigma^*$  orbital which responds to A-B bond cleavage. This anionic curve has 2 important parts; 1) The stable part, at large A-B bond distances, it is an excited state but its energy lies below the neutral curve because the closed-shell  $A^-$  of the anion system is more stable than  $A^\cdot$  radical of the neutral, and 2) The metastable part at the medium and short A-B bond distances. Its energy lies above neutral because of the negative electron affinities (EAs) of neutral nucleic acid bases. As a result, there is a crossing region of these 2 curves. At the crossing point, in quantum theory, one eigenfunction cannot provide two eigenvalues, hence, this point does not exist. As a result of the avoided crossing, the potential energy curves are modified into the adiabatic PEC which consists of the neutral PEC in the left and the anion PEC in the right region of the crossing. These modified curves can explain the dissociative electron attachment. When the electron is captured by the neutral molecule, a vibrationally excited state can be formed which, depending on the details of the PEC, --the energy height of the  $\sigma^*$  anionic curve compared to the equilibrium structure of the neutral-- can tunnel through the barrier. Then the dissociative  $\sigma^*$  curve is reached and  $B^\cdot$  radical can be released.

For the anionic curve the problem in theoretical calculations lies in the complications that arise when going from static to time-dependent descriptions and in treating bound states and continuum states together. Depending on the energy of the incoming electron various approximate treatments can be applied. For “exact” calculations the so-called R-matrix method must be used (Feuerbacher *et al.*, 2004; Morgan *et al.*, 1998). This method divides the space around a molecule into an outer region, in which the electron is treated by electron-collision methods, and an inner region where the electron is treated by methods similar to the ones used in electron structure calculations. The R-matrix method is nowadays established (with commercially available software) and successful, but it is not universally applicable since the calculations are extremely demanding and in practice it can only be used for small molecules. Another technique that has been developed to get reliable energies of metastable anion is the Z-extrapolation or called charge-stabilization. The wave

function of metastable anion is stabilized by increasing certain nuclear charges ( $\delta q=1-5\%$ ) of atoms concerning bond-breaking and then extrapolating this plot to  $\delta q \rightarrow 0$  to obtain an estimate of the energy of the metastable anion for the actual molecule (Feuerbacher *et al.*, 2004).

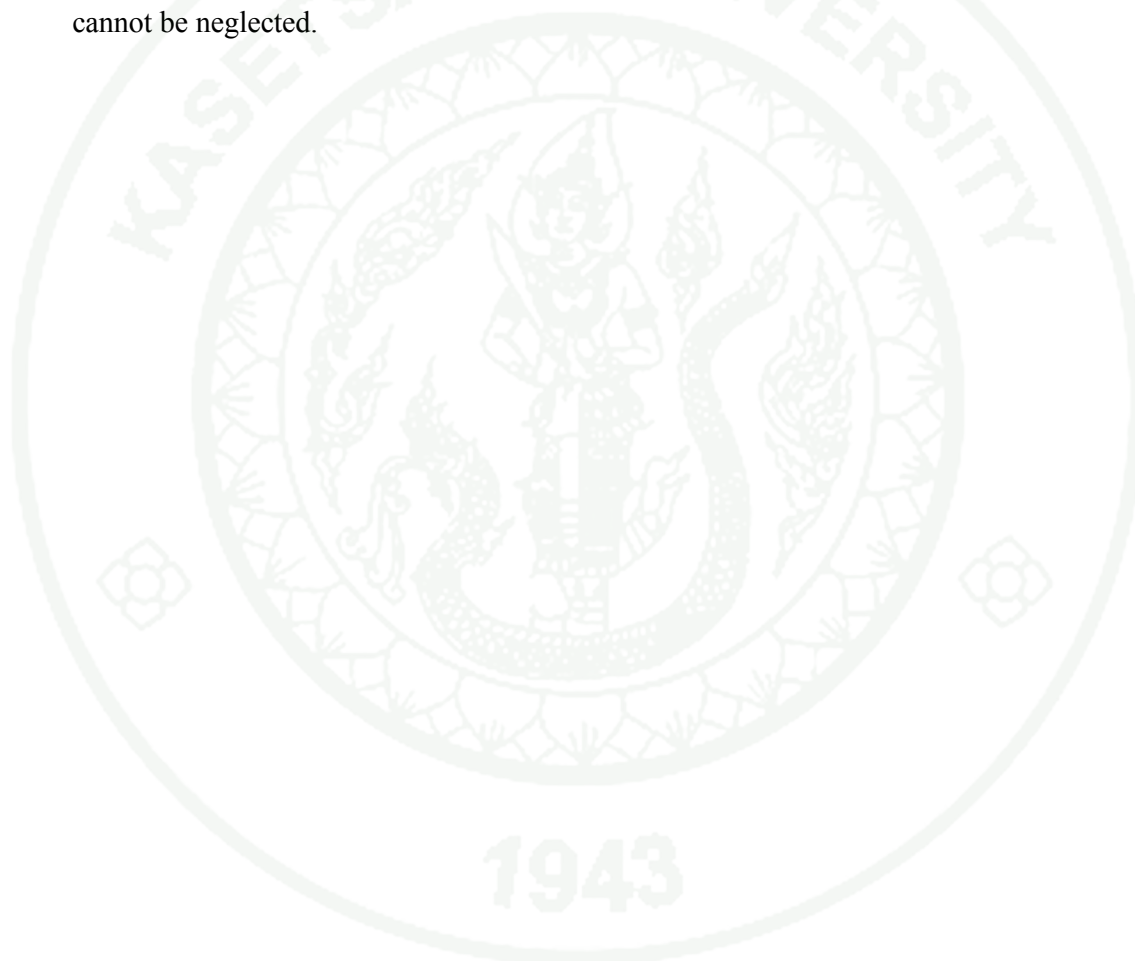
Numerous calculations have been performed with these methods. To simplify these calculations, many theoretical studies in the electron-DNA field always construct the neutral and anionic PECs by using standard calculation methods. But the problem is found in the metastable part which anion is less than its corresponding neutral. For small bond distances, the anionic energy equals to neutral energy plus free electron energy. To obtain the  $\sigma^*$  anionic potential curve at short A-B bond distances (metastable part), the Z-extrapolation is required (Feuerbacher *et al.*, 2004; Nestmann and Peyerimhoff, 1985; Theodore *et al.*, 2006; Whitehead *et al.*, 2002). However, this method is time consuming due to several calculations are needed for each distance. Therefore, Anusiewicz *et al.* proposed another model in order to eliminate the computational cost. The  $\sigma^*$  curve of anion in the metastable part can be extrapolated by using an exponential form such as  $C + A \exp[-b(R-R_c)]$ , where  $R_c$  is the value of R distance at which the  $\sigma^*$  energy intersects the neutral's energy curve and A, C, b are parameters whose values obtained by least-squares fitting (Anusiewicz *et al.*, 2005).

As mentioned earlier, in reality, the two potential energy curves interact with each other leading to an avoided crossing. The resulting curves can in principle be obtained from the equation

$$\begin{pmatrix} E^{upper}(r) \\ E^{lower}(r) \end{pmatrix} = EV \left( \begin{pmatrix} E^{neutral}(r) & C \\ C & E^{anion}(r) \end{pmatrix} \right)$$

where C is the interaction parameter governing the amount of the 'repulsion' between the curves. It can be estimated by various methods. EV(M) is the vector of the eigenvalues of M (Sommerfeld, 2005). Anusiewicz *et al.* suggested the easiest way to

obtain the avoided crossing. One charge-stabilization calculation was performed at the crossing point. The energy at this point was lowered in a small interval. Then the lower adiabatic anionic curve was obtained. The upper curve was corrected with the same interval energy (Anusiewicz *et al.*, 2005). However, only for small systems (2-3 atoms), the avoided crossing region can be calculated accurately. For large systems it is difficult to calculate and it has never been done because effects of other dimensions cannot be neglected.



## METHODS OF CALCULATIONS

### **Mechanisms and energetic of the direct benzene-to-phenol conversion on Fe-ZSM-5 zeolite: M06 density functional calculation**

The reaction mechanisms of benzene-to-phenol conversion have been investigated in the ZSM-5 zeolite cluster model of 3T (Yoshizawa *et al.*, 2003; Yoshizawa *et al.*, 2000b), 5T (Ryder *et al.*, 2003), 8T (Fellah *et al.*, 2009) and 10T (Kachurovskaya *et al.*, 2003). However, previous studies have shown that neglecting the framework effect leads to inconsistencies between cluster results and the substantial zeolite conduct (Kasuriya *et al.*, 2003; Limtrakul *et al.*, 2001; Namuangruk *et al.*, 2004; Panjan and Limtrakul, 2003; Rungsirirakun *et al.*, 2005). Although Kachurovskaya *et al.* (2004) investigated the benzene to phenol conversion over Fe-Ferrierite performed by periodic ab initio calculations, using VASP program, but it does not practical for the big unit cell of ZSM-5 zeolite. In recent studies, the authors have carried out QM/MM calculations for investigating the oxidation of methane to methanol (Pantu *et al.*, 2004), the benzene to phenol conversion (Shiota *et al.*, 2006) and the hydrolysis of methoxide species (Pabchanda *et al.*, 2005) and also found that the ONIOM model with the QM and MM parts treated with B3LYP and UFF, respectively, provides values that agree well with the experimental measurements. The interaction of  $Z[Fe^{III}O_2]^+/Z[Fe^{III}O]^+$  and benzene was studied by the popular B3LYP method (Ryder *et al.*, 2003; Shiota *et al.*, 2005; Shiota *et al.*, 2006; Yoshizawa *et al.*, 1999; Yoshizawa *et al.*, 2000a; Yoshizawa *et al.*, 2000b; Yoshizawa *et al.*, 2003). It is well-known that dispersion interaction is dominant in various aromatic molecules and cannot be described by the popular B3LYP functional. A M06 functional, one of the Minnesota functionals, includes a dispersion term and also has been suggested for various transition metals (Zhao and Truhlar, 2008b). Recent studies have shown that the Minnesota functionals are capable to study both zeolite cluster and large zeolite system treated with QM/MM approach (Boekfa *et al.*, 2009; Kumsapaya *et al.*, 2009; Zhao and Truhlar, 2008a). These make M06 a good candidate for studying this reaction. Therefore, in the present work, the quantum

chemical study on the hydroxylation of benzene over the dioxo-mononuclear iron species on ZSM-5 zeolite is reported by using the ONIOM approach at the M06 level of theory.

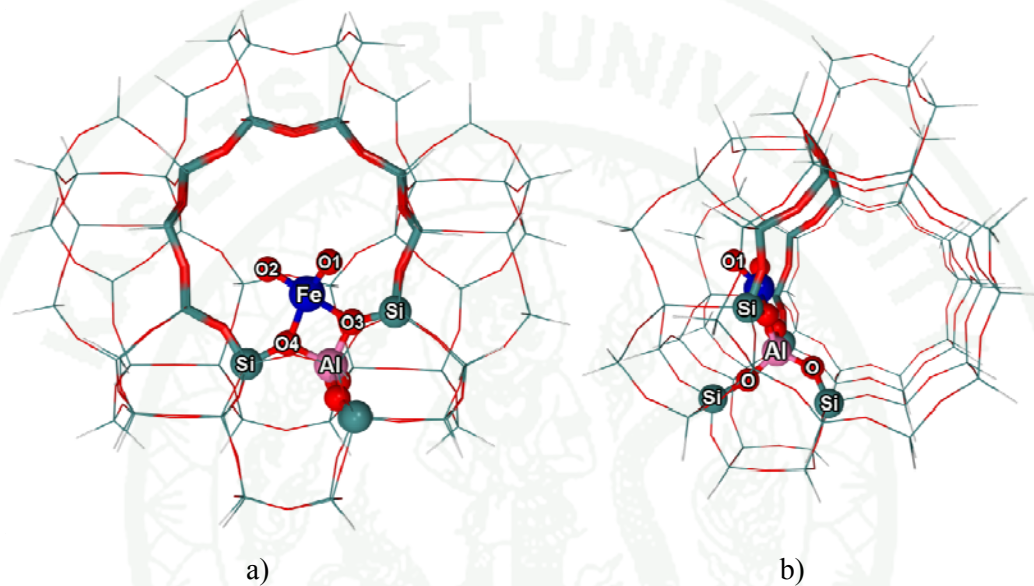


**Figure 1** Structure of 70T cluster model of Fe-ZSM-5 is taken from the straight channel (a) and the zigzag channel (b) views. Inner layer is presented as a stick style and a ball-and-stick style which is optimized. Outer layer is shown as a line style.

Due to the fact that  $\text{Fe}^{\text{I}}$  ion does not exist in the condense phase, this work will focus only on the  $[\text{Fe}^{\text{III}}\text{O}_2]^+$  and  $[\text{OFe}^{\text{III}}\text{O}]^+$  species to avoid the production of  $\text{Fe}^{\text{I}}$  ion after oxygenation of benzene. The structure of the 70T cluster model was taken from the crystal structure of the ZSM-5 lattice, see Figure 1. The selected 70T cluster model covers three different channel structures: the straight channel, the zigzag channel and the channel intersection; where reactions generally take place. One of the silicon atoms at the T12 position in the ZSM-5 zeolite was substituted by an aluminum atom and the negative charge of the cluster was balanced by oxo-iron(III) cation as mentioned above to form the active center. Due to the limitation of computational resources, the 70T cluster model was treated by the ONIOM2 scheme

in which the whole model is subdivided into two layers. The inner layer represents the reaction region. A 12T model including the active site and the benzene molecule, was treated with the unrestricted M06 functional using the 6-31G(d,p) basis set for all atoms except Fe atom was treated by using the effective-core pseudopotential (ECP) of Stuttgart and Bonn (Dolg *et al.*, 1987) to take care relativistic effects of Fe. The rest of the extended framework, up to 70T, was treated by the UFF method. During the geometry optimization only the 5T region,  $[(\equiv\text{SiO})_2\text{-Al-(O-Si}\equiv)_2]$ , the active  $[\text{OFe}^{\text{III}}\text{O}]^+$  or  $[\text{Fe}^{\text{III}}\text{O}_2]^+$  moieties and the adsorbates were allowed to relax as shown in a ball-and-stick style in Figure 1. For all transition states, normal mode analyses verified that only one imaginary frequency corresponding to the motion of atoms for each structure of transition state is present. Previous studies have reported that the sextet spin state was the most stable configuration for nitrous oxide decomposition (Ryder *et al.*, 2002) and partial oxidation of benzene over peroxy-iron ZSM-5 zeolite (Ryder *et al.*, 2003). Therefore, the spin states of all calculations in this work were kept at the high-spin sextet state. To improve and to obtain the reliable energies the full single point quantum calculation using UM06 level was performed at the optimized structure of all complexes obtained from ONIOM(UM06:UFF). All calculations were carried out with the MN-Gaussian 03 code (Frisch *et al.*, 2004).

1943

## **Au(I) cation and Au(CN)<sub>2</sub><sup>-</sup> anion in liquid nitromethane: quantum chemical calculations and molecular dynamics simulations**

This theoretical study consists of three sections: 1) quantum chemical calculations of the energetic and the clustering of gold ion and nitromethane (NM) molecules, 2) construction of intermolecular potential functions for Au<sup>+</sup>-NM and Au(CN)<sub>2</sub><sup>-</sup>-NM systems which then be used for describing the interaction between gold and NM in molecular dynamics (MD) simulations, and 3) MD simulations for obtaining the information about the behavior and the dynamics of gold ion/complex in the solution.

### 1. Quantum Chemical Calculations

Most of quantum chemical calculations were performed with the LANL2DZ (Hay and Wadt, 1985) basis set for Au and the D95V (Dunning and Hay, 1976) basis set for N, O, C and H. This choice of basis sets was motivated by the necessity of including relativistic effects for Au and the requirement that the LANL2DZ (Hay and Wadt, 1985) basis set and ECP which is often used successfully for Au (Pyykko, 2004b, 2005) must be combined with a same-quality basis for the lighter elements. The same basis sets were used in the work on the dicyanoaurate(I) anion. Normally, anions require more diffuse basis sets but the negative charge of Au(CN)<sub>2</sub><sup>-</sup> anion is distributed over all atoms. Therefore, at least concerning the energetics, a more compact basis set can be used. These basis sets are also practical to perform quantum chemical calculations on the larger clusters. As a method Hartree-Fock (HF) and MP2 levels were employed for constructing potential energy surfaces (PESs). The calculations were performed with and without basis set superposition error (BSSE). The HF method and basis sets as mentioned above were used to investigate the geometry, electronic structure, and the binding energy of Au<sup>+</sup>-NM<sub>n</sub> and Au(CN)<sub>2</sub><sup>-</sup>-NM<sub>n</sub> clusters with n = 1-10. NM is a molecule with a high dipole moment (4.6 debyes) and its electrostatic potential (ESPs) is divided into a positive half-space (CH<sub>3</sub>) and a negative one (NO<sub>2</sub>), see Figure 2a. Consequently the interaction of a free Au(I) ion with the NO<sub>2</sub> part of NM is attractive while the

interaction of Au(I) with the CH<sub>3</sub> part is repulsive. This is in contrast to Au(CN)<sub>2</sub><sup>-</sup> case in which the ESP of Au(CN)<sub>2</sub><sup>-</sup> is negative everywhere except close to the nuclei (Figure 2b). Consequently, the interaction of Au(CN)<sub>2</sub><sup>-</sup> with the NO<sub>2</sub> side of NM is repulsive and the one with the CH<sub>3</sub> side is attractive. The coordination of NM to Au(I) for both the free and the complexed Au(I) ion cases was studied in more detail. All quantum chemical calculations were carried out with the Gaussian 03 (Frisch *et al.*, 2004) computer program.

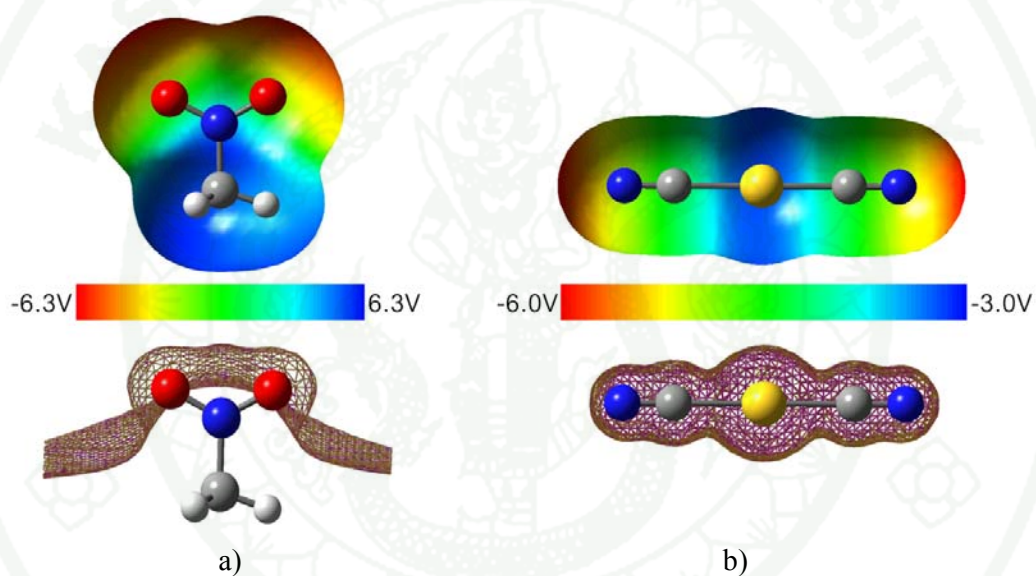


**Figure 2** Electrostatic potential (right) and the surface of zero ESP (left) of a) NM and b) Au(CN)<sub>2</sub><sup>-</sup>.

## 2. Potential Energy Surface

### 2.1 Au<sup>+</sup>-NM

Au<sup>+</sup>-NM and NM-NM intermolecular potential functions were developed for subsequently simulating Au(I) in liquid NM. An analytical pair potential for Au<sup>+</sup>-NM was constructed by fitting the parameters of functions of the interatomic distances to energies derived from quantum chemical calculations. Details

of these calculations were given in section 1 above. Au(I) coordinates (Figure 3) were generated along straight lines around a rigid NM molecule. In principle, it is not important how the conformation space is sampled unless important parts of it are left out. The subdivision of the sampling coordinates into straight lines only allows for an easy visualization of the potential energy in sets of distinct curves but does not enter into the fitting procedure. The  $q_i$  partial charges of NM were taken from (Sorescu *et al.*, 2001) as shown in Table 4 and fixed for all calculations in this work, for reasons of consistency ( $q_{Au} = 1$  a.u.). The equation and its parameters describing the  $Au^+$ -NM potential energy surfaces were obtained by minimizing the least-square deviation between the energies from the analytical formula and their quantum-chemically calculated counterparts.

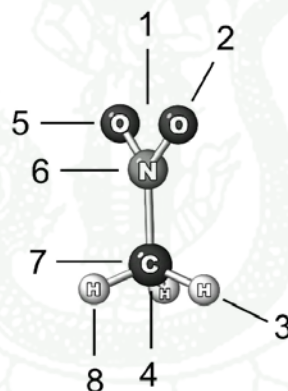


**Figure 3** Positions of  $Au^+/K^+$  around NM used for the construction of the  $Au^+$ -NM/ $K^+$ -NM potential energy function. The solid lines refer to movement of  $Au^+/K^+$ . The numbers of the lines refer to the energy curves in Figure 20 and 23.

## 2.2 $Au(CN)_2^-$ -NM, $K^+$ -NM and $K^+$ - $Au(CN)_2^-$

$Au(CN)_2^-$  anion can be prepared as an alkaline salt, for instance, as  $NaAu(CN)_2$  and  $KAu(CN)_2$ , by cyanidation of gold cluster (Cui and Zhang, 2008). Therefore, it is interesting to study the structure and dynamics of this ion-pair in

solution. To this aim,  $\text{Au}(\text{CN})_2^-$ -NM,  $\text{K}^+$ -NM and  $\text{K}^+$ - $\text{Au}(\text{CN})_2^-$  intermolecular potential functions were developed for investigating the dynamics of  $\text{Au}(\text{CN})_2^-$  anion and  $\text{KAu}(\text{CN})_2$  ion-pair in liquid NM. An analytical pair potential for these systems was constructed in the same way as described above.  $\text{K}^+$  coordinates around NM were generated in the same manner of  $\text{Au}^+$ -NM (Figure 3). The selected positions of  $\text{K}^+$  around  $\text{Au}(\text{CN})_2^-$  anion are shown in Figure 4. To construct an analytical potential function for  $\text{Au}(\text{CN})_2^-$ -NM, 22 orientations of the linear  $\text{Au}(\text{CN})_2^-$  anion around a rigid NM molecule were generated as shown in Figure 5. The  $q_i$  partial charges of  $\text{K}^+$  is 1 a.u. while the atomic partial charges  $q_i$  of  $\text{Au}(\text{CN})_2^-$  were calculated by the method and basis sets mentioned above. They are shown in Table 5.

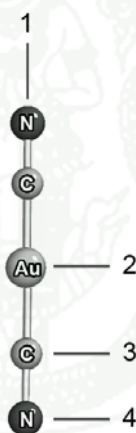


**Figure 4** Positions of  $\text{K}^+$  around  $\text{Au}(\text{CN})_2^-$  anion used for the construction of the  $\text{K}^+$ - $\text{Au}(\text{CN})_2^-$  potential energy function. The numbers of the lines refer to the energy curves of Figure 24.

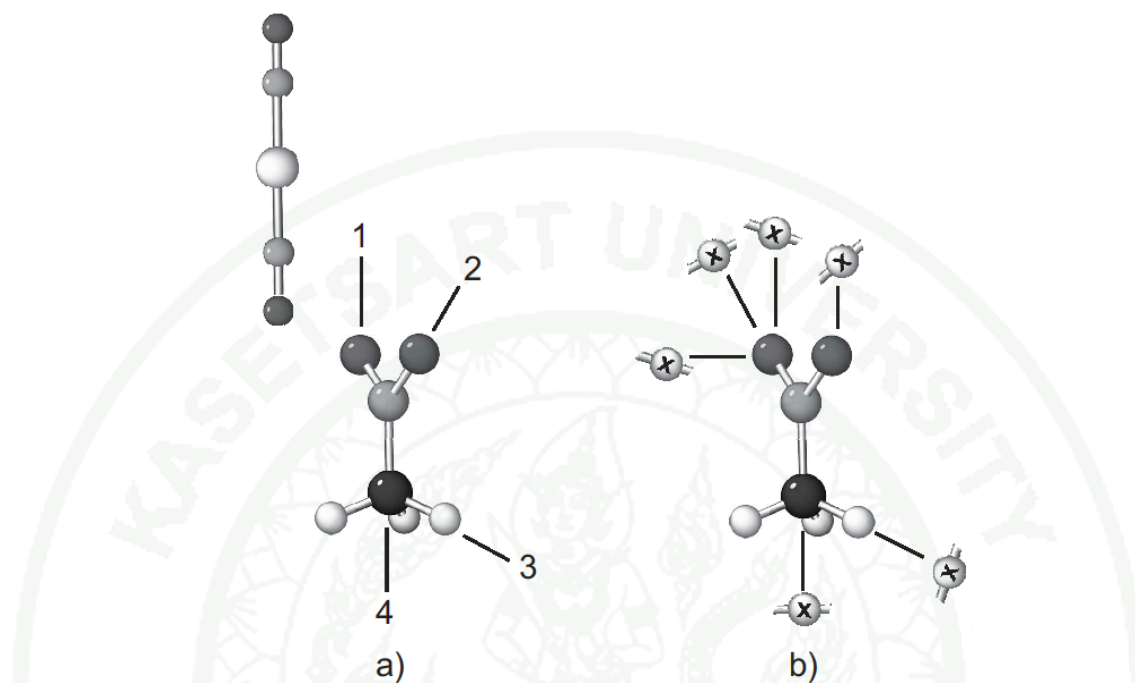


**Figure 5** Directions of the atom of  $\text{Au}(\text{CN})_2^-$  approaching to NM via a) the end-on by N atom of  $\text{Au}(\text{CN})_2^-$  and via b) the side-on of  $\text{Au}(\text{CN})_2^-$  where  $\mathbf{X} = \text{Au}, \text{C}$  and  $\text{N}$ .

### 2.3 NM-NM

An energy surface for the NM-NM interaction was calculated at the B3LYP/6-31+G(d) level and the corresponding potential energy function was constructed in the same fashion as mentioned above. This served the purpose of providing an independent check since the intermolecular part of the NM potential energy function previously used for simulations of liquid NM (Megyes *et al.*, 2007; Sorescu *et al.*, 2001) was derived from physical data of crystals of triazines (Sorescu *et al.*, 1997; Sorescu *et al.*, 2000). Its accuracy is therefore difficult to judge and besides the issue of transferability sometimes such potential energy functions are not accurate for liquid state simulations where much more mutual orientations of neighboring molecules play a role than in the crystalline phase. This potential energy function is subsequently referred to as the ‘generic NM pair potential’. The charges  $q_{ij}$

were fixed at the values given in (Sorescu *et al.*, 2001) in order of being able to use also the Au-NM energy function described above.

### 3. Molecular Dynamics Simulation

Two molecular dynamics (MD) simulations for the Au<sup>+</sup>-NM system were performed, one with the newly developed potential energy function for the NM-NM interaction and one with a previously published NM-NM potential energy function taken from the literature (Sorescu *et al.*, 2001). The cubic box contained 499 rigid NM molecules and one Au<sup>+</sup> cation. The boxlength of 35.561 Å corresponds to the volume occupied by 500 NM molecules at 300K and atmospheric pressure. A continuous negative charge distribution was neutralizing the box. Periodic boundary conditions were employed, together with the minimal image convention for the short-range forces. For the electrostatic forces the Ewald summation was used. The simulation was performed in the NVT ensemble at 300K. A timestep of 0.5 fs was chosen and the production run was performed for 77.5 ps after equilibrating the system for 22.5 ps. Before that, several equilibration cycles at high temperature with crude temperature scaling were employed to relax the system.

MD simulations of KAu(CN)<sub>2</sub> in liquid NM were performed by using the NM-NM intermolecular potential energy function developed in this work together with the Au(CN)<sub>2</sub><sup>-</sup>-NM, K<sup>+</sup>-NM and K<sup>+</sup>-Au(CN)<sub>2</sub><sup>-</sup> potential functions described in section 2.2 and 2.3. Two MD simulations were performed: (i) Au(CN)<sub>2</sub><sup>-</sup>-NM and (ii) KAu(CN)<sub>2</sub><sup>-</sup>-NM. The cubic box (35.561 Å boxlength) contained one Au(CN)<sub>2</sub><sup>-</sup> anion for each system and one K<sup>+</sup> cation for system (ii) while 460 and 459 rigid NM molecules were required for (i) and (ii), respectively. Other system parameters were the same as in the Au<sup>+</sup>-NM simulation. However, the production run of (i) and (ii) were performed for 980.0 and 967.5 ps, respectively, after equilibrating the system of 22.5 ps for (i) and 35.0 ps for (ii).

### **Effect of substituent group on dissociative electron attachment of purines: quantum chemical study**

This work focuses on the effect of substituent groups on dissociative electron attachment (DEA) of purine (Pu), adenine (Ad) and 6-fluoropurine (6-fPu) while the other 2 purines, 6-dimethyladenine (6-dimAd) and 8-fluoropurine (8-fPu) were studied in this work to complete some results. The structure and the numbering of all compounds are shown in Figure 6. Experimental and theoretical studies observed site- and bond-selective of LEE on nucleic acid bases (Abdoul-Carime *et al.*, 2004; Denifl *et al.*, 2007; Ptasinska *et al.*, 2005a; Ptasinska *et al.*, 2005b; Ptasinska *et al.*, 2005c; Ptasinska *et al.*, 2005d). Moreover, the substituent groups at C6 of purine cause different mass spectra of dehydrogenate  $M^-$  anions (Denifl *et al.*, 2007).

Therefore, three different topics have been concentrated. The first concerns the question which hydrogen dissociates most easily. To answer this, bond dissociation energies (BDE) and energies required for the dissociative electron attachment ( $E_{DEA}$ ) of hydrogens are calculated. Secondly, why the purine derivatives show different spectra is needed to find out. Analyses of electronic properties such as electrostatic potential (ESP) and molecular orbitals can explain this question. The last topic is why different energies are required for removing hydrogen from the same site of similar purines. Neutral and anionic potential energy surfaces (PES) should be constructed to show where they cross and how high the barrier for losing the hydrogen atom is.

All calculations were carried out with the Gaussian 03 set of programs.

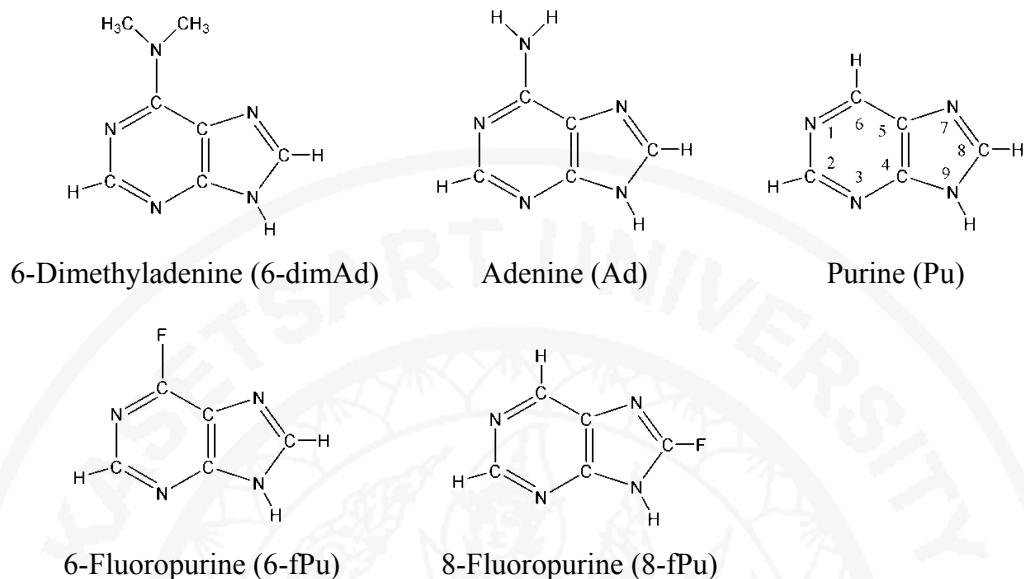


**Figure 6** Structure and standard numbering of all studied purines.

### 1. Energetics

Ad and Pu have hydrogen atoms at four ring positions if one regards the two hydrogens of the  $\text{NH}_2$  of Ad as equal while 6-fPu has hydrogen atoms at three ring positions. These molecules have negative electron affinities (EA). This means that molecule (MH) with the electron at 'infinite distance',  $(\text{MH} + e^-)$ , has a lower energy than 'real' anionic states. These anions are in a metastable state. The exact energy of  $(\text{MH} + e^-)$  is the same as of MH and quantum chemical calculations on  $(\text{MH} + e^-)$  approach this value from above upon increasing basis set. In reality a metastable anion  $(\text{MH}^*)$  is formed. The energy required for reaction (1) is called  $E_{\text{DEA}}$  and must be discussed together with the bond dissociation energy (BDE) (2), for understanding the dissociation. Reliable BDEs and  $E_{\text{DEA}}$  have been calculated with the G2MP2 quantum thermochemical extrapolation method (Curtiss *et al.*, 1993). This method has an accuracy of at least  $\pm 0.09$  eV for calculating atomic and molecular electron affinities (Rienstra-Kiracofe *et al.*, 2002).





The dehydrogenated  $\text{M}^{\cdot}$  anion is a closed-shell molecule while  $\text{M}^{\cdot} + \text{H}^{\cdot}$  is a biradical system. This reaction competes with autodetachment which gives  $\text{MH} + e^{-}$  as products. An important value of the dissociative electron attachment is the adiabatic electron affinity (AEA) of the  $\text{M}^{\cdot}$  radical. The dissociative electron attachment is more favorable than autodetachment if  $\text{AEA}(\text{M}^{\cdot})$  is a large positive value. The BDE,  $E_{\text{DEA}}$  and AEA are calculated from the supermolecular approach using the following relationships:

$$\text{BDE} = E(\text{M}^{\cdot}) + E(\text{H}^{\cdot}) - E(\text{MH}) \quad (3)$$

$$E_{\text{DEA}} = E(\text{M}^{\cdot}) + E(\text{H}^{\cdot}) - E(\text{MH}) \quad (4)$$

$$\text{AEA} = E(\text{M}^{\cdot}) - E(\text{M}) \quad (5)$$

where E stands for energy of anion or neutral at the optimized geometry.

## 2. Electronic properties

Analysis of some electronic properties can show some information about DEA of purines. The molecular dipole moment should be an important quantity since the incoming electron is firstly trapped in the dipole-bound state (DBS) and then tunnels to other valence molecular orbital. Often electrostatic potential (ESP) provides additional information about the similarities and differences of the compound and its derivatives. Moreover it is essential to analyze some molecular orbitals that may concern i.e. the highest occupied molecular orbital (HOMO) and other lower orbitals (HOMO-n), the lowest unoccupied molecular orbital (LUMO) and other higher orbitals (LUMO-n), the singly occupied molecular orbital SOMO. All of these are obtained by using the unrestricted B3LYP density functional (UB3LYP) and the basis set of cc-pVTZ.

### 3. Potential energy surfaces

For a detailed understanding of the reaction mechanism a knowledge of the relevant potential energy curves is prerequisite. Experiments (Denifl *et al.*, 2007) and theoretical calculations (Denifl *et al.*, 2007; Evangelista *et al.*, 2004) including the results that will be presented in the next section have been observed that H atom at N9 site is most easily detached. Therefore, the approximation of a one-dimensional reaction coordinate N9-H seems justified.

For the neutral potential energy surface the dissociation of H atom from N9 site occurs via a homolytic bond breaking which  $M_{N9}^{\cdot}$  radical and hydrogen atom are the dissociative products. This reaction concerning biradical species should in principle be calculated by means of multireference calculations such as CAS or MCSCF methods. Since the  $\sigma^*$ -orbital that is mostly responsible for the N9-H bond is spread out over several atoms (Figure 38) which, together with the size of the systems and the other molecular orbitals of similar energies makes such calculations of the multireference type difficult. The calculation of the neutral potential energy curves poses only the general problem of an accurate description of homolytic bond breaking which poses accuracy problems but can be treated by standard electronic structure theory. Unrestricted density functional theory (DFT) can provide a reasonable description of homolytic bond breaking (Gräfenstein *et al.*, 2002). At long  $r[N9-H]$  distances ( $\sim 7.0$  Å) a proton always detaches instead of neutral H atom. This is due to the closed-shell  $M^-$ , for  $MH \rightarrow M^- + H^+$ , is more stable ( $\sim 3.5-4.5$  eV) than  $M^{\cdot}$  radical, for  $MH \rightarrow M^{\cdot} + H^{\cdot}$  reaction. However a high ionization potential (IP) of H of 13.6 eV is required for  $H \rightarrow H^+ + e^-$  reaction. As a consequence, the energy needed for reaction H atom abstraction is smaller ( $\sim 10$  eV) than that for proton removal. In order to represent the biradical system of process (2) a 'alter' keyword is used for obtaining H as a dissociative product. As a result of such keyword an electron from an occupied molecular orbital is moved into an unoccupied 1s molecular orbital of H. Normally, this orbital is LUMO+3 for all purines. The energy of the modified wave function should be equal to the BDE. Now the wave function representing  $M_{N9}^{\cdot}$  radical and H

atom at  $r = 7.0 \text{ \AA}$  is obtained. Then its coefficient parameters are used as a starting guess for the calculations of the energy from  $r = 4.0 \text{ \AA}$  to  $0.6 \text{ \AA}$ .

In the equilibrium structure of the neutral molecule (short N9-H distances) all anions are metastable (less stable than the neutral species). At larger N9-H distances, however, some anion states become energetically more favorable than the neutral molecule, meaning that the neutral and anionic  $E=f(r[\text{N9-H}])$  curves have to cross each other. In the region left of this crossing ( $r[\text{N9-H}] \sim \leq 1.4$ ) the anion is not stable and the exact energy of  $(\text{MH} + e^-)$  is the same as of MH, therefore, its energy cannot be calculated by standard quantum chemical methods. The anionic energy curves are in principle more difficult to calculate. From the molecular orbital analysis it can be seen from the symmetry of the LUMO and the higher unoccupied molecular orbitals of the neutral species that the state that responsible for bond weakening/breaking is not the (stable or metastable) anionic ground state. It is inspected that this MO graphically to see if it exhibits  $\sigma^*$ - character at the N9-H bond. The single electron of the anion at its lowest energy normally occupies a  $\pi^*$ -MO with a zero density in the molecular plane and therefore does not influence the N9-H bond. It is the lowest (or next-to-lowest)  $\sigma^*$ -MO that can weaken this bond. All these states are, however, quite close in energy. At longer N9-H distances the anion is stable in the corresponding geometry and it poses no special problem to calculate the anion in the  $\sigma^*$  state which is assumed to be responsible for dissociation (some care must be taken since in the anionic ground state the excess electron usually occupies a  $\pi^*$ -orbital). At shorter N9-H distances the anionic state crosses the neutral curve and the anion gets metastable with respect to autodetachment of the electron.

In this study the potential energy curves (PECs) of the neutral and anionic species as a function of the N9-H distance were calculated by means of the following methods.

### 3.1 Calculation of anionic states

All calculations were performed at the equilibrium structure of neutral molecule. The neutral PEC is calculated at the UHF/aug-cc-pVTZ method and basis set as the technique described above. To obtain the anionic PEC the molecule is divided into two spaces. The inner space around a molecule is treated by standard method; here is unrestricted Hartree-Fock method. The outer space is treated by the electron collision method -- the 'Outer Valence Green's Function (OVGF)' method. This method gives quite accurate values of ionization and electron attachment energies. Therefore the following procedure was applied for obtaining the required anionic PEC:

- 1) Construct the neutral PEC concerning  $MH \rightarrow M + H^+$  reaction in order to obtain the inner space curve. Some care must be taken that any occupied MOs at large  $r[N9-H]$  has no wave function on  $H^+$ .
- 2) Identify the lowest  $\sigma^*$ -orbital from a UHF calculation of the neutral molecule using the aug-cc-pVDZ basis set. Normally, it is LUMO for all purines.
- 3) Inspect this MO graphically to see if it exhibits  $\sigma^*$ -character at the N9-H bond. This orbital will be treated as the outer space.
- 4) Calculate its energy by means of UOVGF method at the aug-cc-pVDZ basis set as a function of  $r[N9-H]$ . The resulting electron affinity (EA) curves are smooth and cross the  $E=0$  line at about  $r[N9-H] \approx 1.4 \text{ \AA}$ . Only large positive values are physically meaningful for the left of the crossing. The small positive or negative values are replaced by charge-stabilization or polynomial extrapolation methods of the positive branch towards smaller distances as described following.

#### 4.1) The stabilization method

At  $r[\text{N9-H}] \leq 1.4 \text{ \AA}$  certain nuclear charges ( $\sim \delta q$ ) of atoms concerning bond-breaking is increased only 1-5%. For values of  $\delta q$  large enough to make large negative EAs. At least 3 nuclear charge stabilization calculations are needed for each  $r[\text{N9-H}]$ . One then extrapolates this plot to  $\delta q \rightarrow 0$  to obtain an estimate of the energy of the metastable anion for the actual molecule (with  $\delta q = 0$ ), see Figure 7. The extrapolation is carried out using a second order (in  $\delta q$ ) polynomial. This method is assumed to be accurate one because wave functions of a few atoms have been perturbed (Feuerbacher *et al.*, 2004; Nestmann and Peyerimhoff, 1985; Theodore *et al.*, 2006; Whitehead *et al.*, 2002).

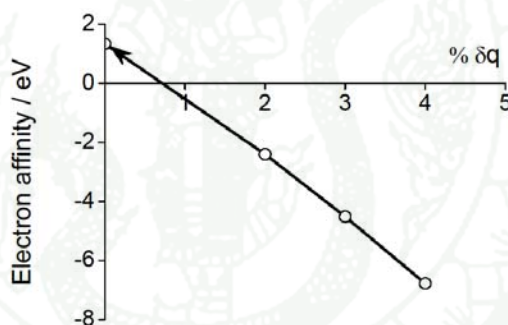


**Figure 7** Charge-stabilization plot of electron affinity (eV) as functions of the added nuclear charge ( $\delta q$ ) for each N9-H bond length.

#### 4.2) Extrapolation method

Due to at least 3 nuclear charge stabilization calculations are needed for each distance leading extremely computationally consuming. So it would be easy to obtain the anionic curve by extrapolating the curve at  $r[\text{N9-H}] \sim 1.4\text{-}3.0 \text{ \AA}$  using least-squares fitting or second order polynomial to the small N9-H distances. A dashed line in Figure 8 is obtained from the extrapolation method.

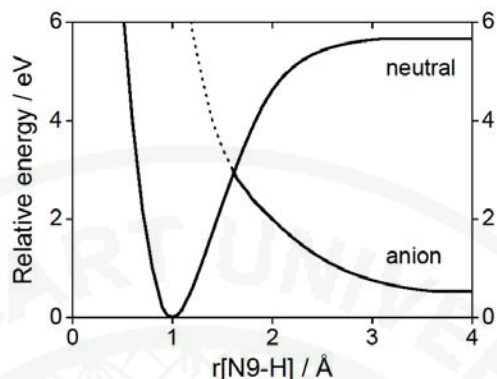


**Figure 8** Dashed line: metastable part of anionic potential energy curve obtained by the extrapolation method, see text.

5) The total energy of the anion is obtained by adding the EA curves and the neutral potential energy curve from 1). The anionic potential energy surface can be obtained by this equation:

$$E_{anion} = E_{neutral} + EA \quad (6)$$

### 3.2 Density functional Theory

In this method the adiabatic potential energy surfaces of the neutral and anionic species as a function of the N9-H distance were calculated by means of the unrestricted density functional UB3LYP and the pVTZ basis set. Wesolowski and co-worker showed that the B3LYP method gives reliable adiabatic electron affinities (AEA) of the DNA and RNA bases (Wesolowski *et al.*, 2001). The structure of purines was optimized at each N9-H distance. The neutral curve is obtained as mentioned in section 3.

The methods described above do not give the actual wave functions of metastable anions. Their electronic properties are not obtained (although they also could be approximated). It would be better to gain the real wave function at  $r[\text{N9-H}] \sim \leq 1.4 \text{ \AA}$  to see what the excess electron is doing in the molecule. Therefore, in this

work, UB3LYP/cc-pVTZ calculations are additionally performed in a simple way in order to obtain the metastable anionic potential energy curve. For the anionic PEC, the excess electron is in the valence orbital corresponding to the N9-H bond cleavage. Therefore, the diffuse functions are not required for this calculation because, at equilibrium structure of neutral molecule, the diffuse functions allow the excess electron stays outside the molecular framework to dipole-bound or continuum states. But, for bond cleavage, the excess electron must be in the valence orbital, therefore, the excess electron can be in the  $\sigma^*$  N9-H orbital if basis sets without diffuse functions are chosen (Li *et al.*, 2002). At the stable part ( $r[\text{N9-H}] \approx 1.5\text{-}4.0 \text{ \AA}$ ) of the anionic curve the extra electron occupies in the  $\sigma^*$  N9-H orbital. The symmetry of  $r[\text{N9-H}] = 1.5 \text{ \AA}$  wave function is kept to use as starting guess for the calculation at  $r[\text{N9-H}] = 1.4 \text{ \AA}$  by using the ‘scf=(symm,verytight)’ keyword, and so on.

Moreover, anharmonic N9-H stretching vibrational energy levels of the neutral curve are important when considering the threshold energy required for dissociation. These vibrational energy levels can be calculated by taking advantage of the fact that this PEC closely resembles a Morse potential:

$$E(v) = hv_0(v + 1/2) - \frac{[hv_0(v + 1/2)]^2}{4D_e} \quad (7)$$

$$v_0 = \frac{\alpha}{2\pi} \sqrt{2D_e/m} \quad (8)$$

$$\alpha = \sqrt{k_e/2D_e} \quad (9)$$

$$k_e = m(2\pi v)^2 \quad (10)$$

Where  $h$  = Planck constant

$v$  = the vibrational quantum number

$D_e$  = the well depth (defined relative to the dissociated atoms)

$m$  = molecular mass

$k_e$  = the force constant at the minimum of the well depth

$v$  = N9-H stretching frequency which is scaled by the factor of 0.9804 for zero-point energy of B3LYP/6-31G\* method and basis set (Wong, 1996).

## RESULTS AND DISCUSSIONS

Previous 'method' section explains how to get the information of the studies systems. The details of the above studies are shown in the followings.

The direct benzene-to-phenol conversion on Fe-ZSM-5 has been elucidated via ONIOM2(UM06:UFF) approach. The dioxo-iron ( $\text{FeO}_2^+$ ) center is proposed to be the active center of Fe-ZSM-5. The most possible mechanism pathway is that benzene is favorably activated by  $\alpha$ -oxygen of the active dioxo-iron center via electrophilic aromatic substitution than the H-abstraction of benzene molecule. The  $\sigma$ -adduct --the product of electrophilic substitution-- further transforms into the very stable hydroxo-phenoxo intermediate via two pathways that will be addressed in detail next. Finally, the hydroxo hydrogen shifts to the phenoxo oxygen for phenol formation. The step is proposed to be a rate-determining step for the total reaction mechanism of benzene-to-phenol conversion when the phenol desorption is taken into account. The activation energy of this step is 45.67 kcal/mol.

Au(I) cation and  $\text{Au}(\text{CN})_2^-$  anion in liquid nitromethane were studied via both quantum chemical calculations and molecular dynamics (MD) simulations. Beside the quantum calculations were performed for obtaining the energetic and the clustering of gold ion and nitromethane (NM) molecules, it is also used for constructing potential energy functions which are the important parameters for describing the interaction between gold ion and NM in MD simulation. The resulting radial distribution function (RDF) of  $\text{Au}(\text{CN})_2^-$  in liquid nitromethane obtained from the MD simulation is in good agreement with the one obtained from an X-ray diffraction experiment.

The theoretical investigation can successfully address the effect of substituent group on dissociative electron attachment of gas phase purines which is shown in the third topic. The results will show that the different substituent groups at the C6 site of purine significantly affect the electron energy required for releasing hydrogen atom from different sites. The electron-withdrawing F atom of 6-fluoropurine causes less

electron energies needed for hydrogen loss compared to purine while the electron-donating  $-\text{NH}_2$  group of adenine does the opposite. The reasons for this can address by four factors: electrostatic potential, the energy level of virtual  $\sigma^*$  molecular orbitals, electronegativity of atoms and electron affinity of dehydrogenated radical.

### **Mechanisms and energetic of the direct benzene-to-phenol conversion on Fe-ZSM-5 zeolite: M06 density functional calculation**

#### 1. Structure of the $\alpha$ -site

The optimized structures of peroxo-iron  $Z[\text{Fe}^{\text{III}}\text{O}_2]^+$  and dioxo-iron  $Z[\text{OFe}^{\text{III}}\text{O}]^+$  species are shown in Figure 9. All oxo-iron intermediates are coordinated with the two bridging oxygen atoms of zeolite framework in the form of bidentate interactions which the distances between Fe and oxygen (O3 and O4) atoms of zeolite are in range 1.9-2.0 Å. The distance between Fe and Al is about 2.8 Å which agrees well with EXAFS measurements of 2.9 Å for the dioxide and the dihydroxide forms of the mononuclear iron species (Choi *et al.*, 2004; Choi *et al.*, 2003). In the peroxo case, the  $\text{Fe-O}_\alpha$  distance is about 1.93 Å whereas it is 1.66 Å in the dioxo case. The distance between Fe and  $\alpha$ -oxygen atoms (O1 and O2) is about of 1.66 Å which is close to the bond distance between an active oxygen atom bound to the non-heme iron in the enzyme cytochrome P450cam about 1.65 Å (Green *et al.*, 2004). The peroxo form is more stable than the dioxo one by about 14.90 kcal/mol. However, their orientations are different in which Fe coordinated with four oxygen atoms is in a tetrahedral shape for the peroxo while it is a distorted square planar for the dioxo. Moreover, these isomers can transform to each other via transition state TS\_1. Energy required for the dioxo-to-peroxo transformation is only 8.18 kcal/mol.

A population analysis is used to calculate the atomic spin density ( $\rho$ ) of system. For  $Z[\text{OFeO}]^+$ , the spin density of two  $\alpha$ -oxygen atoms,  $\rho(\text{O}_\alpha)$ , are  $\sim 1.0e^-$  and the atomic charges are about -0.34, therefore, the  $\text{O}_\alpha$  atoms of  $Z[\text{OFeO}]^+$  belong to an anion radical species, in agreement with experiment (Starokon *et al.*, 2003). Similarly,

the  $O_{\alpha}$  atoms of the peroxy-iron  $Z[FeO_2]^+$  is also an anion radical but it is less reactive than  $Z[OFeO]^+$  due to a small  $\rho(O_{\alpha})$  of  $\sim 0.6e^-$ . Although  $Z[OFeO]^+$  is less stable than  $Z[FeO_2]^+$  but  $O_{\alpha}$  atoms of  $Z[OFeO]^+$  are more reactive. Consequently, the dioxy form is chosen to represent the  $\alpha$ -site for studying the mechanisms of benzene-to-phenol conversion in the next section.

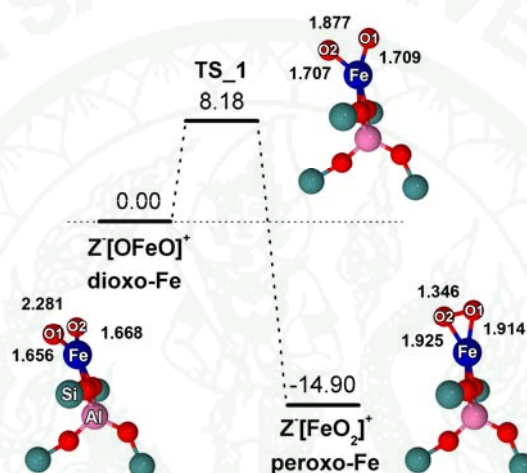


**Figure 9** Relative energies and optimized structure together with some selected parameters of  $Z[FeO_2]^+$ ,  $Z[OFeO]^+$  and transition state (TS\_1) taken from zigzag channel of ZSM-5. Energies are given in kcal/mol and distances are given in angstroms.

## 2. Benzene adsorption

The calculations show that benzene molecule can be adsorbed on the active  $[OFe^{III}O]^+$  center of ZSM-5 via two- and three-centered adsorption forms. In the two-centered complex, a  $p$  orbital of one carbon donates electrons to a hybrid  $sdp$  orbital of Fe which acts as an acceptor. This adsorption complex is called as '**1d1a**'. The similar interaction is also found in the case of three-centered adsorption form but the  $p$  orbital of two carbons act as donators. This form is named as '**2d1a**' complex. From NBO analysis of these complexes, the stabilization energy  $E(2)$  obtained by donation from the donor to the acceptor are high (29.17 and 34.64 kcal/mol, respective for

**1d1a** and **2d1a**) indicating the strong interaction between Fe and benzene molecule. This does significantly disturb the structure of the benzene molecule in which hydrogen atoms at the attached carbons are distorted from the molecular plan ~2-4 degree. Although  $E(2)$  of **2d1a** is larger than that of **1d1a**, the adsorption energy of these two forms is similar (-32.02 kcal/mol for **1d1a** and -32.05 kcal/mol for **2d1a**). The optimized structures of benzene adsorbed on Fe-ZSM-5 are shown in Figure 10. For **2d1a**, the distance of Fe...C1 and Fe...C2 are 2.599 and 2.716 Å, respectively. In **1d1a** complex, only C1 atom sits near Fe<sup>III</sup> ion and the Fe...C1 distance is 2.544 Å while the distance of Fe...C2 is 2.909 Å.

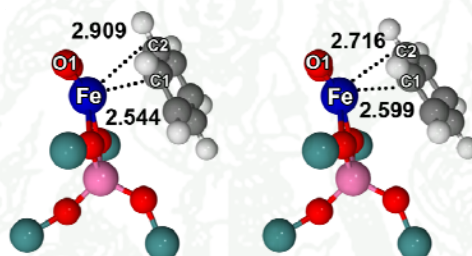


**Figure 10** Optimized structure of **1d1a** (left) and **2d1a** (right) adsorption complex together with the Fe...C distances. Distances are given in angstroms.

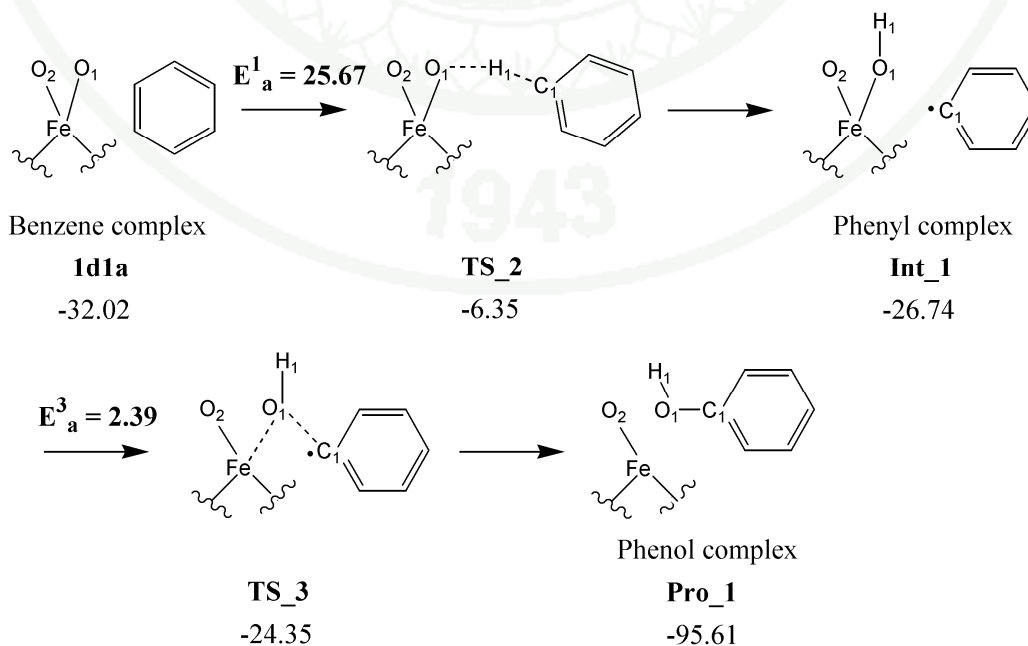
### 3. Reaction mechanisms

3.1 Is benzene activated via a hydrogen abstraction or an electrophilic aromatic substitution?

Three different pathways have been proposed for activating benzene molecule; the hydrogen abstraction yielding a phenyl complex (Shiota *et al.*, 2005; 2006; Yoshizawa *et al.*, 2000a; Yoshizawa *et al.*, 2000b; Yoshizawa *et al.*, 2003), the oxygen insertion into the C-H bond (Fellah *et al.*, 2009; Ryder *et al.*, 2003) and the electrophilic substitution to give benzene oxide (Kachurovskaya, 2004; Kachurovskaya *et al.*, 2003) and an  $\sigma$ -adduct (Bassan *et al.*, 2003; de Visser and Shaik, 2003; Shiota *et al.*, 2005; Yoshizawa *et al.*, 2003). Based on experimental

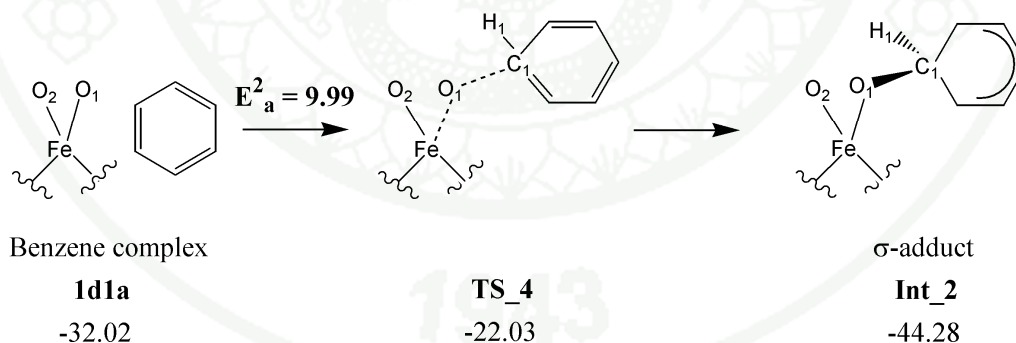
results, it was found that the oxidation of aromatic molecule catalyzing with P450 enzyme proceeds via the electrophilic substitution mechanism (de Visser *et al.*, 2007). Unlike the partial oxidation of aromatic, the hydrogen abstraction step is a key role step in converting the aliphatic molecule to the corresponding alcohol not only in enzyme (de Visser *et al.*, 2007) but also in zeolite (Dubkov *et al.*, 1997). Theoretical study showed that benzene oxide should be formed via the  $\sigma$ -adduct for the non-heme system (Bassan *et al.*, 2003; de Visser and Shaik, 2003) and in zeolite (Yoshizawa *et al.*, 2003). Therefore, the oxygen insertion and the electrophilic substitution to benzene oxide are not considered in the present work. Therefore, this work will focus on the hydrogen abstraction and the electrophilic aromatic substitution to the  $\sigma$ -adduct pathways. One of the aims of this work is to confirm that the electrophilic substitution occurs more easily than the hydrogen abstraction.

The **1d1a** complex can be activated by both a hydrogen abstraction and by electrophilic aromatic addition. Figure 11 shows their energetic profiles and the optimized structures obtained from quantum calculations. The hydrogen abstraction occurs via TS\_2 by a direct attack of  $\alpha$ -oxygen O1 to H1 atom of benzene to form phenyl and hydroxyl moieties as an intermediate Int\_1 as the following scheme shows 2-dimensions of this mechanism.



This benzene activation pathway was proposed by Yoshizawa in the gas phase (Shiota *et al.*, 2005; Yoshizawa *et al.*, 2000a; Yoshizawa *et al.*, 1999) and zeolitic systems phase (Shiota *et al.*, 2006; Yoshizawa *et al.*, 2003; Yoshizawa *et al.*, 2000b). Next the phenyl moiety shifts to the hydroxyl group yielding phenol as a product. This step takes place rapidly ( $E_a = 2.39$  kcal/mol) due to Int\_1 is a very reactive phenyl radical, whose spin density and atomic charge are  $0.80e^-$  (90% at C1) and 0.32, respectively.

The electrophilic aromatic addition arises with the reactive  $\alpha$ -oxygen radical (O1) of the  $[\text{OFe}^{\text{III}}\text{O}]^+$  center attacking a carbon atom of the benzene ring, see TS\_4 in the below scheme. Like in the case of the high-valency monooxo-iron cation in cytochrome P450 (de Visser and Shaik, 2003), in an activated  $\text{Fe}^{\text{IV}}=\text{O}$  core of tetrahydrobiopterin-dependant hydroxylases (Bassan *et al.*, 2003), and in the gas phase  $[\text{Fe}=\text{O}]^+$  cation (Yoshizawa *et al.*, 2000b), it leads via electrophilic substitution to a  $\sigma$ -adduct Int\_2. The activation energy for O1 substitution is only 9.99 kcal/mol while the H1 removal requires higher energy (25.67 kcal/mol) to occur. This indicates that energetic profiles show that O1 prefers ring attack to H1 removal.



As a consequence, the most preferable mechanism for benzene activation is the electrophilic substitution. The product of this activation is the  $\sigma$  adduct Int\_2 in which the attacked  $sp^2$  carbon C1 is turned into the  $sp^3$  species. Due to the Mulliken spin density of benzene is  $0.42e^-$  for TS\_3 and  $0.29e^-$  for the  $\sigma$ -adduct and charge of benzene moiety is 0.38 for TS\_3 and 0.27 for the  $\sigma$ -adduct. So it is difficult to characterize the  $\sigma$  adduct as a radical or cation species. While the  $\sigma$ -adduct is found in both radical and cation in the P450 system (de Visser and Shaik, 2003).

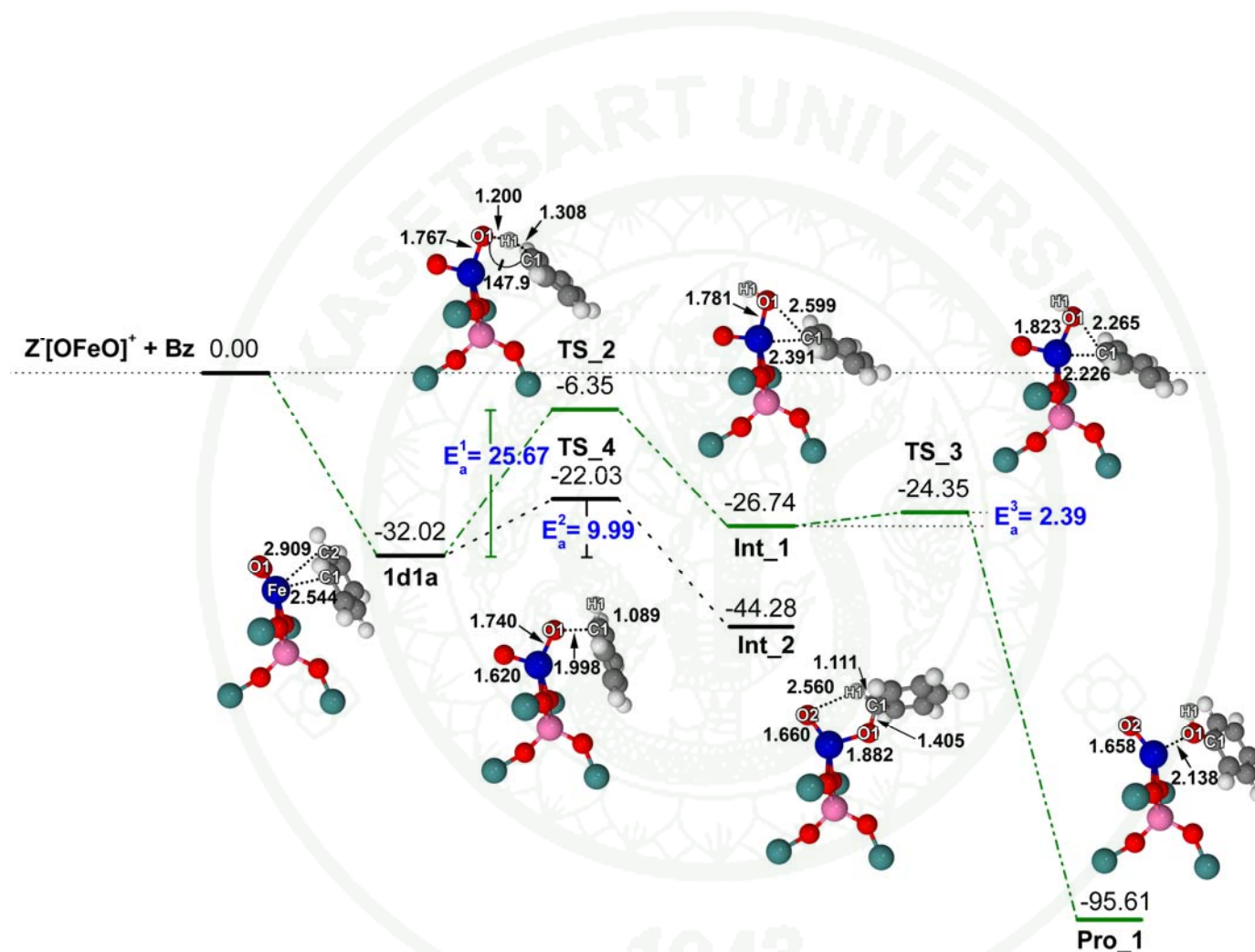
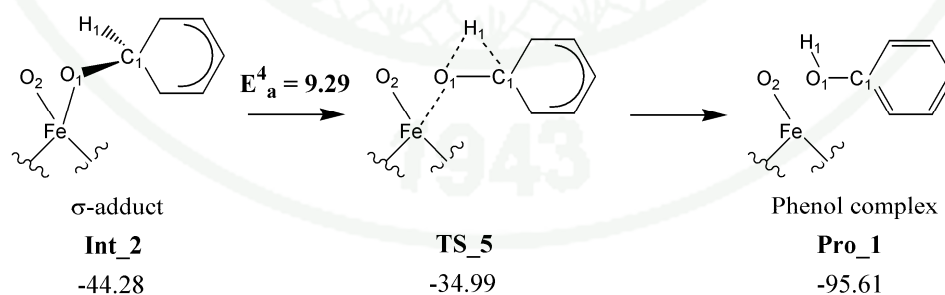


**Figure 11** Energy profiles of the **1d1a** activation via H-abstraction (—••) and electrophilic substitution (- - -). Energies are obtained from the single point calculation at UM06//ONIOM2(UM06:UFF) level. Optimized structures are taken from the ONIOM2(UM06:UFF) level. Energies, distances and angles are given in kcal/mol, angstroms and degree.

### 3.2 Rearrangement of the $\sigma$ -adduct

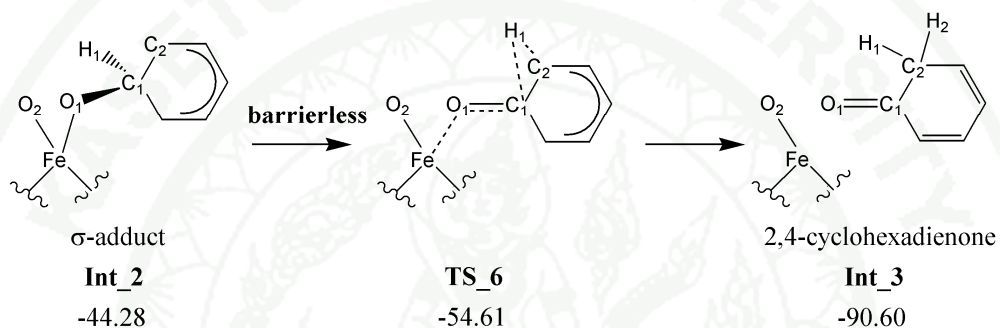
Next, the *ipso* hydrogen (H1) of the  $\sigma$ -adduct (Int\_2) can then rearrange to form the more stable resonant complexes via four channels: (I) 1,2-H transfer to form phenol, (II) NIH shift to form a keto intermediate, (III) proton-shuttle forming hydroxo-phenoxo ligands on Fe atom, and (IV) ring closure yielding benzene oxide. Theoretically studies showed that ring closure needs 15.2 kcal/mol for in an activated  $\text{Fe}^{\text{IV}}=\text{O}$  core of tetrahydrobiopterin-dependant hydroxylases (Bassan *et al.*, 2003) and 1.4 kcal/mol for cytochrome P450 enzyme (de Visser and Shaik, 2003). So benzene oxide is possibly produced from the  $\sigma$ -adduct but it is a dead-end product that cannot convert to phenol and ketone (Bassan *et al.*, 2003; de Visser and Shaik, 2003). Therefore, the  $\sigma$ -adduct transformation into benzene oxide is not investigated in this work. The energetic profiles and optimized structures for the  $\sigma$ -adduct transformation are shown in Figure 12.

In channel I, the 1,2-H shift arises via TS\_5 in which H1 at the *ipso* position (C1) leaving to the *meso* O1 forming the phenol product (Pro\_1). This stage occurs via the three-centered transition state which the H-C1-O1 plane is perpendicular to the benzene ring as shown in the following. This requires an energy of about 9 kcal/mol in shifting H1 from C1 to  $\text{O}_\alpha 1$ .

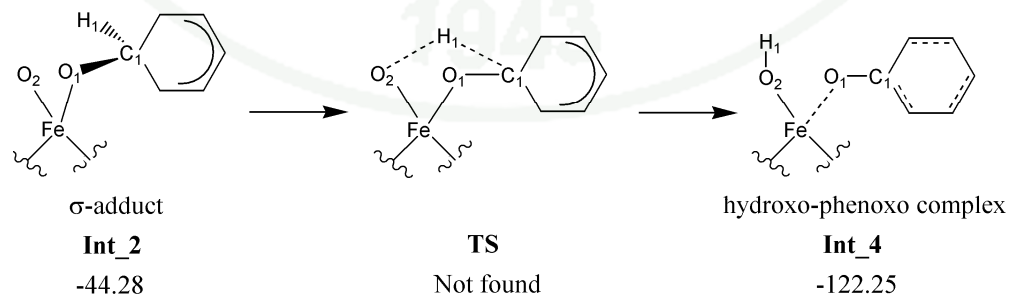


Channel II, NIH shift, is the 1,2-H shift along the benzene ring (see the following). The *ipso* H1 moves to the adjacent carbon C2 yielding the keto intermediate, 2,4-cyclohexadienone, Int\_3. This state is a barrier-free step. To verify this, the NIH shift activation energy of a gas phase  $\sigma$ -adduct cation radical was calculated. It is found that it needs energy only 2.0 kcal/mol. In the zeolitic system, Fe atom gains electron from the  $\sigma$ -adduct leading the more positive charge of the

benzene ring (charge = 0.76 and spin density = 0.13). Therefore, after the  $\sigma$ -adduct formation in Fe-ZSM-5, the reaction simultaneously shifts to 2,4-cyclohexadienone. Although TS\_6 of channel II is the three-center transition state which is similar to TS\_5 of channel I, but the energy barrier is completely different. This is due to TS\_6 as a reactant-like transition state and the adjacent carbons (C2 and C3) having some spin density ( $\sim 0.07e^-$ ), so, the NIH shift can occur rapidly.



The proton-shuttle channel III poses 1,4-H shift from C1 to the radical O2 ligand as the following shows. However, at ONIOM2(UM06:UFF) approach, the optimized structure of this transition state has not been found yet. Due to the reaction takes place via the five-centered transition state, which is less constrain than TS\_5, and the O2 ligand is more reactive than C2 and C3, therefore, the estimated activation energy of the 1,4-H shift of this channel should be barrierless. Hence, the proton-shuttle of the  $\sigma$  adduct is more favorable than the 1,2-H transfer step in channel I. This mechanism produces a very stable hydroxo-phenoxo complex Int\_4 which is also generated from 2,4-cyclohexadienone Int\_3 via channel II that will be addressed next.



As a conclusion, after the  $\sigma$ -adduct formation (Int\_2), the reaction prefers to produce both the 2,4-cyclohexadienone (Int\_3) and the hydroxo-phenoxo intermediate (Int\_4).

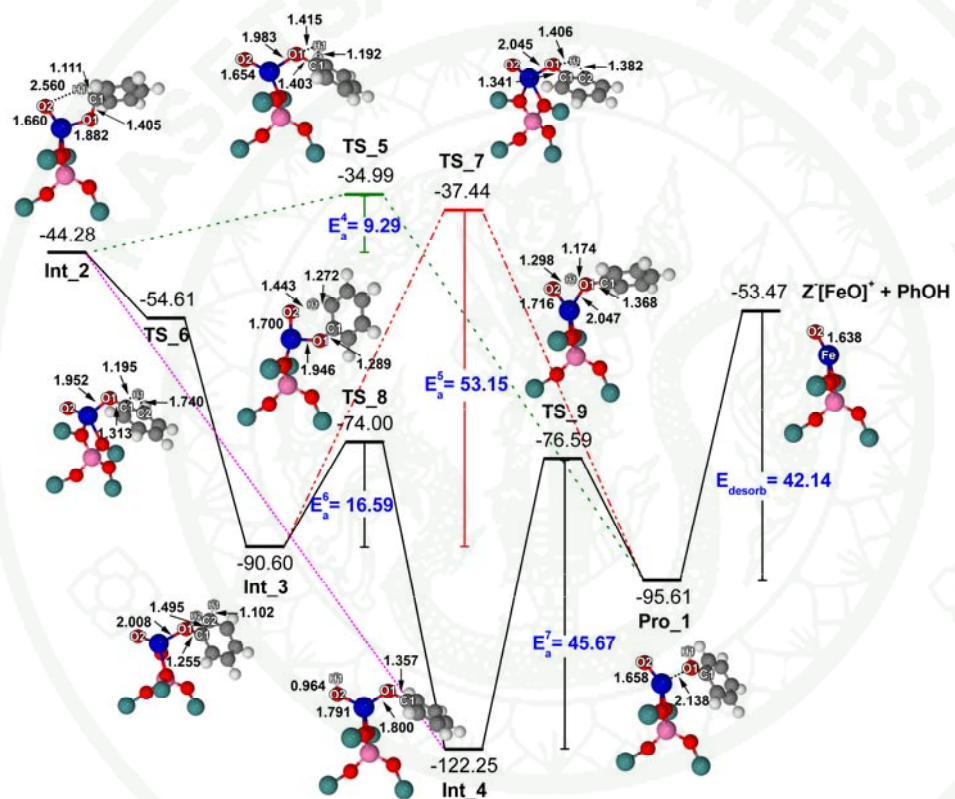
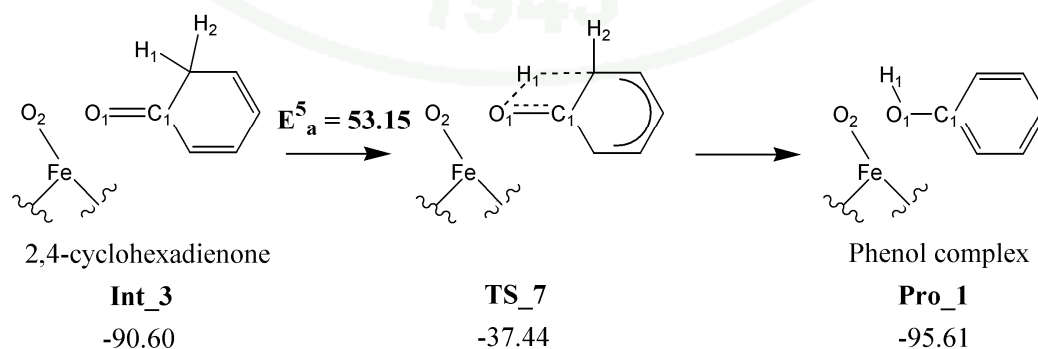


**Figure 12** Energy profiles: a) 1,2-H transfer (---), NIH shift (—) and proton-shuttle (····) of the  $\sigma$ -adduct (Int\_2) and b) keto-enol tautomerization (— · ·) and proton shuttle (—) of 2,4-cyclohexadienone (Int\_3). Energies are obtained from the single point calculation at UM06//ONIAM2(UM06:UFF) level and given in kcal/mol. Optimized structures with selected parameters are taken from the ONIAM2(UM06:UFF) level. Distances and angles are given in angstroms and degree.

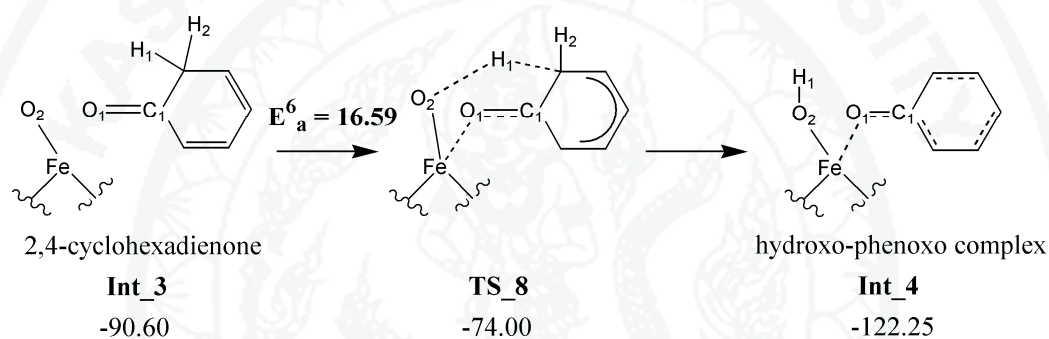
### 3.3 Transformation of 2,4-cyclohexadienone

2,4-cyclohexadienone (Int\_3) is strongly adsorbed on the Fe site leading a large adsorption energy of -90.60 kcal/mol. In order to release the ketone from the FeO center, a huge energy of 54.40 kcal/mol is needed for tunneling through the barrier. Therefore, the ketone desorption channel is not preferable. The ketone can occur the subsequent intramolecular hydrogen transfer to *meta*- and *para*-carbons. However, theoretical study of the tautomerization of the gas phase 2,4-cyclohexadienone found that 1,2- and 1,3-H shifts require high energy of 42.7 and 103.2 kcal/mol, respectively (Gomez *et al.*, 2006). Consequently, this intramolecular H-transfer is not considered in the present work as well.

Moreover, Int\_3 can occur both the keto-enol tautomerization and the proton shuttle to the O2 ligand. The keto-enol transformation obtains an adsorbed phenol (Pro\_1) as a product via TS\_7 in which H1 poses the 1,3-H shift to O1, see the below scheme. The activation energy of this stage is calculated to be 53.15 kcal/mol which is similar to that in the gas phase of 53.3 kcal/mol (Gomez *et al.*, 2006). This indicates that the  $\alpha$ -site does not affect for keto-enol tautomerization in the zeolitic system. Compare to the phenol formation via the three-centered transition state of TS\_5, the four-centered TS\_7 needs larger energy because O1 is out-of-plane of the benzene ring. At this point, the phenol production cannot be reached via the keto-enol tautomerism.



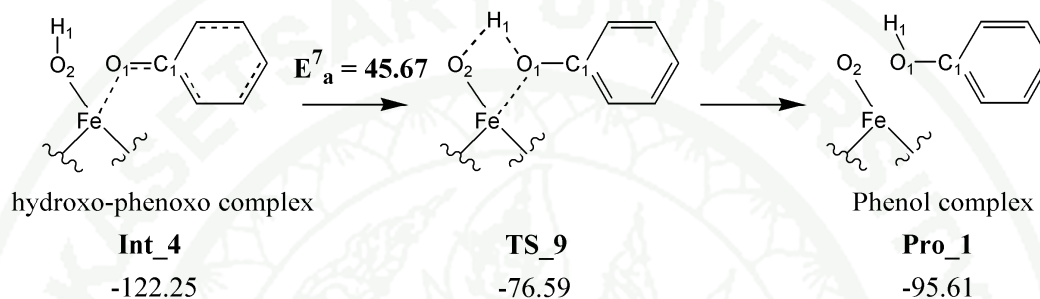
The most possible pathway for the 2,4-cyclohexadienone rearrangement is the proton shuttle mechanism in which H1 is leaving from C2 site to the radical O2 ligand via 1,5-H shift of TS\_8 as shown below. The energy of 16.59 kcal/mol is required in order to pass the barrier of the six-centered transition state TS\_8. Therefore, this channel is more favorable than the keto-enol tautomerism. The corresponding product of this stage is the hydroxo-phenoxo complex (Int\_4) which can also be formed via the proton shuttle of channel III which is addressed earlier.



### 3.4 Formation and desorption of phenol

Aside from the phenol production via the 1,2-hydride shift of the  $\sigma$ -adduct and the keto-enol tautomerization of 2,4-cyclohexadienone (Int\_3), phenol can also be obtained from the proton transfer (TS\_9) of the hydroxo-phenoxo complex (Int\_4). The following mechanism is shown in 2-dimension below. The hydroxo H1 of Int\_4 moves to the phenoxo O1 forming the adsorbed phenol (Pro\_1) as the final product. Because Int\_4 is very stable (-122.25 kcal/mol) and the hydroxo group strongly coordinates to Fe center, hence, it is difficult to pass TS\_9 to generate the phenol. The activation energy for H-transfer to form Pro\_1 is 45.67 kcal/mol. The phenol is adsorbed on Fe site via lone-pair electron of O1 of phenol which is weaker interaction than the coordination of the hydroxyl group on Fe site leading the product phenol is less stable than Int\_4. Although, the phenol complex Pro\_1 is very stable (-95.61 kcal/mol) but its structure is similar to an isolated phenol. Pro\_1 can be desorbed to obtain the isolated phenol and  $Z[\text{FeO}]^+$ . The spin density of Fe  $\rho(\text{Fe})$  is  $3.95e^-$  for  $Z[\text{FeO}]^+$  while O2 is still a radical which  $\rho(\text{O2}) = 0.95e^-$  for  $Z[\text{FeO}]^+$ .

These mean that, after benzene hydroxylation,  $\text{Fe}^{\text{III}}$  ion is reduced to be  $\text{Fe}^{\text{II}}$  ion and  $\text{O}_2$  can cause further reactions. The Fe-O<sub>2</sub> bond and the spin density of  $Z^+[\text{FeO}]^+$  are not much different from those of the phenol complex, Pro\_1. The desorption energy of phenol from Fe-ZSM-5 is 42.14 kcal/mol for  $Z^+[\text{FeO}]^+$  (see Figure 12).



### 3.5 The most possible reaction mechanism and rate-determining step

The direct benzene-to-phenol conversion on Fe-ZSM-5 has been studied via M06 functional. All structures were optimized at ONIOM2(UM06:UFF) approach and then the single point calculation at UM06 were performed to obtain the reliable energies. From the results, It can be concluded that the adsorbed benzene is activated by  $\alpha$ -oxygen of the active Fe center via electrophilic substitution yielding the  $\sigma$ -adduct. The activation energy is calculated to be 9.99 kcal/mol. The most easily accessible pathway of the  $\sigma$ -adduct to phenol conversion is the subsequent production of the hydroxo-phenoxo intermediate obtained by either via the proton shuttle of the  $\sigma$ -adduct or via the 1,5-H shift of 2,4-cyclohexadienone which is produced from 1,2-H shift of the  $\sigma$ -adduct. Then the hydroxo-phenoxo intermediate proceeds the migration of the hydroxo hydrogen atom to the phenoxo oxygen atom for phenol production. When considering a total reaction including the phenol desorption, it is found that the migration of H of the hydroxo-phenoxo intermediate is a rate-limiting step. The activation energy of this step is 45.67 kcal/mol which slightly higher than the phenol desorption energy of 42.14 kcal/mol.

## **Au(I) cation and Au(CN)<sub>2</sub><sup>-</sup> anion in liquid nitromethane: quantum chemical calculations and molecular dynamics simulations**

### 1. Quantum Chemical Calculations

#### 1.1 The Au<sup>+</sup>-NM interaction

Despite a long history of applying quantum chemical theory and calculations to gold-ligand systems some aspects of the energetics and the bond-directionality of transition metal cation-ligand interactions remain an interesting problem.

In some respect, Au(I)-ligand systems are simpler than most other transition metal-ligand systems because Au(I) has a completely filled d<sup>10</sup>-shell, like Cu(I) and Ag(I). Even on the Hartree-Fock level, however, orbital effects are encountered. If NM ligands are added subsequently into the solvation shell of Au(I), the second NM molecule is about as strongly (or even slightly stronger, depending on the method of calculation) bound than the first one. Such a behavior is not found for singly charged alkaline ions where saturation effects start right away and in fact the decrease in the incremental binding energies is largest when going from one to two ligands ( $\Delta E_1^{\text{inc}}$ ).

$$\Delta E_n^{\text{inc}} = E_n^{\text{inc}} - E_{n-1}^{\text{inc}} \quad (11)$$

$$E_n^{\text{inc}} = E(\text{Au}(\text{NM})_n^+) - E(\text{Au}(\text{NM})_{n-1}^+) - E(\text{NM}) \quad (12)$$

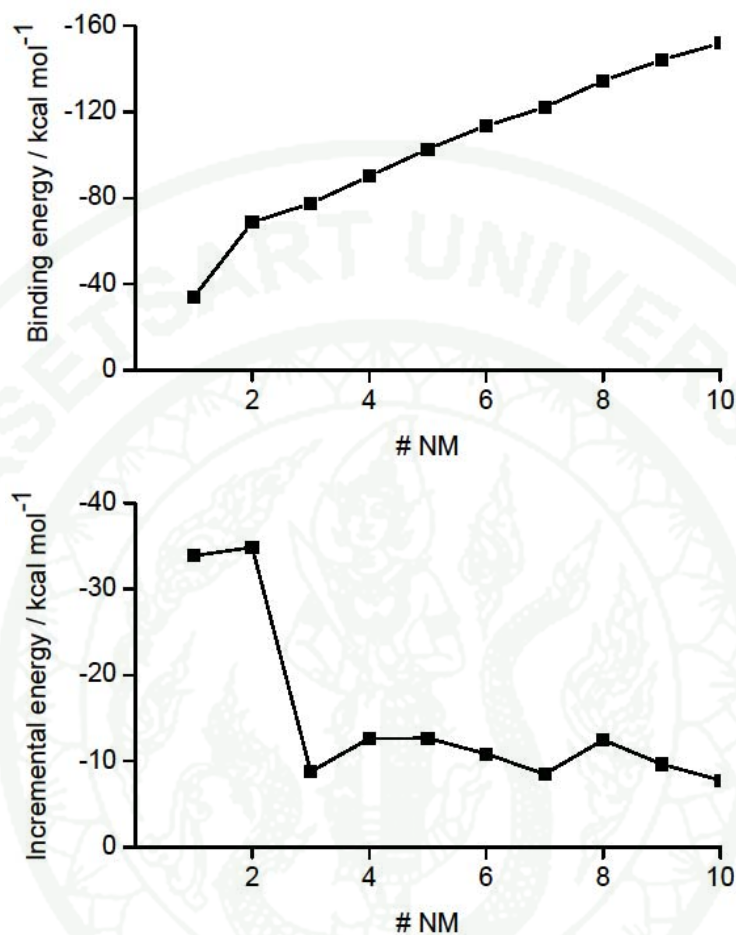


**Figure 13** Upper panel: Total ligand-cation binding energies of the most stable structure defined as  $E = E(\text{Au}(\text{NM})_n^+) - E(\text{Au}^+) - n E(\text{NM})$  in the  $\text{Au}(\text{NM})_n^+$  clusters with  $n = 1$  to 10. Lower panel: Incremental energy for the same clusters, as defined as equation (11).

In other words, for 'purely electrostatic' systems like alkali cations the binding energy per ligand in the 1:1 complex is always more than the one in 1:2 complexes while for Au(I) the opposite is found, as Figure 13 shows. A natural bond orbital (NBO) analysis (Carpenter and Weinhold, 1988) shows that no chemical bond is formed between Au and the coordinating oxygen atom of NM. The charge transfer from one NM molecule to Au is  $0.04 e$  for  $\text{AuNM}^+$  and  $0.08 e$  for  $\text{AuNM}_2^+$ . The Au  $6s$  population in  $\text{AuNM}_2^+$  is  $0.35 e$  while the  $5d$  population decreases to  $9.81 e$  as

shown in Table 1. A similar small overall charge transfer with a large increase in density of the highest  $s$  AO has been observed for Cu(I)/H<sub>2</sub>O long ago by Rosi and Bauschlicher. In two publications on this subject (Rosi and Bauschlicher, 1989; Rosi and Bauschlicher, 1990), they showed (their tables III and I, respectively) the increase in  $4s$  density in Cu(H<sub>2</sub>O)<sub>2</sub><sup>+</sup>. These authors already give the probably correct reason for the nonadditive behavior. They stated that even without forming a bond, the mixing of  $s^1-d^9$  into the wavefunction reduces the Cu(I)-O repulsion, thus allowing the ligand to approach closer. In the linear O-Cu(I)-O system the cost of the  $s$ - $d$  mixing is shared between two ligands, offsetting the usual saturation effects. The same argument can be applied to Au(I). It is known (Pyykko, 2004b; Schmidbaur *et al.*, 2005) that, due to relativistic effects, the  $6s$ - $5d$  splitting in Au is much smaller than in Ag or Cu (in fact, the color of gold results from this). These effects cause a lowering of the  $6s$  and an increase of the  $5d$  energy, thus facilitating the  $s$ - $d$  mixing. The interaction of Au(I) with one and two water molecules has also recently been investigated by Lee and coworkers (Lee *et al.*, 2005). Their interpretation uses the same arguments but is more involved.

**Table 1** Atomic partial charge (NPA) and electronic configurations (NEC) of the atoms in NM, AuNM<sup>+</sup> and AuNM<sub>2</sub><sup>+</sup>. See text for details.

	NM					AuNM <sup>+</sup>					AuNM <sub>2</sub> <sup>+</sup>				
	NPA	NEC				NPA	NEC				NPA	NEC			
<b>Au</b>	1.00	6s	0.00	5d	10.00	0.96	6s	0.08	5d	9.96	0.84	6s	0.4	5d	9.81
<b>N</b>	0.57	2s	1.15	2p	3.25	0.61	2s	1.16	2p	3.20	0.61	2s	1.2	2p	3.20
<b>C</b>	-0.38	2s	1.12	2p	3.25	-0.37	2s	1.13	2p	3.23	-0.37	2s	1.1	2p	3.23
<b>O*</b>	-0.48	2s	1.79	2p	4.67	-0.65	2s	1.77	2p	4.86	-0.63	2s	1.8	2p	4.52
<b>O</b>	-0.40	2s	1.75	2p	4.64	-0.30	2s	1.75	2p	4.54	-0.28	2s	1.8	2p	4.85
<b>H</b>	0.23	1s	0.77			0.25	1s	0.75			0.25	1s	0.8		
<b>H</b>	0.23	1s	0.77			0.25	1s	0.75			0.25	1s	0.8		
<b>H</b>	0.23	1s	0.77			0.25	1s	0.75			0.25	1s	0.8		

In some sense, therefore, the non-additivity discussed above is a relativistic effect. Non-relativistic quantum chemical calculations on Au are not recommended. Relativistic calculations on Au are not per se a problem, since the main effects like mass-velocity and Darwin are already well dealt with by using an atom-derived relativistic effective core potential like (Hay and Wadt, 1985) and only for very accurate results high-level calculations that solve the full-electron Dirac equation are necessary.

This situation is further illustrated by comparing the fully geometry-optimized  $\text{AuNM}_3^+$  complex with one in which  $C_{3h}$  symmetry is enforced. In the former, one O-Au-O angle is nearly linear and the Au-O distance to the third oxygen is considerably longer (Figure 14). There linear O-Au-O arrangement goes together with a  $6s$  population of  $0.30 e$  compared to  $0.13 e$  in the  $C_{3h}$  complex (Table 2).

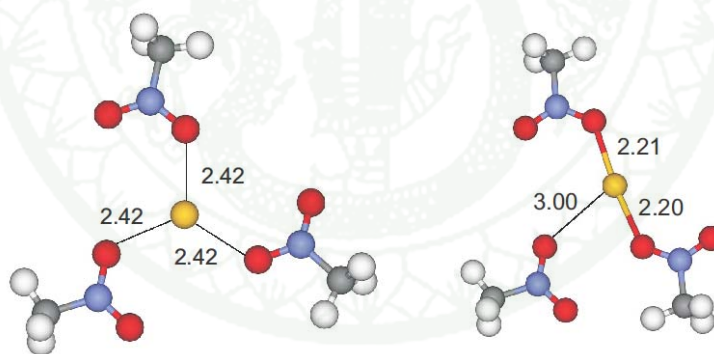


**Figure 14** Geometries of  $C_{3h}$ - symmetric (left) and fully geometry-optimized (right)  $\text{AuNM}_3^+$ , together with Au-O distances (Å).

**Table 2** Atomic partial charges (NPA) and 6s and 5d populations (NEC) of Au in  $\text{AuNM}_3^+$ : geometry-optimized (left) and forced  $C_{3h}$ -symmetric structure (right).

$\text{AuNM}_3^+$ (opt.geom.)					$\text{AuNM}_3^+$ ( $C_{3h}$ geom.)				
NPA	NEC				NPA	NEC			
0.86	6s	0.30	5d	9.83	0.91	6s	0.13	5d	9.94

In order to see if this highly nonadditive behavior for low coordination numbers has consequences for larger complexes, geometry optimizations on  $\text{AuNM}_n$  with  $1 \leq n \leq 10$  were performed. Their structures are shown in Figure 15. From the interaction energies (Figure 12, Upper panel), it can be seen that for  $n > 3$ , the energetics resemble a low charge-density cation like  $\text{K}^+$ . Despite of the large value of  $\Delta E_n^{\text{inc}}$  for  $n=1$ , NM molecules beyond  $n=2$  are also bound in the first shell because they increase the overall binding energy. This justifies the construction of a pair potential like normally used for large, singly charged cations without problems. Its construction is outlined in section 2.1 of the ‘methods of calculations’ part. One might argue that it has to be differentiated nevertheless between the first two NM molecules and the rest in the sense that larger clusters  $\text{AuNM}_n^+$  consist of  $\text{AuNM}_2^+$  solvated by  $n-2$  more loosely bound NM molecules. However, one sees that in  $\text{AuNM}_3^+$  the energy of the trigonal planar geometry (Figures 14 and 15) is only slightly higher than the T-shaped one and for  $n=4$  the tetrahedral arrangement is already 2 kcal/mol more stable than the square planar one. Therefore,  $\text{AuNM}_2^+$  should not be considered as an ‘inert core’, dynamical considerations notwithstanding. The  $\text{AuNM}_n^+$  clusters were all optimized without constraints. Up to  $n=8$  they are compact and even the  $\text{AuNM}_{10}^+$  cluster shows not two solvation shells but eight shorter (4.02 Å) and two longer (~5.11 Å) Au-O distances in a capped double prism typical of coordination number 10. Therefore, even without taking into account the pV term which in condensed phase systems makes ‘spongy’ structures less favourable, a high coordination number of Au(I) in NM can be expected. It should be mentioned that at least for the gas phase

this is different to the Au(I)/H<sub>2</sub>O system where calculations indicate that from the third water molecules onward, a second shell is formed (Reveles *et al.*, 2007), partially due to the larger water-water interaction. Finally it should be mentioned that a recent combined experimental and theoretical study (Iino *et al.*, 2007) on Cu/H<sub>2</sub>O and Ag/H<sub>2</sub>O hydration in the gas phase showed that the situation for Cu<sup>+</sup> is similar to the one encountered for Au<sup>+</sup>, in contrast to Ag<sup>+</sup> where the *d/s* gap is much larger.

It can conclude that the quantum chemical cluster calculations indicate that, despite the peculiarities of the Au<sup>+</sup>-NM interaction, MD simulations with suitably chosen pair-additive potentials are justified for the condensed phase.

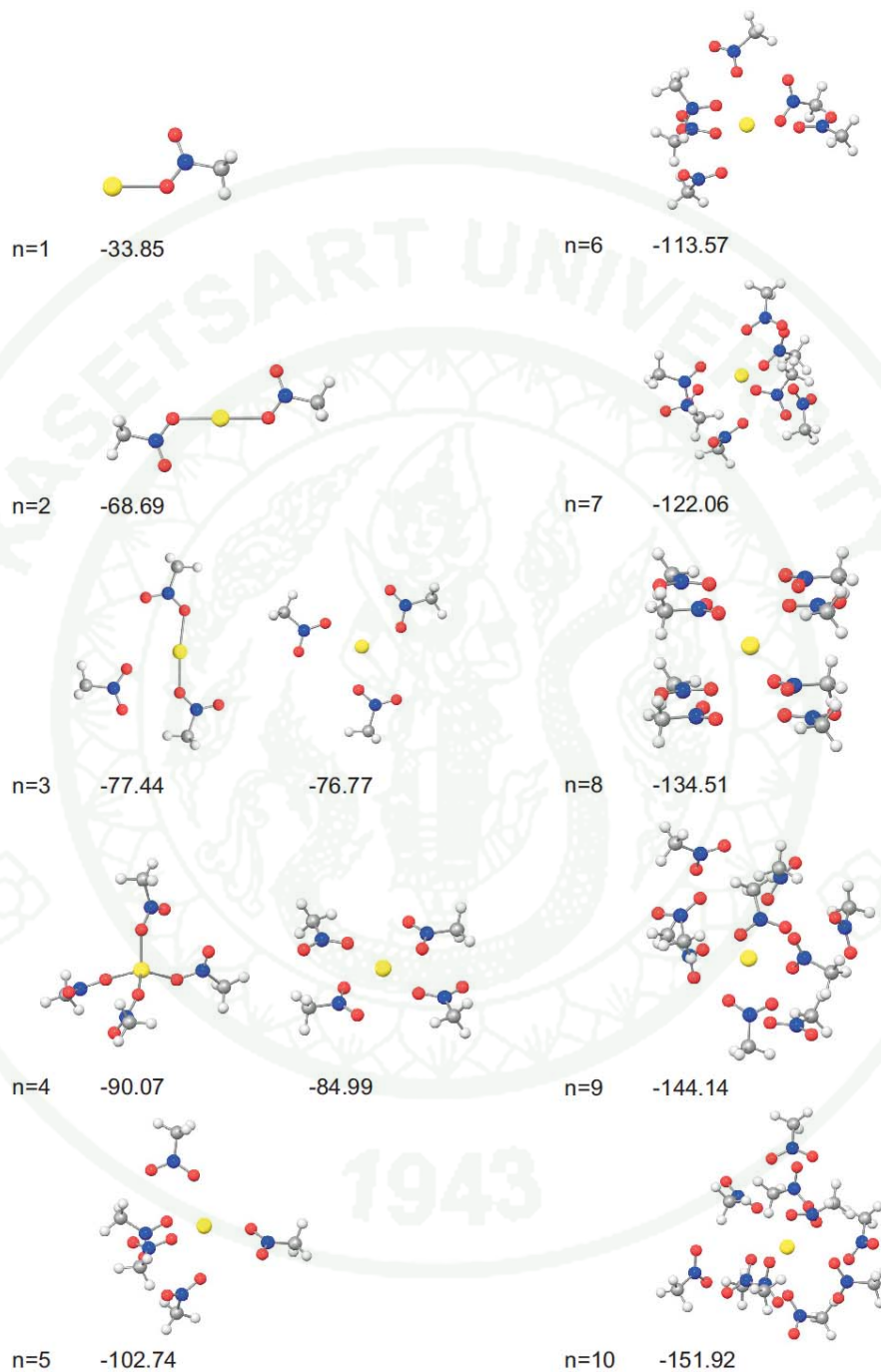


**Figure 15** Optimized geometries together with the total ligand-cation binding energies ( $E$ ) of  $\text{AuNM}_n$  with  $1 \leq n \leq 10$  calculated at HF level. Energies are given in kcal/mol.

## 1.2 Au(CN)<sub>2</sub><sup>-</sup>-NM interaction

### 1.2.1 Structure and formation energy of Au(CN)<sub>2</sub><sup>-</sup>

In order to form Au(CN)<sub>2</sub><sup>-</sup> anion, electrons in *sp* orbital of C atom of CN<sup>-</sup> group transfers to the unoccupied *6s* orbital of Au(I) yielding AuCN species. It is clearly seen that Au(I) gains 0.36 *e* from CN<sup>-</sup> group, see NPA in Table 3. Moreover, due to a strong ligand field of CN<sup>-</sup>, only one CN<sup>-</sup> group can cause the mixing of *6s-5d* orbital of Au(I) while it needs two nitromethane molecules to cause this hybrid orbital. The ion-ligand formation between Au(I) cation and the first CN<sup>-</sup> group is an exothermic reaction and releases energy of 180.62 kcal/mol. The calculated Au-C and C-N distances are 1.998 and 1.160 Å, respectively. Similarly, to form Au(CN)<sub>2</sub><sup>-</sup> anion, the *6s* orbital of Au(I) in AuCN obtains 0.31*e* from *sp* orbital of C atom of the second CN<sup>-</sup> ligand. This formation is a weaker interaction than the first one, its energy is calculated to be -94.2 kcal/mol. The mixing of *6s-5d-6p* orbital of Au(I) is observed in the Au(CN)<sub>2</sub><sup>-</sup> case. Au(CN)<sub>2</sub><sup>-</sup> is a linear molecule with D<sub>∞h</sub> symmetry. Its structure can be compared to the S-Au(I)-S complexes (Bryce *et al.*, 2003). The calculated Au-C and C-N distances are 2.050 and 1.166 Å, respectively. This agrees well with X-ray diffraction data for the crystals Nd[Au(CN)<sub>2</sub>]<sub>3</sub>·3H<sub>2</sub>O and Am[Au(CN)<sub>2</sub>]<sub>3</sub>·3H<sub>2</sub>O in which the Au-C distance is 1.984 and 2.064 Å, respective for Nd[Au(CN)<sub>2</sub>]<sub>3</sub>·3H<sub>2</sub>O and Am[Au(CN)<sub>2</sub>]<sub>3</sub>·3H<sub>2</sub>O while the C-N distance is 1.141 and 1.075 Å for Nd[Au(CN)<sub>2</sub>]<sub>3</sub>·3H<sub>2</sub>O and Am[Au(CN)<sub>2</sub>]<sub>3</sub>·3H<sub>2</sub>O, respectively (Assefa *et al.*, 2007).

**Table 3** Atomic partial charge (NPA) and electronic configurations (NEC) of the atoms in Au(I), CN<sup>-</sup>, AuCN and Au(CN)<sub>2</sub><sup>-</sup>. See text for details.

	Au(I)							CN <sup>-</sup>						
	NPA	NEC						NPA	NEC					
<b>Au</b>	1.00	6s	0.00	5d	10.0	6p	0.00	-	-					
C	-	-						-0.18	2s	1.56	2p	2.56	3s	0.04
N	-	-						-0.82	2s	1.62	2p	4.19	3s	0.01
	AuCN							Au(CN) <sub>2</sub> <sup>-</sup>						
	NPA	NEC						NPA	NEC					
<b>Au</b>	0.64	6s	0.51	5d	9.83	6p	0.02	0.33	6s	0.81	5d	9.73	6p	0.13
C	-0.20	2s	1.26	2p	2.91	3s	0.04	-0.10	2s	1.26	2p	2.77	3s	0.05
N	-0.44	2s	1.59	2p	3.84	3s	0.01	-0.57	2s	1.58	2p	3.98	3s	0.05

### 1.2.2 Electrostatic potential and electron densities

Au(CN)<sub>2</sub><sup>-</sup> consists formally of the singly positive Au(I) cation and the two singly negative cyanide ligands. The electron density ( $\rho$ ) difference between Au(CN)<sub>2</sub><sup>-</sup> constituents was calculated according to:

$$\Delta\rho = \rho_{\text{Total}} - \rho_{\text{Au}^+} - \rho_{(\text{CN})_{\text{Right}}^-} - \rho_{(\text{CN})_{\text{Left}}^-} \quad (13)$$

at the optimized structure of Au(CN)<sub>2</sub><sup>-</sup>. It reveals that the region around Au(I) gains electron density (Figure 16) from the CN<sup>-</sup> groups. This increase of electron density takes place in a ring-shaped region perpendicular to the axis of the anion.

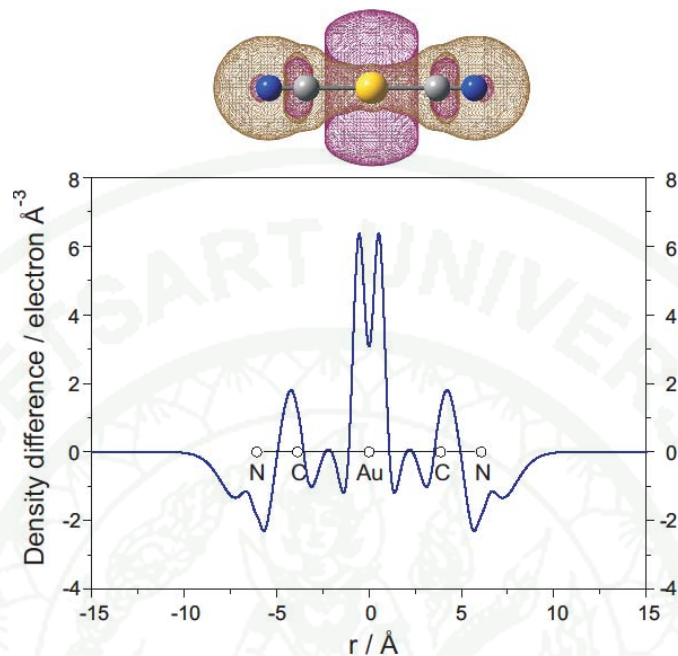


**Figure 16** Electron density difference between  $\text{Au}(\text{CN})_2^-$  complex and its constituents,  $\text{Au}(\text{I})$  and the  $\text{CN}^-$ . Isosurface plot (upper part) and integral of  $\Delta\rho(x,y,z)$  over  $y$  and  $z$  (lower part). The excess density (purple color, at  $\Delta\rho = 0.4 \times 10^{-3} e/\text{\AA}^3$ ) is located around  $\text{Au}(\text{I})$  while the  $\text{CN}^-$  groups lose some electron density. (brown color, isosurface plotted at  $\Delta\rho = -0.4 \times 10^{-3} e/\text{\AA}^3$ ).

### 1.2.3 Geometries and binding energies of $\text{Au}(\text{CN})_2^-/\text{NM}_n$ ( $n = 1:10$ ) complexes

Unlike it is the case for the free  $\text{Au}(\text{I})$  ion, the  $6s$  orbital in  $\text{Au}(\text{CN})_2^-$  is nearly fully occupied (Table 3). Therefore, it does not change its hybridization when interacting NM ligands. As a result, the binding energy per ligand decreases monotonically with the number ( $n$ ) of ligands (Figure 17) when the most stable structure for each  $n$  is considered. The optimized structures of  $\text{Au}(\text{CN})_2^-/\text{NM}_n$  with  $n = 1$  to 10 are shown in Figure 18. When a NM molecule is added into the solvation shell of  $\text{Au}(\text{CN})_2^-$ , it is found that the first NM prefers to be bound to  $\text{Au}(\text{CN})_2^-$  via end-on direction to form a linear  $\text{Au}(\text{CN})_2^-/\text{NM}$  complex. The binding

energy of this end-on structure is -13.43 kcal/mol and it is more stable ( $\sim 5$  kcal/mol) than the side-on structure with a T-shaped  $\text{Au}(\text{CN})_2^-$ -NM complex. This is due to the fact that the N atom of  $\text{Au}(\text{CN})_2^-$  is more negative than Au(I) (see Figure 2b).  $\text{Au}(\text{CN})_2^-$ - $\text{NM}_2$  is a linear complex but the NM molecules are loosely bound to the anion as mention above. This structure is more stable ( $\sim 3.7$  kcal/mol) than the one that two NM molecules are bound to the same N atom and hydrogen-bonded to each other. From  $n=2$  onward, in the larger complexes the incoming NM molecules prefer to be bound on each N atom of the anion and form the hydrogen-bond to each other. But, for  $n=7$ , the energy of this structure and the energy of the full ring structure is similar. In even larger complexes, the optimized geometries show that the additional NM molecules form as a half-ring structure. Moreover, the  $\text{Au}(\text{CN})_2^-$ - $\text{NM}_9$  complex prefers to be formed like a half-sphere as well. However, for  $n=10$ , a second NM shell starts to form. The incremental energy of  $n=8-10$  is greater than that of  $n=7$  due to the strong interaction between NM molecules. This behavior is often found for solutes where the interaction energy with solvent molecules similar to the solvent-solvent energy and reflects the competition between surface and interior states.

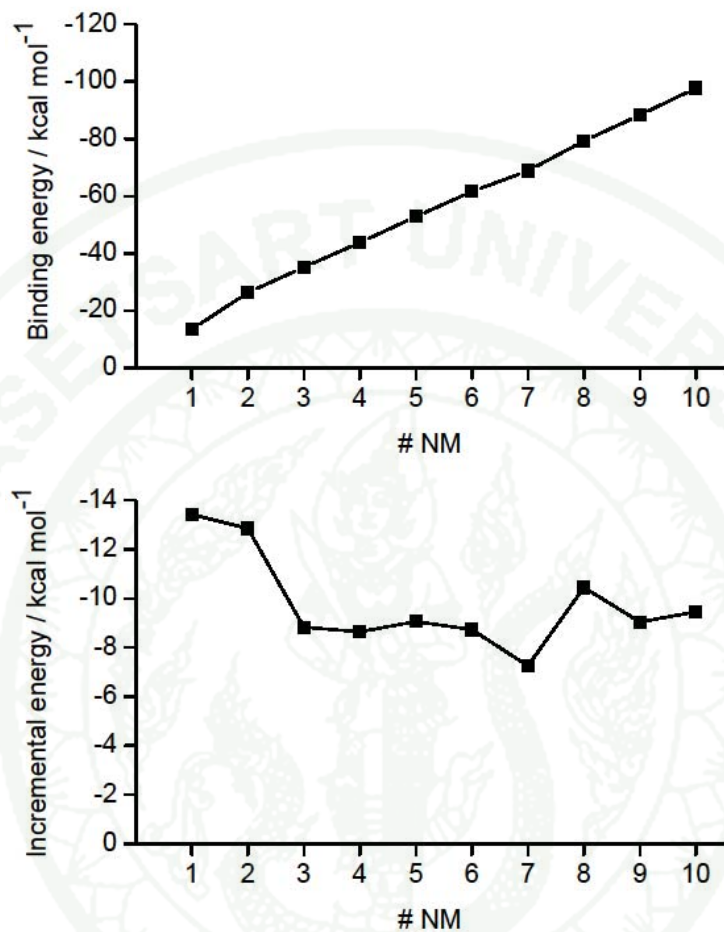


**Figure 17** (Upper) Total ligand-cation binding energies of the most stable structure defined as  $E = E(\text{Au}(\text{CN})_2^- \cdot \text{NM}_n) - E(\text{Au}(\text{CN})_2^-) - n E(\text{NM})$  in the  $\text{Au}(\text{CN})_2^- \cdot \text{NM}_n$  clusters with  $1 \leq n \leq 10$ . (Lower) Incremental energy defined as similar as equation (11).

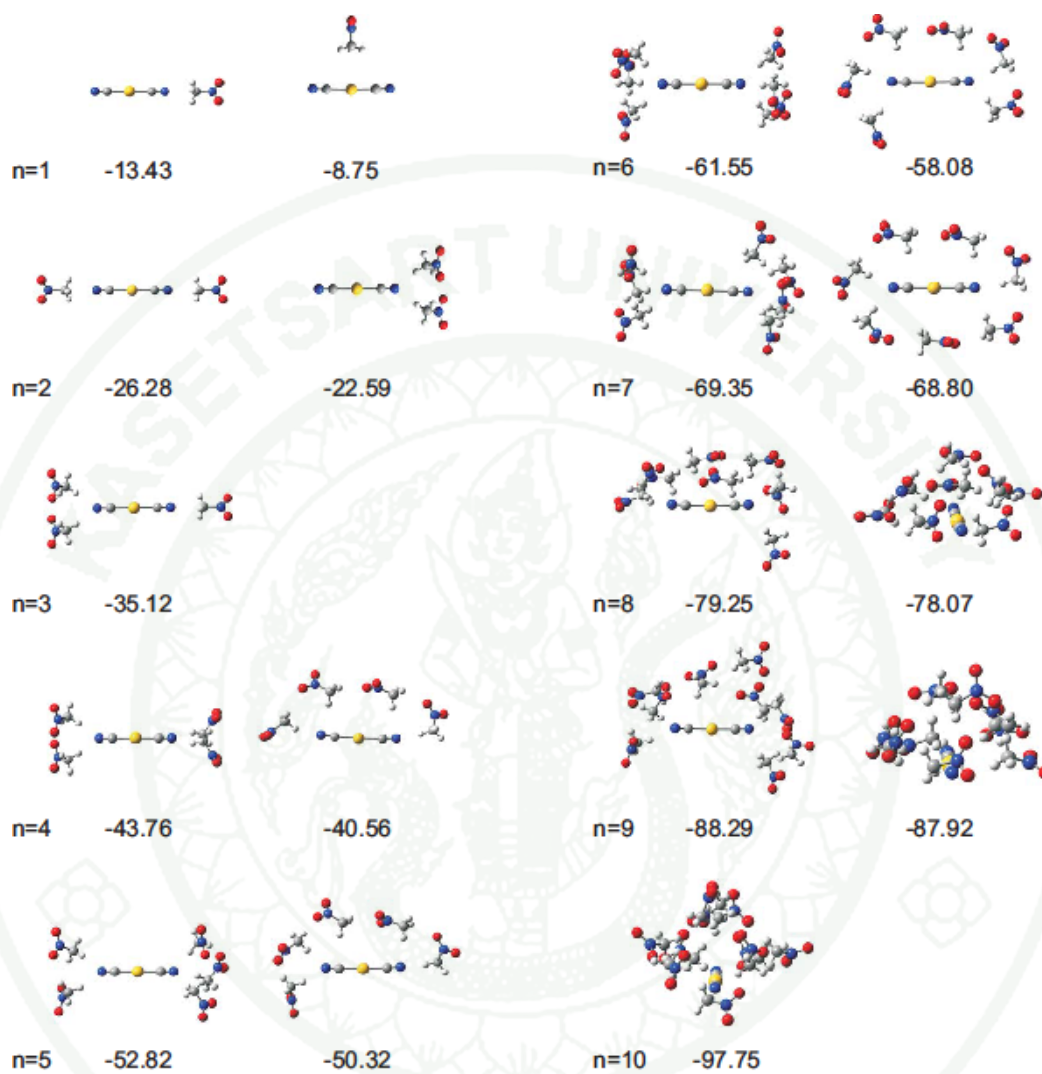


**Figure 18** Optimized geometries and binding energies of the stable conformations of  $\text{Au}(\text{CN})_2^- \cdot \text{NM}_n$  with  $1 \leq n \leq 10$  calculated at the HF level. Energies are given in kcal/mol.

## 2. Potential Energy Surface

### 2.1 Au<sup>+</sup>-NM Potential Energy Surface

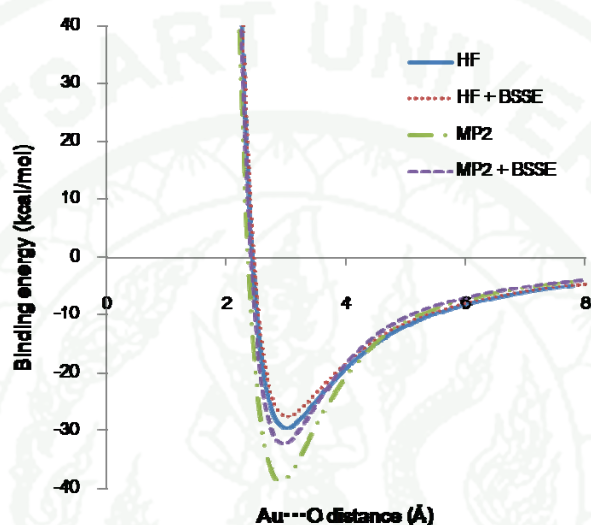


**Figure 19** Potential energy surface of Au<sup>+</sup>-NM along direction 1 as shown in Figure 3.

As mentioned in section 2.1 of the ‘method of calculations’ part the Hartree-Fock (HF) and MP2 levels with and without correction of basis set superposition error (BSSE) were employed to construct the Au<sup>+</sup>-NM potential function. Figure 19 shows the minimum PES calculated by various methods. Primarily because of the use of an ECP for the Au core electrons, the BSSE (basis set superposition error) of the binding energy at the HF level is small. For calculations at the MP2 level it was found that after correcting for the BSSE, (which is larger than for HF), both HF and MP2 binding energies are very similar, which is typical for systems dominated by electrostatics. Therefore, the HF level is suitable for constructing all PESs in this work. By finding the best parameters A to D via a least-square procedure in the analytical energy expression:

$$V_{fit}^{CH_3NO_2-Au^+} = \sum_{k \in NM} q_k / r_k + A_k / r_k^8 + B_k / r_k^6 + C \exp(-Dr_k) \quad (14)$$

the Au<sup>+</sup>-NM intermolecular potential function was derived. The first term is the Columbic energy which the Coulomb constant ( $4\pi\epsilon_0$ ) is 1. The powers of r of -8 and -6 in equation (14) do not have special physical significance but they gave a slightly better fitting than other combinations. These two terms in take care for the steep short-range parts while the exponential term models the shallow potential at medium distances. The details of the fitting procedure are described in section 2.2 of the ‘method of calculations’ part. The numerical values of the parameters are given in Table 4.

**Table 4** Charges and fitted parameters (kcal/mol and Å<sup>-1</sup>) for the Au<sup>+</sup>-NM pair potential. See text for explanations.

	<b>q</b>	<b>A</b>	<b>B</b>	<b>C</b>	<b>D</b>
C	-0.305	8 905.8	-19 646.0	166 150.0	3.1885
H	0.146	650.5703	-149.5139	81.15	1.0576
N	0.821	0.0044	235.6198	2 500.2	1.8507
O	-0.477	11 814.0	-10 535.0	69 080.0	3.1399

1943

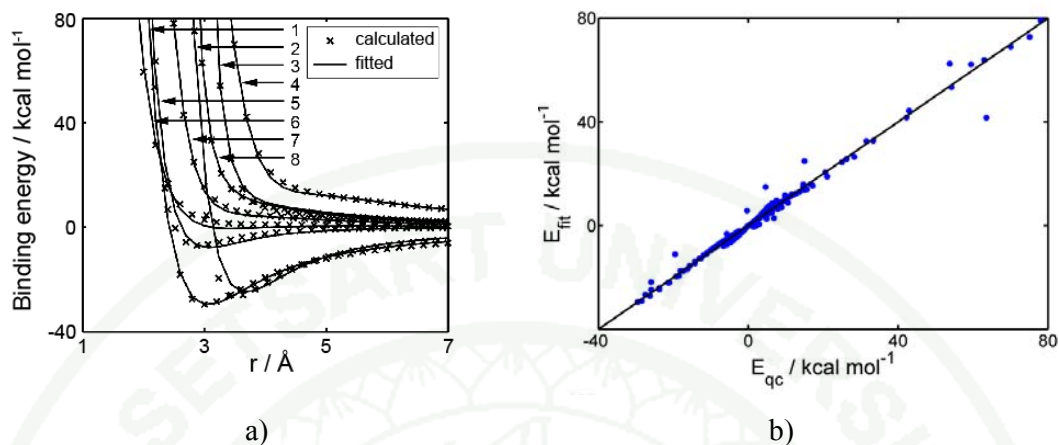


**Figure 20** a) Au-NM interaction: Quantum chemical (x) and fitted (solid lines) energies. The numbers 1-8 refer to Figure 3. b) Fitting accuracy of the Au<sup>+</sup>-NM potential energy function.

Figure 20a shows the correlation between the fitted energies and the ab-initio data. It can be seen that the overall fitting accuracy (Figure 20b) is very satisfactory. Figure 21 shows a contour plot of two cuts through the analytical Au-NM potential energy surface according to equation (14), in the symmetry plane of NM and 2 Å above it.

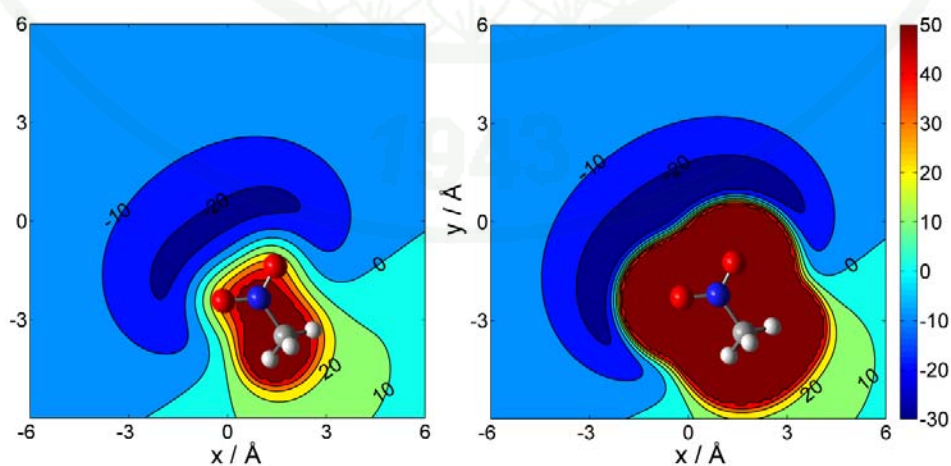


**Figure 21** Au-NM Potential energy according to equation (14) in the  $C_s$  plane of NM (right) and 2 Å above (left). Energies in kcal/mol and x/y coordinates in Å.

## 2.2 Au(CN)<sub>2</sub><sup>-</sup>-NM, K<sup>+</sup>-NM and K<sup>+</sup>-Au(CN)<sub>2</sub><sup>-</sup> Potential Energy Surface

The best functions for the Au(CN)<sub>2</sub><sup>-</sup>-NM, K<sup>+</sup>-NM and K<sup>+</sup>-Au(CN)<sub>2</sub><sup>-</sup> interactions are shown in equations (15-17). The atomic charges of Au(CN)<sub>2</sub><sup>-</sup>, K<sup>+</sup> and NM are given in Table 5.

$$V_{fit}^{NM-Au(CN)_2^-} = \sum_{j \in Au(CN)_2^-} \sum_{k \in NM} q_j q_k / r_{jk} + A_{jk} / r_k^3 + B_{jk} / r_k^4 + C_{jk} / r_k^5 \quad (15)$$

$$V_{fit}^{NM-K^+} = \sum_{k \in NM} q_k / r_k + A_k / r_k^4 + B_k / r_k^6 + C_k / r_k^8 \quad (16)$$

$$V_{fit}^{K^+-Au(CN)_2^-} = \sum_{k \in Au(CN)_2^-} q_k / r_k + A_k / r_k^3 + B_k / r_k^4 + C_k / r_k^5 \quad (17)$$

The values of the parameters **A** to **C** for each pair-potential are given in Tables 6-8. Again, the direct physical meaning of these functions is limited but they reproduce perfectly the attractive and repulsive energies obtained from quantum chemical calculations. The fitted energy together with the ab-initio data of each pair-potential is plotted as shown in Figures 22-24.

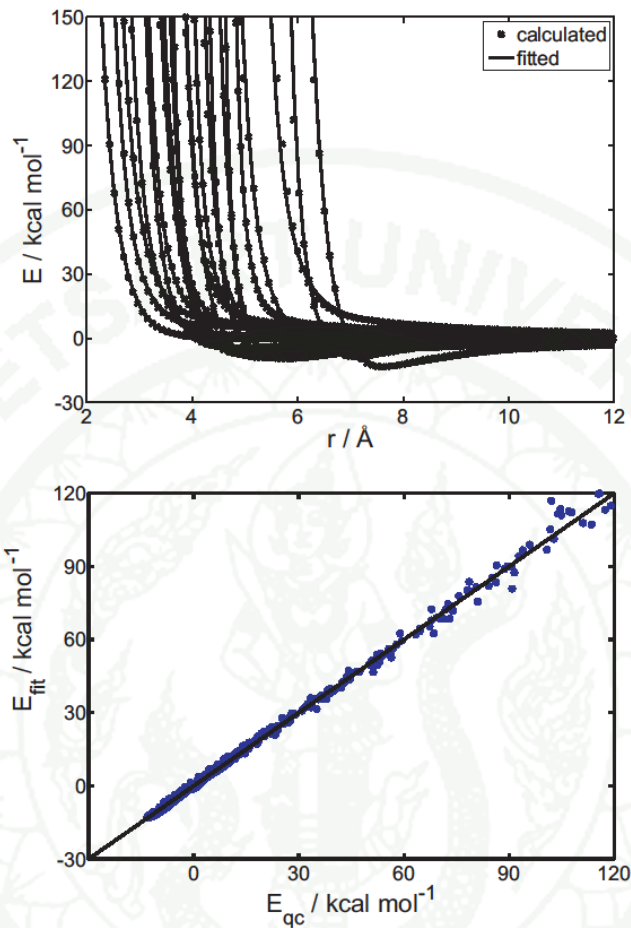
**Table 5** Atomic partial charges in Au(CN)<sub>2</sub><sup>-</sup>, K<sup>+</sup> and NM used in equations 15-17.

NM	$q_i$	K <sup>+</sup> & Au(CN) <sub>2</sub> <sup>-</sup>	$q_i$
C	-0.305	Au	0.411
H	0.146	C	-0.433
N	0.821	N	-0.272
O	-0.477	K	1.000

**Table 6** Values of the fitted parameters (kcal/mol) for the Au(CN)<sub>2</sub><sup>-</sup>-NM pair potential.

<b>j</b>	<b>k</b>	<b>A</b>	<b>B</b>	<b>C</b>
Au	C	576.3645	-5 411.1	10 557.0
Au	H	-163.8395	391.271	131.2832
Au	N	-1 331.2	1 890.3	0.0
Au	O	1 864.3	-6 534.9	8 405.5
C1	C	625.6538	-5 240.7	8 500.7
C1	H	233.4933	-176.6096	89.4191
C1	N	692.8688	317.4628	0.0
C1	O	-1 194.8	1 877.8	339.4626
N1	C	-1 142.0	2 439.6	104.5295
N1	H	-65.3314	168.5723	0.0
N1	N	546.0669	-4 127.1	5 480.0
N1	O	561.9225	-1 716.3	2 847.2

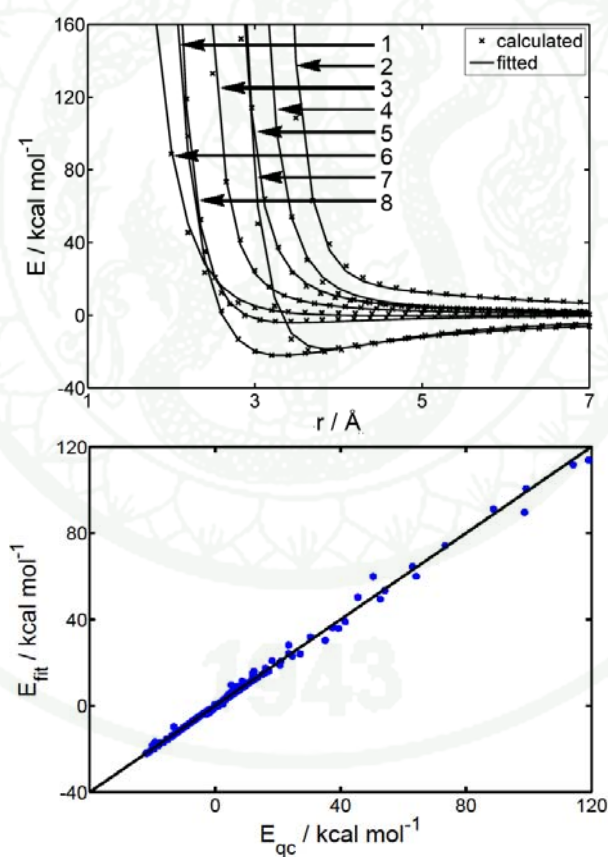
1943



**Figure 22** (Upper part)  $\text{Au}(\text{CN})_2^-$ -NM interaction: Quantum chemical (x) and fitted (solid lines) energies. (Lower part) Fitting accuracy of the  $\text{Au}(\text{CN})_2^-$ -NM potential energy function.

**Table 7** Fitted parameters (kcal/mol) for the  $K^+$ -NM pair potential.

	A	B	C
C	-120.691	-13 777.0	73 064.0
H	166.515	303.829	0.0
N	777.359	1 572.6	0.0
O	-1 185.5	6 681.1	0.0

**Figure 23** (Upper part)  $K^+$ -NM interaction: Quantum chemical (x) and fitted (solid lines) energies. The numbers 1-8 refer to Figure 3. (Lower part) Fitting accuracy of the  $K^+$ -NM potential energy function.

**Table 8** Values of the parameters of the  $\text{K}^+\text{-Au}(\text{CN})_2^-$  pair potential. Energies are given in kcal/mol.

	A	B	C
Au	-3 260.0	2 880.0	9 730.0
C1	5 150.0	-16 000.0	16 600.0
N1	-2 760.0	5 150.0	865.4599

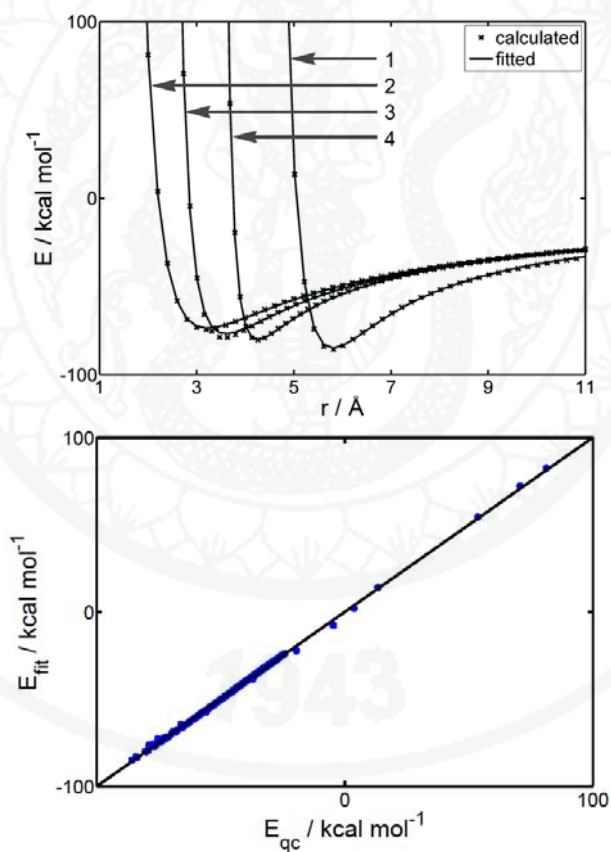


**Figure 24** (Right)  $\text{K}^+\text{-Au}(\text{CN})_2^-$  interaction: Quantum chemical (x) and fitted (solid lines) energies. (Left) Fitting accuracy of the  $\text{K}^+\text{-Au}(\text{CN})_2^-$  potential energy function.

### 2.3 NM-NM Potential Energy Surface

The obtained pair potential energy expression for the NM-NM interactions is a polynomial in  $1/r$

$$V_{fit}^{NM-NM} = \sum_{j \in NM1} \sum_{k \in NM2} q_j q_k / r_{jk} + A_{jk} / r_k^4 + B_{jk} / r_k^5 + C_{jk} / r_k^8 \quad (18)$$

This expression can rightly reproduce the ab-initio data and gives a rather good fitting accuracy. Its quality can again be judged from its agreement with the underlying data points and the overall correlation (Figure 25).

**Table 9** Values of the parameters of the NM-NM pair potential (equation 18). Energies are given in kcal/mol.

j	k	A	B	C
C	C	-1 112.2	0.0	23 563.0
C	H	146.5868	0.0	0.0
C	N	-548.6524	0.0	12 299.0
C	O	-844.1313	2 375.6	2 375.6
H	H	9.7094	0.0	0.0
H	N	64.1848	0.0	0.8246
H	O	93.0748	0.0	0.0
N	N	323.2490	0.0	0.0
N	O	-87.7924	0.0	3 104.0
O	O	-353.2470	1 366.2	270.4317

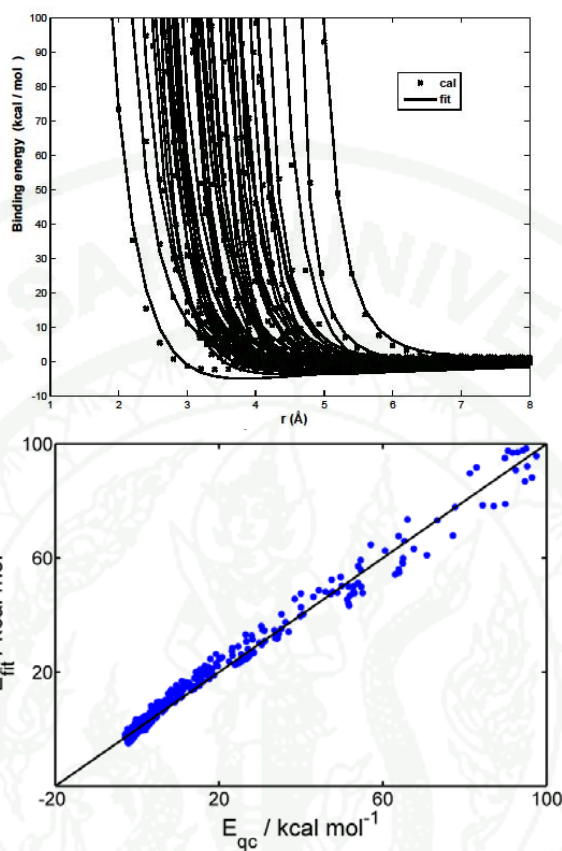


**Figure 25** (Upper part) NM-NM interaction: Quantum chemical (x) and fitted (solid lines) energies. (Left) Fitting accuracy of the the NM-NM potential energy function.

Due to the higher dimensionality of the NM-NM system compared to the NM-Au system (6 internal degrees of freedom versus 3), several thousand energy points had to be calculated and the various potential energy curves are shown in Figure 25. The number of non-zero parameters (Table 9) for the ten atom pairs is not overwhelming. Again, the atomic charges in the NM molecules were not changed.

A comparison between the two potential energy functions in terms of the various atom-atom pair terms is given in Figure 26. Since the partial charges are the same in both cases, the electrostatic contributions were excluded. The newly potential energy function is given in equation 18 while the generic one (Sorescu *et al.*,

2001) uses an  $\exp(-r)$  term for the repulsion and an  $r^{-6}$  term for attractive interactions beside the electrostatic terms.

Two main differences are present: in all curves the  $\exp(-x)$  term leads to a steeper repulsive part. This is a consequence of the values of the parameters and not of the functional form since  $r^{-8}$  is infinite for  $r = 0$  while  $\exp(-r)$  terms are finite. Further, all terms in the generic potential exhibit no or only extremely shallow minima, in contrast to the pronounced minimum for C-N in the newly potential energy function. Due to the fact of the completely different ways in which both energy expressions were derived, detailed comparisons are difficult but it can be safely stated that the generic expression acts as a ‘soft sphere plus coulomb’ - type of potential. The largest deviations between both potential energy functions can be seen for C-N and C-C. These centers are, however, shielded by hydrogen atoms and not in close contact with each other.

Since it also turned out (see below) that the MD results from both Sorescu’s (Sorescu *et al.*, 2001) and the newly potential energy function are very similar to each other, one can conclude that electrostatic interactions dominate also in the present model and the softer repulsive part plays a minor role. It should be noted that such an agreement between a typical generic function and a ‘specialized’ one is not normally to be expected. In contrary, often large discrepancies are found that render the use of the generic potential doubtful (Onthong *et al.*, 2004).

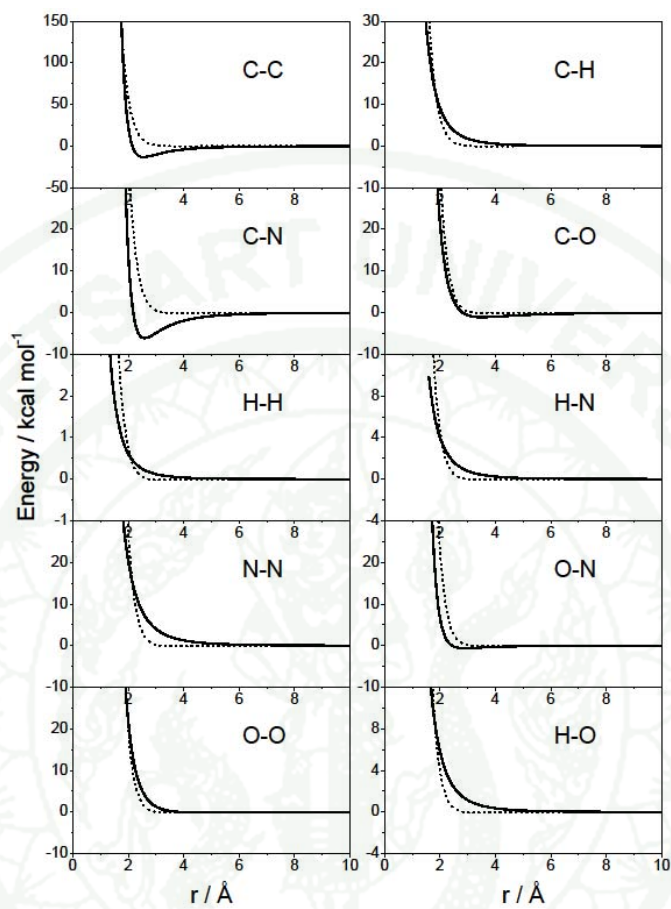


**Figure 26** Comparison of the various atom – atom terms of this work (solid lines) and the generic (dashed lines) NM-NM potential energy functions.

1943

### 3. Molecular Dynamics Simulation

#### 3.1 Au<sup>+</sup>-NM

The technical details of the simulation were given in chapter 2.3 of the ‘methods of calculations’ section. The trajectory was analyzed in terms of radial distribution functions (RDFs), denoted as  $g_{xy}(r)$

$$g_{xy}(r) = \left\langle \frac{dn_{xy}}{dr} \cdot \frac{1}{4\pi r^2 \rho_x N_y} \right\rangle \quad (19)$$

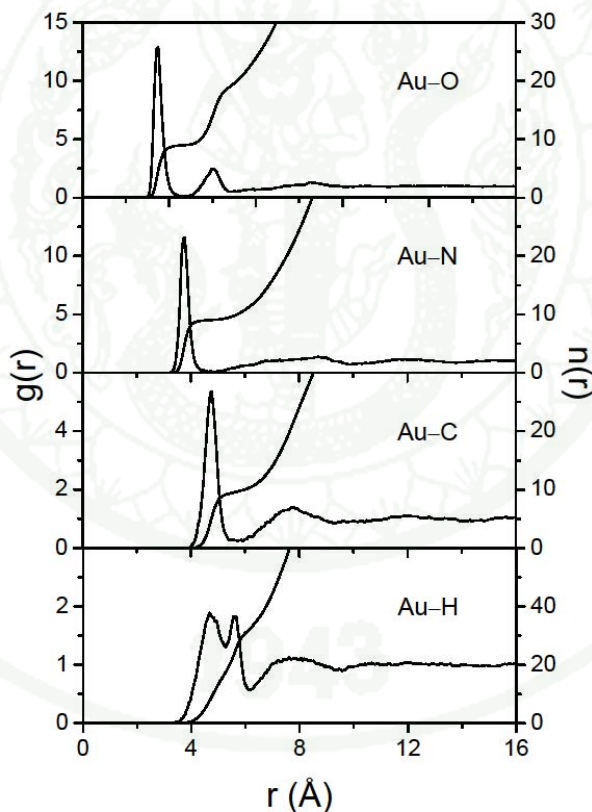
$N_y$  is the number of y center,  $\rho_x$  is the macroscopic density of x center and  $n_{xy}$  is the number of xy pairs.

Figure 27 shows all Au-NM pair correlation functions. The characteristic values of the RDFs are listed in Table 10. There the running integration numbers  $n_{xy}$ , defined according to

$$n_{xy}(r) = 4\pi\rho_0 \int_0^r r^2 g_{xy}(r) dr \quad (20)$$

are also given. All RDFs with the exception of  $g_{Au-H}$  have one sharp first peak that goes down to near zero after its maximum. The splitting of  $g_{Au-H}$  might be an artifact from the rigidity of the newly NM model. The number of N atoms under the first peak is about 10 for the generic NM pair potential energy function (Sorescu *et al.*, 2000; Sorescu *et al.*, 2001) and 9.01 if the new one is used. Such a difference – even if the Au-NM interactions are the same in both potentials – is not surprising. These respective values for  $n_{Au-O}$  are consistent with the values for  $n_{Au-C}$  and  $n_{Au-N}$ . Such a large solvation number is a consequence of the large distance (2.62Å) at which  $g_{Au-O}$  has its maximum. The second O atom of the NM molecules is found under the second peak of  $g_{Au-O}$  at distances of about 4.62 Å. Consequently,  $n_{Au-O}$  is 18.88 (my potential) and 20.48 after this second peak. This is somewhat remarkable since the attractive

potential at the site of one O atom and between two O atoms is similar (Figure 3) and the quantum chemical details that might lead to a preference of coordination to a single oxygen (section 2.1) are, of course, absent in the simple pair potential of this work. Looking at the conformations (a typical snapshot is plotted in Figure 28) one sees, however, that the more distant O atoms can interact favorably with the electropositive methyl groups, thus allowing for the crowded solvation shell. As mentioned above, virtually identical results for RDFs, coordination numbers and typical geometries are obtained if the NM-NM potential from (Sorescu *et al.*, 2000; Sorescu *et al.*, 2001) is used instead of the newly constructed one.



**Figure 27** Au-NM radial distribution functions from the simulation utilizing the newly constructed NM-NM potential energy function.

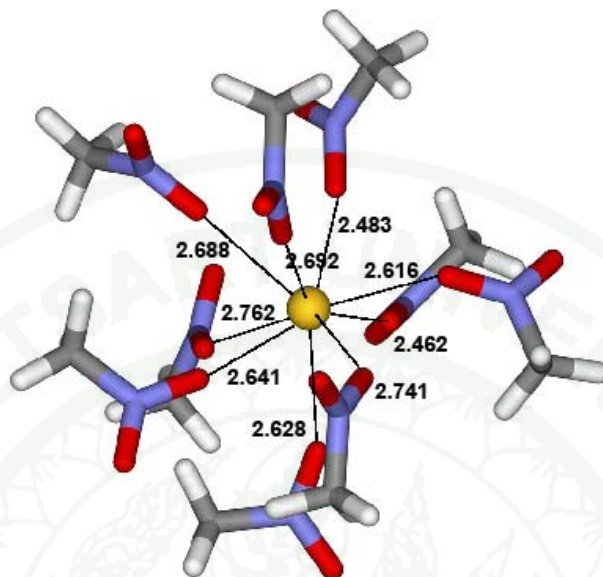


**Figure 28** Typical configuration of NM around Au<sup>+</sup>.

**Table 10** Characteristic values of the radial distribution functions for the Au<sup>+</sup>-nitromethane system with the new (a) and the generic (b) NM-NM potential energy function.

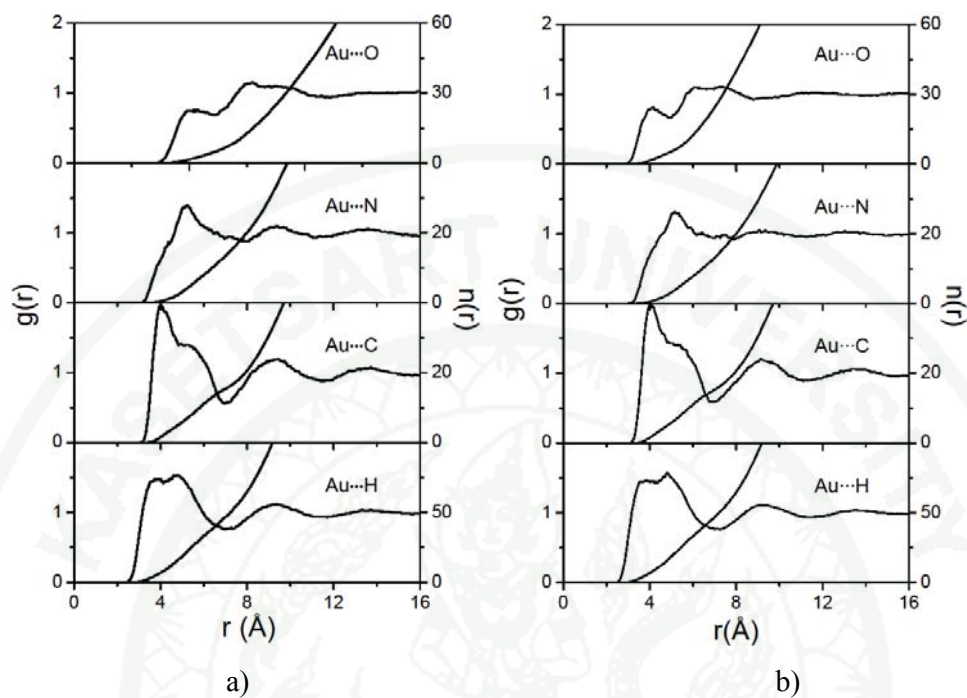
(a)										
pair	1 <sup>st</sup> shell					2 <sup>nd</sup> shell				
	r <sub>max</sub>	g(r <sub>max</sub> )	r <sub>min</sub>	g(r <sub>min</sub> )	n(r <sub>min</sub> )	r <sub>max</sub>	g(r <sub>max</sub> )	r <sub>min</sub>	g(r <sub>min</sub> )	n(r <sub>min</sub> )
Au-O	2.62	12.86	3.42	0.11	8.96	4.52	2.47	5.07	0.51	18.88
Au-N	3.77	11.57	4.67	0.07	9.01	8.72	1.36	10.06	0.73	49.37
Au-C	4.77	5.35	5.52	0.27	9.44	7.72	1.39	9.26	0.84	37.87
Au-H	4.67	1.89	6.17	0.57	32.43	7.62	1.12	9.56	0.90	121.01

(b)										
pair	1 <sup>st</sup> shell					2 <sup>nd</sup> shell				
	r <sub>max</sub>	g(r <sub>max</sub> )	r <sub>min</sub>	g(r <sub>min</sub> )	n(r <sub>min</sub> )	r <sub>max</sub>	g(r <sub>max</sub> )	r <sub>min</sub>	g(r <sub>min</sub> )	n(r <sub>min</sub> )
Au-O	2.62	13.44	3.52	0.08	9.84	4.62	2.69	5.17	0.37	20.48
Au-N	3.77	12.56	4.92	0.06	10.00	8.47	1.34	9.91	0.69	47.96
Au-C	4.67	5.39	5.92	0.14	10.60	7.67	1.53	10.16	0.72	49.34
Au-H	4.62	1.98	6.17	0.52	33.86	8.22	1.25	9.61	0.89	125.24

### 3.2 $\text{Au}(\text{CN})_2^-$ -NM and $\text{KAu}(\text{CN})_2$ -NM

RDFs of  $\text{Au}(\text{CN})_2^-$ -NM pair are shown in Figure 29a for the free  $\text{Au}(\text{CN})_2^-$  and Figure 29b for the  $\text{KAu}(\text{CN})_2$  ion-pair. The RDFs values showing the number of NM around  $\text{Au}(\text{CN})_2^-$  anion are listed in Table 12. RDFs are similar for both systems this is due to only one  $\text{KAu}(\text{CN})_2$  ion-pair is present in the system. The simulation of this one  $\text{KAu}(\text{CN})_2$  in NM solution was performed in order to compare the results with the X-ray diffraction experiment. In order to get a deeper insight to the solvation shell structure of dicyanoaurate(I) anion, a two dimensional distribution function in a cylindrical coordinate representation, which is defined as follows, was calculated. The origo was chosen to be the gold atom, the x-axis is given by the N-N' vector, radius is defined by Au-C(NM) and the angle between N-N' vector and Au-CN, respectively. From Figure 30, it can be clearly observed that the solvent molecules around the central ion, which has linear shape, are arranged in two distinct spheres. The existence of two solvation spheres can be predicted from the Au...C partial radial distribution function, but due to the size and shape of the central ion, the contribution of solvent molecules to the first or second solvation spheres are overlapping (shoulder on the right side of the first peak). Consequently the location of molecules belonging to first or second solvation sphere can be determined only from the higher order distribution function. However,  $\text{Au}(\text{CN})_2^-$  is solvated by 15-16 NM molecules in the first two solvation shells, see Table 15. Considering the orientation of NM around the  $\text{Au}(\text{CN})_2^-$  anion (Figure 31), it can be seen that all directions occur but the one with  $\text{CH}_3$  pointing towards the anion is preferred. A snapshot of  $\text{Au}(\text{CN})_2^-$ -NM system is shown in Figure 32. From Table 12, it is also visible that the presence of  $\text{K}^+$  does not affect to the first solvation shell of  $\text{Au}(\text{CN})_2^-$ . All features are similar for both free  $\text{Au}(\text{CN})_2^-$  and the  $\text{K}^+ / \text{Au}(\text{CN})_2^-$  simulation. However,  $\text{K}^+$  seems to affect the second NM shell for which  $n_{\text{Au-C}}$  is smaller by about 7 than in case of the free  $\text{Au}(\text{CN})_2^-$ . The distance between Au(I) and  $\text{K}^+$  is around 24 Å and the distance of the second shell of  $\text{Au}(\text{CN})_2^-$  and  $\text{K}^+$  is ~12 and 9 Å, respectively. The molecular radius of NM is ~3 Å, therefore, there is only space for one layer of NMs between the solvation shells of both cation and anion.



**Figure 29**  $\text{Au}(\text{CN})_2^-$ -NM radial distribution functions from the simulation utilizing the newly constructed NM-NM potential energy function. a) free  $\text{Au}(\text{CN})_2^-$  ion and b) ion-pair  $\text{KAu}(\text{CN})_2$  complex.

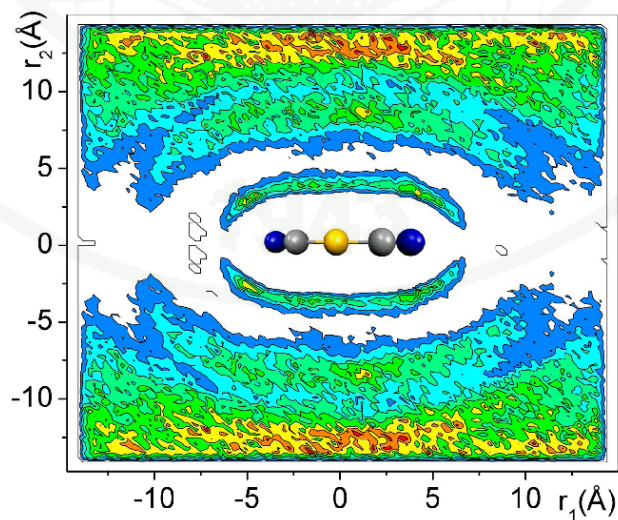


**Figure 30** Two dimensional projection of the distribution of nitromethane molecules around the central dicyanoaurate(I) ion,  $\text{Au}(\text{CN})_2^-$ .

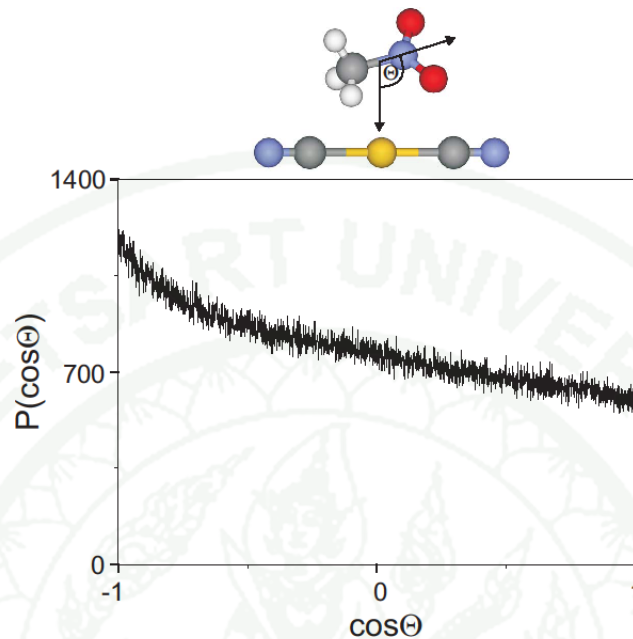


**Figure 31** Angular distribution function of  $\text{Au}(\text{CN})_2^- \cdot \text{NM}$  system.  $\Theta$ : angle between the dipole moment vector of the center of NM and Au(I) atom.

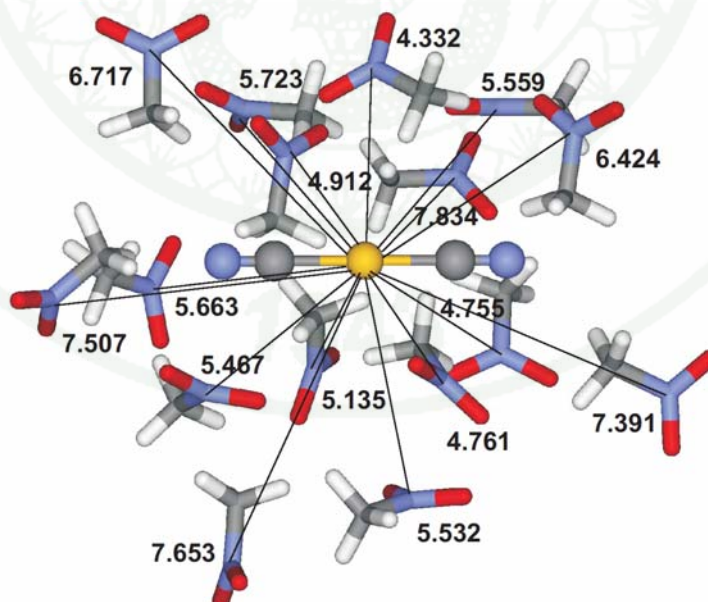


**Figure 32** NM coordinated around  $\text{Au}(\text{CN})_2^-$  anion.

Figure 33a shows RDFs of  $K^+$ -NM in the  $KAu(CN)_2$  systems and it looks like that of  $Au^+$ -NM (Figure 27). The number of O atoms under the first peak is about 9. These respective values for  $n_{K-O}$  are consistent with the values for  $n_{K-C}$  and  $n_{K-N}$ . However, in the second solvation shell, the appearance of  $Au(CN)_2^-$  counterion causes  $n_{K-N}$  of about 10 less than the absent case. Such a large solvation number is a consequence of the large distance (2.7-2.8 Å) at which  $g_{K-O}$  has its maximum. The second O atom of the NM molecules is found under the second peak of  $g_{K-O}$  at distances of about 4.6-4.7 Å.  $n_{K-O}$  has a value of about 21 at the end of this second peak.

Figure 33b shows RDFs of NM-NM in the  $KAu(CN)_2$  which is similar to that in the pure NM of recent study (Megyes *et al.*, 2007). One can see that the ions do not perturb the orientation between NM molecules in these diluted systems.

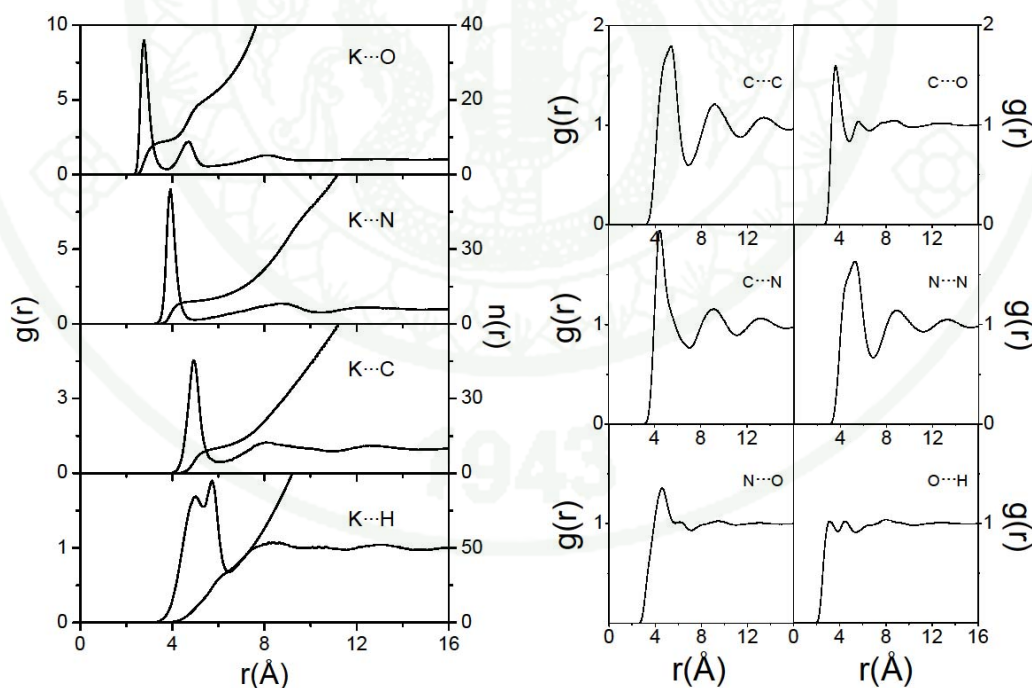


**Figure 33** (Left)  $K^+$ -NM and (right) NM-NM radial distribution functions of  $KAu(CN)_2$ -NM.

**Table 11** Characteristic values of the radial distribution functions for the (a) Au(CN)<sub>2</sub><sup>-</sup>-NM, (b) KAu(CN)<sub>2</sub>-NM systems.

(a)										
pair	1 <sup>st</sup> shell					2 <sup>nd</sup> shell				
	r <sub>max</sub>	g(r <sub>max</sub> )	r <sub>min</sub>	g(r <sub>min</sub> )	n(r <sub>min</sub> )	r <sub>max</sub>	g(r <sub>max</sub> )	r <sub>min</sub>	g(r <sub>min</sub> )	n(r <sub>min</sub> )
Au-O	4.27	0.76	4.82	0.69	4.51	6.17	1.15	8.87	0.93	55.58
Au-N	5.22	1.40	7.77	0.88	18.44	9.41	1.10	11.16	0.93	58.32
Au-C	3.97	1.97	6.97	0.56	15.25	9.46	1.20	11.56	0.88	66.41
Au-H	4.82	1.54	6.97	0.76	46.27	9.36	1.12	11.71	0.93	207.95

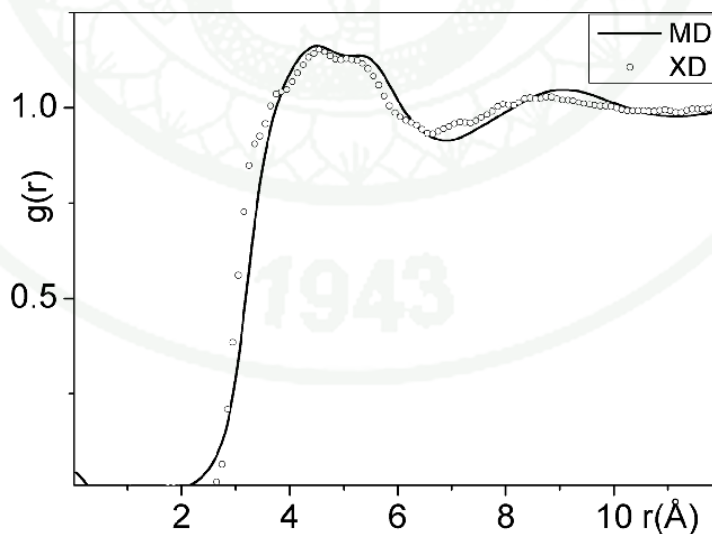
  

(b)										
pair	1 <sup>st</sup> shell					2 <sup>nd</sup> shell				
	r <sub>max</sub>	g(r <sub>max</sub> )	r <sub>min</sub>	g(r <sub>min</sub> )	n(r <sub>min</sub> )	r <sub>max</sub>	g(r <sub>max</sub> )	r <sub>min</sub>	g(r <sub>min</sub> )	n(r <sub>min</sub> )
Au-O	4.17	0.81	4.87	0.67	4.82	7.27	1.11	8.82	0.93	54.55
Au-N	5.17	1.31	7.92	0.92	19.44	9.07	1.05	11.31	0.96	60.18
Au-C	4.02	1.99	6.92	0.58	15.01	9.16	1.20	11.11	0.89	59.36
Au-H	4.77	1.57	7.02	0.76	47.21	9.21	1.11	11.36	0.93	190.49
K-O	2.77	8.99	3.77	0.36	9.03	4.72	2.20	5.57	0.55	20.65
K-N	3.92	9.01	4.97	0.26	9.08	8.67	1.37	10.46	0.76	51.33
K-C	4.92	4.53	5.97	0.44	10.14	8.07	1.24	11.01	0.88	57.12
K-H	5.72	1.90	6.47	0.68	34.76	8.37	1.07	9.71	0.99	117.25

### 3.3 X-ray diffraction experiment and comparison with the $\text{KAu}(\text{CN})_2\text{-NM}$ simulation

In order to have at least one stringent comparison between computationally and experimentally derived quantities, an X-ray diffraction measurement (performed by my co-workers Tünde Megyes, Tamas Radnai, Imre Bako and Szabolcz Balint from Chemical Research Centre of the Hungarian Academy of Sciences, Budapest, Hungary) was carried out on a 0.036 molar solution of  $\text{KAu}(\text{CN})_2$  in nitromethane.

The total radial distribution function obtained from this X-ray diffraction experiment is compared with the one calculated from  $\text{KAu}(\text{CN})_2\text{-NM}$  simulation in Figure 34. Taking into account the complicated atomic composition of the system, the agreement between both radial distribution functions is very satisfactory, giving credibility to the claim that the molecular dynamics simulations deliver a correct average picture of the structure of the solution.



**Figure 34** Comparison of the radial distribution function obtained from the X-ray diffraction experiment and MD simulation of  $\text{KAu}(\text{CN})_2\text{-NM}$ .

Energetic and geometric features of various gold(I)-nitromethane clusters, with Au(I) occurring as a free ion and the  $\text{Au}(\text{CN})_2^-$  complex, respectively, were calculated and discussed in the light of the peculiar properties of Au(I). Extensive quantum chemical calculations on  $\text{AuNM}_n^+$  and  $\text{Au}(\text{CN})_2^- \text{-NM}_n$  clusters were performed at the Hartree-Fock (HF) method with the LANL2DZ basis set for Au(I) and the D95V basis set for N, O, C and H. The especially strong binding of nitromethane in  $\text{AuNM}_2^+$  is found. This is because, even without forming a bond, the mixing of *s-d* into the wavefunction reduces the Au(I)-O repulsion, thus allowing the ligand to approach closer. For higher values of *n* the resulting geometries reflect the fact that the NM-NM interaction dominates over  $\text{AuNM}_n^+$  and  $\text{Au}(\text{CN})_2^- \text{-NM}_n$ . The coordination with a larger number of NM shows that the NM-NM tendency for chain formation dominates but  $\text{Au}(\text{CN})_2^-$  is not expelled from the clusters. Ab-initio pair energy surfaces for Au(I)-NM,  $\text{Au}(\text{CN})_2^- \text{-NM}$ ,  $\text{K}^+ \text{-NM}$ ,  $\text{K}^+ \text{-Au}(\text{CN})_2^-$  and NM-NM were derived by fitting simple analytical functions to quantum chemically calculated energies. These functions were then used to perform a molecular dynamics simulation of one Au(I) cation in 499 nitromethane molecules for the free Au(I) system and one  $\text{Au}(\text{CN})_2^-$  and one  $\text{K}^+$  ions in 459 nitromethane for the  $\text{KAu}(\text{CN})_2$ . The simulations were performed in the NVT ensemble at room temperature. A comparative simulation with an older, generic NM-NM potential energy function was also performed for the Au(I)-NM case and gave nearly identical results with respect to the analyzed quantities. The first solvation shell around the gold ion of the free Au(I) cation consists of 9-10 nitromethane molecules with a distance of about 2.6 Å for the first and about 4.6 Å for the second O atom to  $\text{Au}^+$ . The  $\text{Au}(\text{CN})_2^-$  anion is surrounded by 15-16 nitromethane molecules in the first solvation shell with a Au-C distance of 4.0 Å and 9.2 Å for the second solvation shell. An X-ray diffraction experiment on a diluted solution of  $\text{KAu}(\text{CN})_2$  in nitromethane was performed as well. The resulting total radial distribution function (RDF) agrees well with the one obtained from the molecular dynamics simulation.

## Effect of substituent group on dissociative electron attachment of purines: quantum chemical study

### 1. Energetics

The values of BDEs and  $E_{DEA}$  calculated at G2MP2 level of theory are shown in Table 13. This work focuses on Ad, Pu and 6-fPu. It needs electron energy around 4.3-5.2 eV to remove H atom from all neutral purines. BDE of Ad (4.38 eV) is in good agreement with the experimental average dissociation energy of 3.92-4.35 eV (Zierhut *et al.*, 2004) and 4.32-4.74 eV (Hunig *et al.*, 2004). The energy required for formation the  $M^-$  anions or  $E_{DEA}$  is considerably less than the one needed for bond-breaking in the neutral case since closed-shell anions are energetically favored over neutral radicals. It is found that the smallest energy less than 1 eV required for abstraction of H from the N9 position in all anionic cases. This energy is about half the one required to dissociate the next bond which is the N6-H for Ad and the C8-H for Pu and 6-fPu cases. In order to remove H from the N9 site energies of 0.54, 0.72 and 0.94 eV required, respective for 6-fPu, Pu and Ad, are in good agreement to the experimental values of  $0.72 \pm 0.07$  eV (Denifl *et al.*, 2007) for Pu and  $0.84 \pm 0.07$  eV (Denifl *et al.*, 2007) and 1.01 eV (Abdoul-Carime *et al.*, 2005) for Ad. This leads to the first peak in the spectrum of  $M^-$  amounts as a function of electron energy appears at lower energies for Pu than Ad. The results reveal that the substituent group at the C6 site of the purine ring affects the electron-energy requirement of similar molecules. The electron-donating  $-NH_2$  group gives more electron density into the purine ring while it is reduced by the electron-withdrawing  $-F$  group. This leads the molecule with less electron density in the ring attach the external low-energy electron. It can conclude that seemingly the G2MP2 method works well for describing DEA of familiar molecules. The present values of BDEs and  $E_{DEA}$  of Ad are very similar to those from DFT studies reported by Evangelista *et al.* (2004) (within 0.02 eV) and in fair agreement with Zierhut *et al.* (2004) (within 0.35 eV).

The electron affinity (EA) of  $M^-$  radical must be considered because it refers to the stability of product  $M^-$  anion. The difference between the neutral BDE

**Table 12** Bond dissociation energies (BDEs) of hydrogen atoms in neutral molecules and the energies required for the dissociative electron attachment  $MH + e^- \rightarrow M^- + H^+$  ( $E_{DEA}$ ) from G2(MP2) calculations. The values (in eV) include electronic energy and zero-point vibration energy.

H removal from	6-Dimethyladenine		Adenine		Purine		6-Fluoropurine		8-Fluoropurine	
	BDE	$E_{DEA}$	BDE	$E_{DEA}$	BDE	$E_{DEA}$	BDE	$E_{DEA}$	BDE	$E_{DEA}$
C2	5.20	3.05	4.74	3.63	4.91	3.42	4.85	3.13	4.90	3.29
C6/N6	4.54	3.29	4.69	1.72	4.81	3.16	-	-	4.82	2.99
C8	5.20	1.97	5.06	2.53	5.20	2.33	5.11	2.19	-	-
N9	4.66	1.41	4.38	0.94	4.81	0.72	4.78	0.54	-	0.32
Expt.*	$1.07 \pm 0.07^c$		$3.92-4.35^a$	$0.84 \pm 0.07^c$	$0.72 \pm 0.07^c$					
			$4.32-4.74^b$	$1.01^d$						

\*Experimental BDE values for H removal from all sites and  $E_{DEA}$  values for H removal from the N9 sites.

<sup>a</sup>Zierhut *et al.*, 2004, <sup>b</sup>Hunig *et al.*, 2004, <sup>c</sup>Denifl *et al.*, 2007, and <sup>d</sup>Abdoul-Carime *et al.*, 2005.

and anionic  $E_{DEA}$  is equal to the adiabatic electron affinity (AEA) of  $M'$  radical. Thus the  $AEA(M')$  at N9 position is calculated to be 3.44, 4.09 and 4.24 eV for Ad, Pu and 6-fPu, respectively. AEA of N9-dehydrogenated adenine radical,  $AEA(Ad_{N9})$  of this work agrees with that from the calculation at B3LYP/DZP++ level of theory with zero-point correction of 3.23 eV reported by Evangelista *et al.* (2004). Other  $AEAs(Ad')$  at other sites are also in agreement. The positive AEA shows that the extra electron prefers to be captured by the  $M'$  radical in order to form the more stable  $M'$  anion. A larger  $AEA(M')$  means the lower-energy electron is easier trapped and the  $M'$  anion is more stable, therefore, 6-fPu $_{N9}^-$  is the most stable anion than the cases of Pu and Ad.

## 2. Electronic properties calculation

### 2.1 Vibrational frequencies

Vibrational frequencies are routinely calculated because the G2(MP2) calculations require a harmonic frequency calculation at the HF/6-31G(d,p) level. Moreover, they can be obtained from the UB3LYP/cc-pVTZ level of theory as well. In this work, the N-H and C-H stretching modes are of particular importance. They are identical between the the three molecules, an indication that the substituent groups do not alter the basic electronic structure in the purine ring. For all three molecules, these modes are nearly uncoupled to vibrations of other parts of the molecules except that the C2-H and C6-H bonds are coupled each other for Pu. For all purines except Ad, the N9-H stretching is the highest vibrational mode in the molecule while for Ad the asymmetric stretching mode of the amine group appears at 3982  $\text{cm}^{-1}$  (G2MP2) and 3742  $\text{cm}^{-1}$  (UB3LYP/cc-pVTZ). It is found that the lowest-energy configurations in all molecules retain  $C_s$  symmetry as checked by repeating all calculation without symmetry constraints. Normally, frequency relates to bond strength and the energy required for bond breaking via the Pauling relationship. It can be seen that the N9-H bond is the most difficult to break. This neither holds for BDE nor  $E_{DEA}$ . As a consequence, the frequency is not correlated with the bond breaking energy in the presence of a free electron.

**Table 13** Vibrational frequencies ( $\text{cm}^{-1}$ ) of neutral adenine (Ad), purine (Pu) and 6-fluoropurine (6-fPu).

Stretching mode	Ad	Pu	6-fPu	Ad	Pu	6-fPu
	UB3LYP/cc-pVTZ			HF/6-31G(d)		
C2-H	3161	3173	3183	3388	3403	3414
C6-H/N6-H	3610(sym), 3742(asym)	3160	-	3849(sym), 3982(asym)	3403	-
C8-H	3238	3234	3238	3447	3448	3453
N9-H	3649	3646	3646	3909	3908	3906

## 2.2 Dipole-bound state anion

T. Sommerfeld *et al.* have proposed that the extra electron is induced to be bound to the molecule by a large dipole moment to form a dipole-bound state (DBS) and then this bound electron transfers into a valence orbital inducing DEA process (Sommerfeld, 2005). The extra electron in dipole-bound state (DBS) is trapped into an unoccupied diffuse molecular orbital. To obtain the structure and energy of DBS anions, six basis sets of *sp* orbital with the exponents equal to 0.01, 0.002, 0.0004, 0.00008, 0.000016, and 0.0000032, and a set of *p* orbital with the exponent 0.036 are added for atoms to which the positive end of dipole moment point for describing a diffuse orbital (Jalbout and Adamowicz, 2001a; Jalbout and Adamowicz, 2001b; Stepanian *et al.*, 2003). In Ad case, for example, these basis sets are defined at H of C8 site. Figure 35 shows the optimized structure of DBS Ad anion calculated at the UMP2 level and basis set of 6-31++g\*\*(5D) for all atoms but basis set for H at C8 site is augmented with six basis sets of *sp* orbital and a set of *p* orbital as mentioned above. It is clearly seen that the extra electron is in a diffuse molecular orbital which away from the molecular framework. Therefore the structure of the DBS Ad anion is similar to the neutral molecule. The calculated DBS Ad anion energy is a little bit more stable than that of the neutral by 0.2 meV. The calculated energy is ~10 times smaller than the experimental values (Desfrancois *et al.*, 1996).

This may be due to the basis set-dependence of the bound-state anion. The basis set used in the work is recommended for molecules having dipole moment larger than 3 Debyes. Nevertheless it can be seen that DBS anions are more stable than the neutral molecules and, as a consequence, the potential energy surface (PES) of the DBS anions is lower and parallel to that of their corresponding neutral.

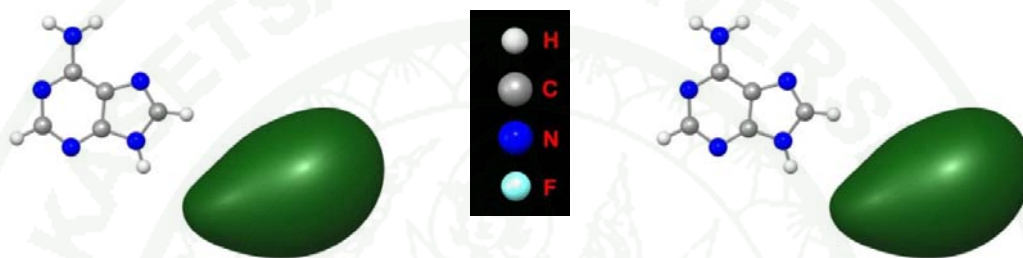


**Figure 35** (Left) LUMO of adenine neutral and (right) HOMO of dipole-bound state adenine anion, see text.

### 2.3 Dipole moment

The calculated values of the dipole moment for these five molecules do not depend much on method and basis set (Table 15). Comparing to Pu, it is clearly seen that the electron-donating  $\text{-NH}_2$  (for Ad) and  $\text{-N(CH}_3)_2$  (for 6-dimAd) groups reduce the magnitude of the dipole moment and change its direction but it seems not possible to rationalize the change by some simple argument like, for example, an electron-donating  $\text{-N(CH}_3)_2$  group. It is interesting to note that the dipole moment vector in purine deviates by about 30 % from the direction of the N9-H bond while 6-dimAd it is nearly perpendicular to it. On the other hand, the electron-withdrawing  $\text{-F}$  group of 6-fPu does not change the direction but only alter the magnitude of the dipole moment. The magnitude of the dipole moment vector decreases from 4.69 D (6-fPu) to 3.68 D (Pu) to 2.36 D (Ad) to 2.16 (6-dimAd) and move its positive end out of the direction of the N9-H bond (Figure 36). This obviously causes considerably different electrical field situation at the N9-H bond for these molecules. The reason for this is provided by the electrostatic potentials (ESP) of the molecules. In the case of molecules which have a small dipole moment and their dipole vector moves out of

the direction of the N9-H bond in larger degree, its  $E_{\text{DEA}}$  value is larger. Especially for 6-dimAd, the difference between  $E_{\text{DEA}}$  for abstracting H atom from N9 and C8 sites is closer than in Pu case. However, other factors must be taken into account to estimate the energetical order for bond cleavage. Since the direction of dipole moment seems to relate to  $E_{\text{DEA}}$ , dipole moment and  $E_{\text{DEA}}$  of 8-fluoropurine (8-fPu) are calculated. The calculated dipole moment of 8-fPu is only 2.72 D and its direction nearly coincides with the direction of the N9-H bond. The H atom is still easiest removed from N9 site but the lowest electron energy of 0.32 eV is needed. This means the direction of dipole moment does indeed correspond to the different  $E_{\text{DEA}}$  of familiar molecules but its magnitude does not. Therefore, the dipole moment just only acts as antenna to induce the extra electron with any energy levels to be bound to the molecule via the dipole-bound state.

**Table 14** Dipole moment of 6-dimethyladenine (6-dimAd), adenine (Ad), purine (Pu), 6-fluoropurine (6-fPu) and 8-fluoropurine (8-fPu) calculated with three methods and basis sets.

	UB3LYP/ cc-pVTZ	MP2/ aug-cc-pVDZ	MP2/ 6-311+G(3df,2p)*
6-dimethyladenine	2.16	2.28	2.30
Adenine	2.36	2.51	2.52
Purine	3.68	3.77	3.77
6-fluoropurine	4.69	5.25	5.18
8-fluoropurine	2.72	2.51	2.54

\*from G2MP2 calculations.

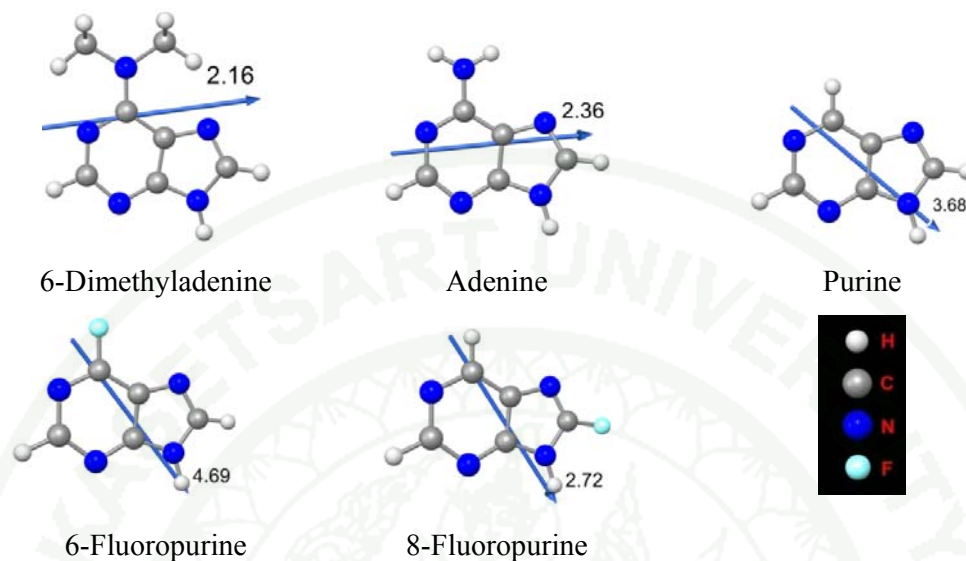


**Figure 36** Molecular dipole moment of 6-dimethyladenine (6-dimAd), adenine (Ad), purine (Pu), 6-fluoropurine (6-fPu) and 8-fluoropurine (8-fPu) obtained from UB3LYP/cc-pVTZ calculations. Arrows point to the positive end of dipole moment.

#### 2.4 Electrostatic potential

One of the questions of this work is why the rather distant groups (C6-H, C6-NH<sub>2</sub> and C6-F) that differentiate the purine derivatives cause remarkable different spectra. Experimentally, the loss of H atom from Ad and Pu is bond- and site-selective depending on the incident electron energy (Denifl *et al.*, 2007). It is noted that different electronic properties origin these phenomena. The electrostatic potential (ESP) of the molecule influences the shape of the diffuse anionic molecular orbital (MO). This obviously causes a considerable different electrical field situation at the N9-H bond for these purines, see Figure 37 showing the ESP projected onto surfaces of constant electron density.

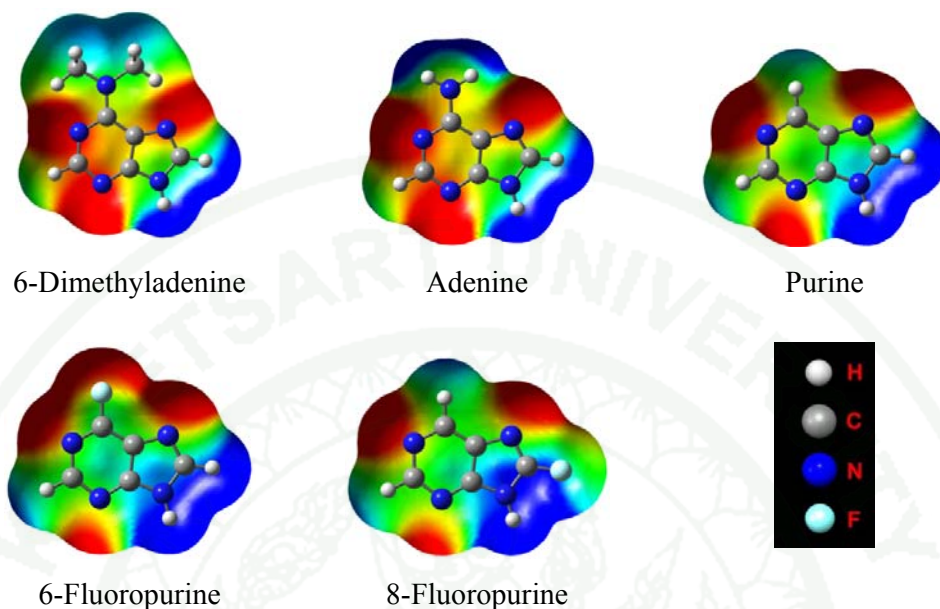


**Figure 37** Electrostatic potential maps of the neutral 6-dimethyladenine (6-dimAd), adenine (Ad), purine (Pu), 6-fluoropurine (6-fPu) and 8-fluoropurine (8-fPu) molecules obtained from UB3LYP/cc-pVTZ calculations.

The extra electron prefers to attach the molecule at strong positive ESP. Only large region of positive ESP in Pu, 6-fPu and 8-fPu is near the N9-H site and the neighboring C8-H sites yielding these two bonds firstly break before the C2-H (for Pu and 6-fPu) and the C6-H (for Pu) bonds which are outside the strong positive ESP. In case of Ad and also for 6-dimAd besides this positive region around the N9-H bond region a second positive ESP region appears around the  $\text{NH}_2$  and  $\text{N}(\text{CH}_3)_2$  groups (see Figure 37). Therefore the incoming electron is firstly possible to attack these two positive ESPs and the extra electron energies needed for dissociation of the N6-H/C6-H, C8-H and N9-H bonds are smaller than that of the C2-H bond for Ad and 6-dimAd. Moreover the C6-H bond for 6-dimAd which is in the less strong positive ESP than the N9-H and C8-H bonds, thus, the C6-H bond breaks after these two bonds. Since regions of strong positive ESP attract an electron, the various functional groups leading to different ESPs should therefore influence the DEA spectrum. At this point it is clearly seen that the ESP indicates the site-selectivity of DEA process.

## 2.5 Energy level of virtual $\sigma^*$ molecular orbitals

The order of the virtual  $\sigma^*$  molecular orbitals (MO) of the neutral molecule (which could be occupied in the metastable anion) can be used for addressing which bond is easier to dissociate. In Figure 38 these virtual  $\sigma^*$  MOs (calculated with the UB3LYP/cc-pVTZ method and basis set) are plotted with a small isovalue of isodensity maps at the equilibrium geometry of the neutral molecules. Indeed the lowest virtual  $\sigma^*$  MO (LUMO+3) of the neutral molecules show the expected differences. It is remarkable that the lowest virtual  $\sigma^*$  MO which is LUMO+3 for all purines has a wave function density around the region of N9-H and C8-H bonds. It can be clearly seen that there is no wave function density in the C6-H region for Pu, 6-fPu and 8-fPu whereas there is one in the C6-NH<sub>2</sub> and C6-N(CH<sub>3</sub>)<sub>2</sub> regions of Ad and 6-dimAd, respectively. It seems the N9-H, N6-H (for Ad) and C8-H bonds can dissociate simultaneously. But when increasing the isovalue the wave function of LUMO+3 orbital mainly located at the N9-H bond, see Figure 39. Therefore, the small-energy electron prefers to attack this MO than the higher virtual  $\sigma^*$  MOs. The next higher virtual  $\sigma^*$  MOs have additional density at the C8-H site (the N6-H site for Ad), also in accordance with the ESP. As a result, the N9-H bond is the easiest to break and the N6-H bond dissociates more easily than the C8-H bond for Ad case. Therefore the ease of H abstraction is N9>C8>C2 for 6-fPu, N9>C6>C2 for 8-fPu, N9>N6>C8>C2 for Ad and N9>C8>C6>C2 for Pu. Consequently, the bond breaking for DEA process obeys to the energy level of virtual  $\sigma^*$  MO for these molecules. However 6-dimAd is the exceptional case. The order of virtual  $\sigma^*$  MOs is N9>C6>C8>C2 but the order of H atom removed for each site is N9>C8>C2>C6. The ESP of 6-dimAd must be considered. The H atom is removed from the C8 site before the C6 site because the C8 one is in the stronger positive ESP than the C6 one. But the competition of bond cleavage between the C6-H and the C2-H sites of 6-dimAd can be addressed by the electron affinity of M<sup>•</sup> radical and the stability of M<sup>-</sup> anion.

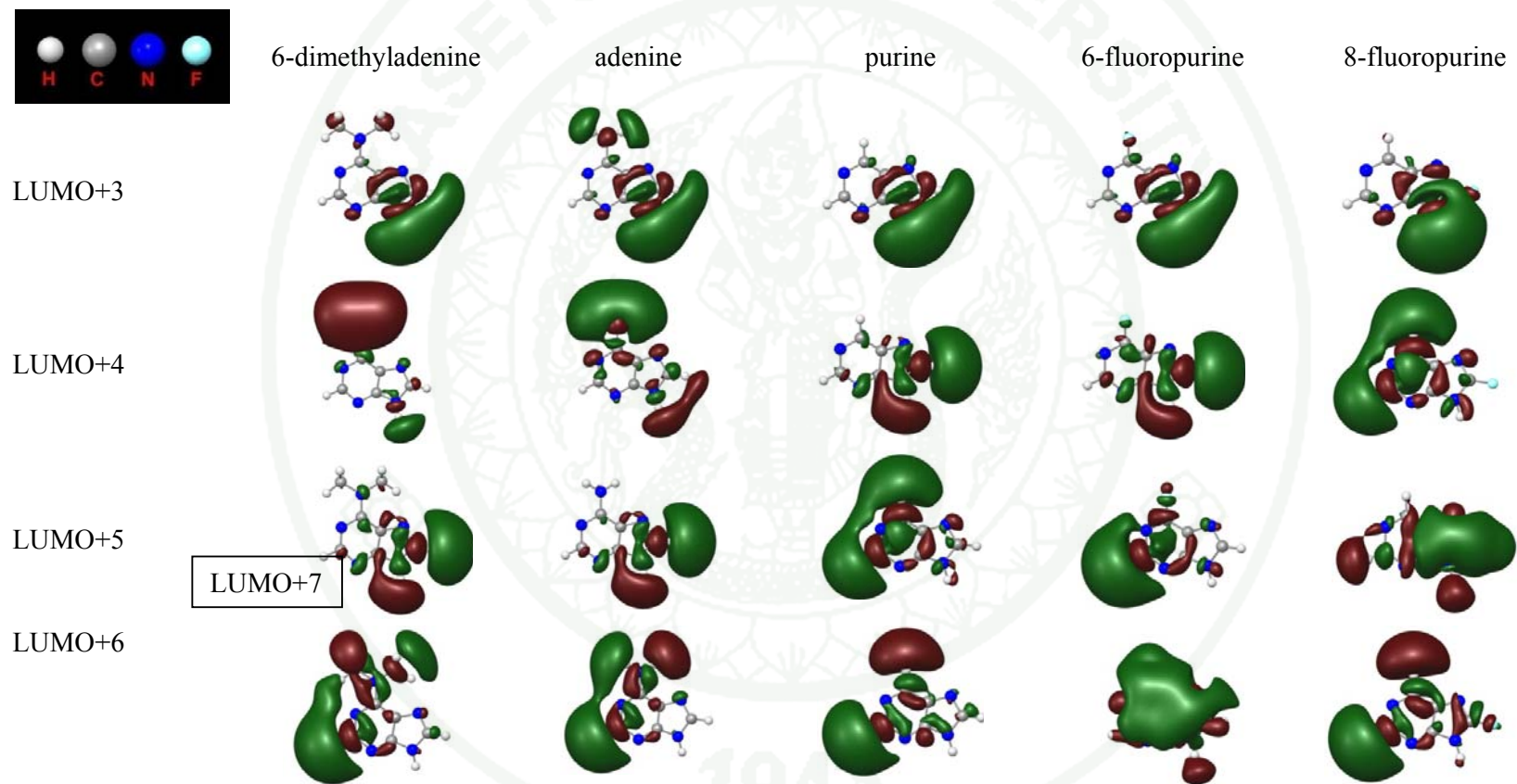


**Figure 38** Isodensity maps (isovalue=0.02) of the first four virtual  $\sigma^*$  molecular orbitals at equilibrium geometry of the neutral 6-dimethyladenine (6dimAd), adenine (Ad), purine (Pu), 6-fluoropurine (6-fPu) and 8-fluoropurine (8-fPu) molecules obtained from UB3LYP/cc-pVTZ calculations. LUMO+7 of 6-dimAd is shown instead of its LUMO+6.

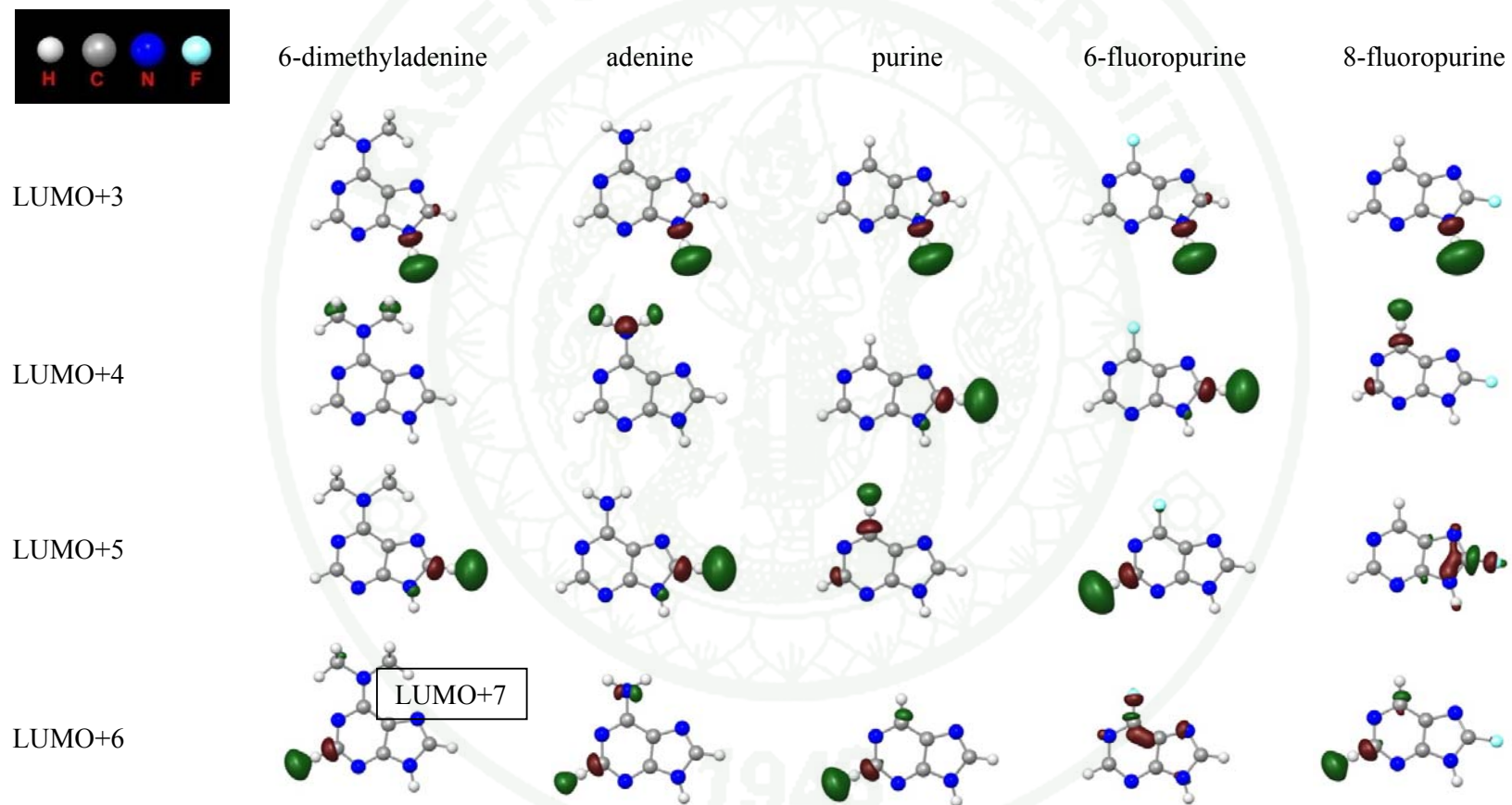


**Figure 39** Isodensity maps (isovalue=0.08) of the first four virtual  $\sigma^*$  molecular orbitals at equilibrium geometry of the neutral 6-dimethyladenine (6-dimAd), adenine (Ad), purine (Pu), 6-fluoropurine (6-fPu) and 8-fluoropurine (8-fPu) molecules obtained from UB3LYP/cc-pVTZ calculations. LUMO+7 of 6-dimAd is shown instead of its LUMO+6.

## 2.6 Electron affinity (EA) of the dehydrogenated M' radical

In previous section, the order of  $\sigma^*$  MO cannot predict the bond cleavage of the bonds located out of the very strong positive ESP, for example, C2-H and C6-H bonds of Pu, 8-fPu and 6-dimAd. For instance, when considering the DEA of 6-dimAd, it is found that the electron energy required for removing H from C6 site is higher ( $\sim 0.3$  eV) than that for C2 site although the virtual  $\sigma^*$  MO corresponding to the C6-H bond are lower in energy (LUMO+4 and LUMO+6 --this orbital does not show in Figures 38-39) than that of the C2-H bond (LUMO+7). To state this, the adiabatic electron affinity (AEA) of M' radical must be considered. This term refers to the stability of product M' anion. AEA of 6-dimAd<sub>C2</sub>' radical is larger ( $\sim 0.90$  eV) than 6-dimAd<sub>C6</sub>' radical. Therefore, 6-dimAd<sub>C2</sub>' anion is formed more preferable than 6-dimAd<sub>C6</sub>' anion leading the smaller E<sub>DEA</sub> for removing H from C2 site than C6 site. This can also address the bond cleavage at the C2 and C6 sites for Pu and 8-fPu. The Pu<sub>C6</sub>' and 8-fPu<sub>C6</sub>' anions are more stable than Pu<sub>C2</sub>' and 8-fPu<sub>C2</sub>' anions around 0.16 and 0.22 eV, respectively. So E<sub>DEA</sub> for the C6-H bond breaking is smaller than that of the C2-H bond. Moreover, from Table 12, all purines (in all regions of ESPs) have the larger EAs of M<sub>N</sub>' radicals than those of M<sub>C</sub>' radicals, hence, a H atom is removed from nitrogen site before carbon site.

## 2.7 Electronegativity

All N-H bonds require smaller electron energies for removing H than the C-H bonds. This is due to the larger electronegativity of nitrogen, compared to carbon. The N-H bond is more ionic in character than the covalent C-H one. The extra electron can be easily located at nitrogen atom than carbon atom. When N-H bond is breaking the extra electron is induced to stay near nitrogen. The corresponding nitrogen anion, M<sub>N</sub>' , is more stable than the carbanion, M<sub>C</sub>' because there is electron-localized over the purine rings in the case of M<sub>N</sub>' while the electron is located at the carbon center for M<sub>C</sub>' (Evangelista *et al.*, 2004).

Now it can be concluded, for this section, that there are four main factors to control the ease of the N-H/C-H bond dissociation: 1) ESP, 2) the energy level of virtual  $\sigma^*$  MOs, 3) the electron affinity of dehydrogenated M' radical and 4) electronegativity of atoms. The difference in the ESP and the electronegativity of atom cause site- and bond-selective of the DEA reaction, respectively, while the energy of virtual  $\sigma^*$  MOs of N-H/C-H bonds is a reason for both bond- and site-selective on DEA process.

### 3. Potential energy curves

The previous section showed to predict which bond dissociates most easily and what are the reasons but it cannot yet describe how large electron the energy for H dissociation at each site actually is. In terms of the experimental spectra, the calculations can give a lower limit for the occurrence of the peaks but not their actual position. Many studies (Anusiewicz *et al.*, 2005; Kumar and Sevilla, 2008; Li *et al.*, 2004; Scheer *et al.*, 2004) showed that potential energy curves of neutral and anionic species can answer this question. Previous section shows that H atom at N9 site is removed easiest. Therefore, neutral and anionic potential energy curves as a function of N9-H bond length is interesting.

#### 3.1 Calculation of anionic states

This method was tested for Ad case. Electron affinities (EAs) of Ad obtained from UOVGF/aug-cc-pVDZ calculations are plotted as a function of N9-H distances and shown in Figure 40. It reveals that, at  $r[\text{N9-H}] \sim 1.4 \text{ \AA}$ , EA values are small positive indicating this electron collision method cannot describe the metastable part of Ad.

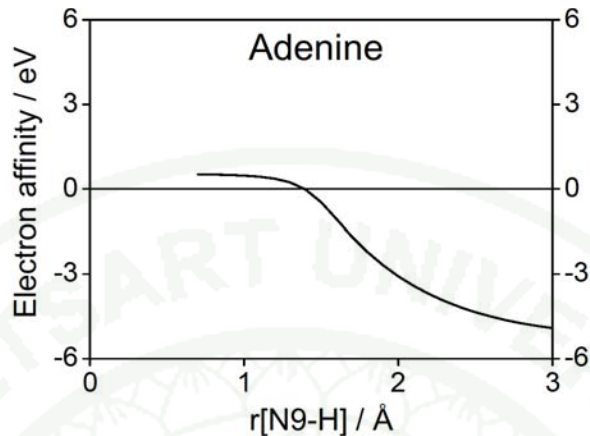


**Figure 40** Electron affinity curves of adenine as a function of N9-H bond length.

The metastable part is then obtained by using charge-stabilization and extrapolation methods, see Figure 41. The unoccupied MOs that were treated with UOVGF/aug-cc-pVDZ method are also shown in Figure 41.a.1. These orbitals are LUMOs for the corresponding neutral in curve b). It can be seen that these two methods gave the similar EA curve. The anionic PEC (curve c) is a product of curve a.1) and b). The electron energy of  $\sim 2.5$  eV, for example, cannot excite the molecule and lead it loses its own H atom at N9 site. So, curve c) cannot represent the DEA of metastable adenine anion. Therefore, this method is not suitable for constructing PEC of metastable anion of purine and its derivatives.

1943

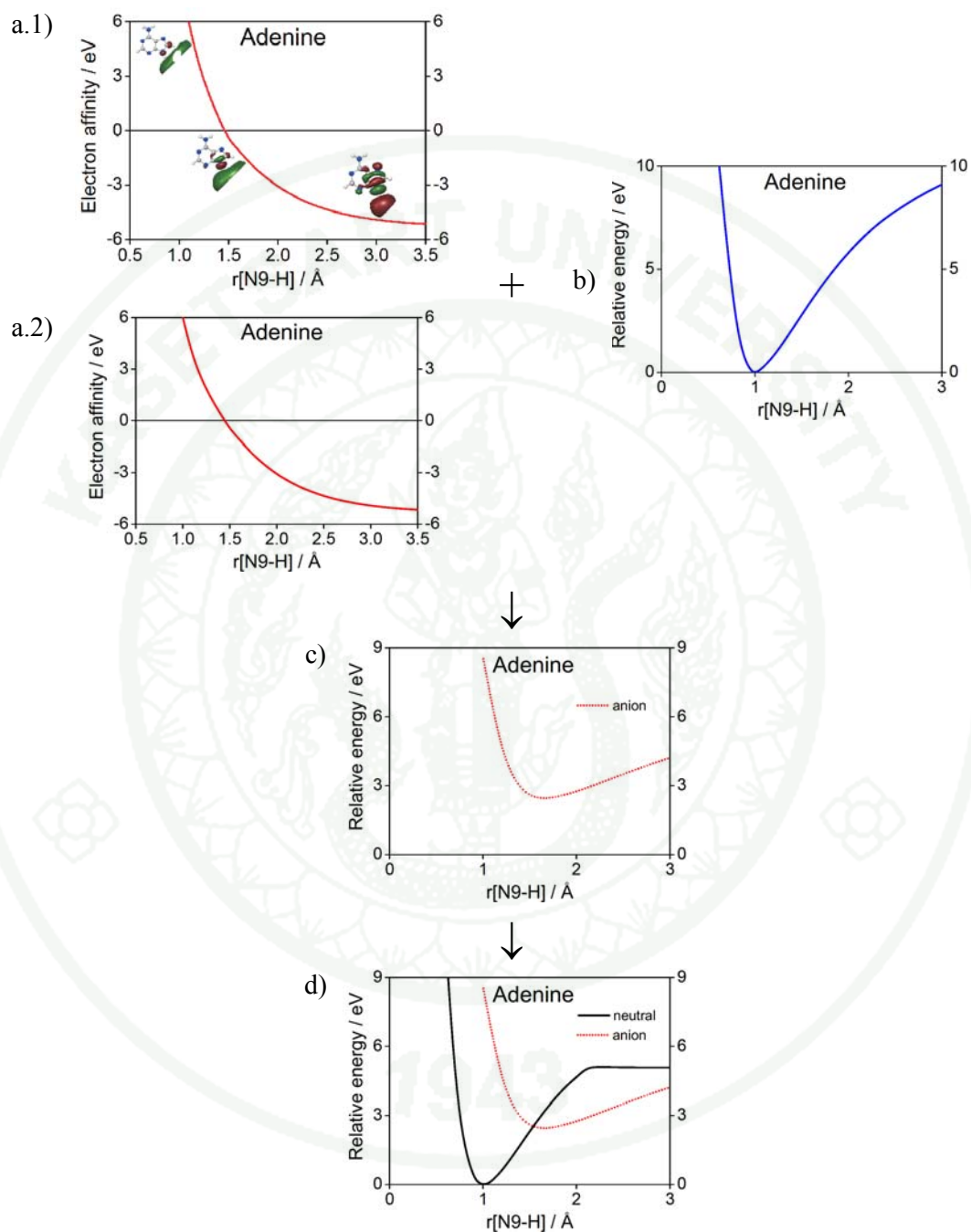


**Figure 41** a) Electron affinity curve of Ad obtained by using; 1) charge-stabilization and 2) extrapolation method, together with LUMOs of  $\text{AdH} \rightarrow \text{Ad}^- + \text{H}^+$  reaction. Isovalue of orbital plot =  $0.004 e/\text{\AA}$ . b) Neutral potential energy curve for  $\text{AdH} \rightarrow \text{Ad}^- + \text{H}^+$ . c) A resulted anionic potential energy curve of Ad. d) Neutral curve for  $\text{AdH} \rightarrow \text{Ad}^- + \text{H}^+$  together with anionic curve.

### 3.2 Density functional Theory

From previous section, the above methods cannot provide the reliable potential energy curve of metastable anions and cannot give any information concerning electronic properties. These can be done by the technique described in the section of methods of calculation. Figure 42 shows the adiabatic neutral and anionic PESs with zero-point energy (ZPE) correction along the N9-H bond length for Pu, Ad and 6-fPu calculated at the UB3LYP/cc-pVTZ level together with the vibrational energy levels for the ground state and the 1<sup>st</sup>- 4<sup>th</sup> excited states. The  $\sigma^*$  MOs concerning the N9-H bond breaking is plotted in Figures 38-39.

The BDE calculated at UB3LYP/cc-pVTZ level is 4.46 eV (6-fPu), 4.48 eV (Pu) and 4.16 eV (Ad). BDE of Ad agrees well with the experimental values of 3.92-4.35 eV (Zierhut *et al.*, 2004) and 4.32-4.74 eV (Hunig *et al.*, 2004). While  $E_{DEA}$  considered as the threshold energy for removing H atom is evaluated to be 0.71 eV (6-fPu), 0.92 eV (Pu) and 1.18 eV (Ad). Therefore the calculated AEA of M<sup>•</sup> radical is 3.75 eV (6-fPu), 3.56 eV (Pu) and 2.98 eV (Ad). These AEA values are the same tend but underestimate energies within 0.5 eV compared to G2MP2. The barrier of this reaction is about 0.99, 1.18 and 1.28 eV for 6-fPu, Pu and Ad, respectively.

Focus on  $r[\text{N9-H}] \approx 2.0\text{-}2.2 \text{ \AA}$ ,  $E_{DEA}$  is estimated to be 0.62, 0.79 and 1.05 eV for 6-fPu, Pu and Ad, respectively. These energies are lower ( $\sim 0.1$  eV) than those of H atom loss to infinity distance. In all neutral purine molecules, the 1<sup>st</sup> vibrational motion along the N9-H stretch has a characteristic energy of 0.64 eV. If the reaction is addressed via the neutral curve, it seems that the structure peak in DEA spectra cannot appear in Pu and Ad at this energy, except 6-fPu, because it lies below the asymptotic energy of separation into M<sup>•</sup> + H. But their next  $v=2$  energy level can tunnel through the barrier. However, the excess electron is captured in the dipole-bound state. The dipole-bound state anion curve should be considered instead of neutral curve. Consequently, all neutral curves will shift to the lower energy in some extent depending on the dipole-bound binding energy of anion. Dipole-bound electron

affinities (DBEAs) have been measured using photoelectron spectroscopy and Rydberg electron-transfer studies. The average DBEAs are adenine,  $0.012 \pm 0.005$  eV; uracil ( $\sim 4.6$  D),  $0.089 \pm 0.005$  eV; thymine ( $\sim 4.1$  D),  $0.065 \pm 0.005$  eV (Hendricks *et al.*, 1998; Schiedt *et al.*, 1998). Due to the lack of accurate DBEAs of Pu and 6-fPu, the DBEAs of Pu (3.7 D) and 6-fPu (4.7 D) are estimated to be 0.050 and 0.090 eV, respectively. Allowing for the estimated dipole binding energy, the  $v=1$  level of the dipole bound 6-fPu anion to appear near an electron impact energy of 0.55 eV which cannot pass through the barrier leading the first peak of 6-fPu does not exist at the electron energy of 0.55 eV. The  $v=2$  level of 6-fPu, Pu and Ad appear at 1.14, 1.17 and 1.22 eV, respectively, at which the first peak of all purines appears. These energies are not close to the  $E_{DEA}$  calculated at G2MP2 which is 0.54, 0.72 and 0.94 eV, respectively, for 6-fPu, Pu and Ad. However, it can distinguish the energy required for losing a neutral H from N9 site between these three purines and provides the same trend as the G2MP2 calculations. This finding agrees well with the experiment (Denifl *et al.*, 2007) observed that the first DEA peak of Pu lies in lower electron energy than that of Ad.

The lower-panels in Figure 42 exhibit the spin density on the departing H9 and the N9 site as the N9-H distance is stretching. As seen for Ad, at shorter distance the spin density is on  $\text{NH}_2$  group. Then, as the internuclear distance increases, the spin density on H9 increases. It increases more rapidly at shorter distance and tends toward a saturated value of 1 beyond 2.5 Å. While the spin density of Pu and 6-fPu locates only in region of the N9-H bond and its neighboring C8-H site. The surface plot of spin density of Ad anion is shown in Figure 43. This is similar for Pu and 6-fPu cases except the absence of spin density on the C6 site. The spin density on H9 shows that the H is departing as a neutral hydrogen atom (with all spin density on it). The remaining fragment is, of course, a closed-shell negative ion.

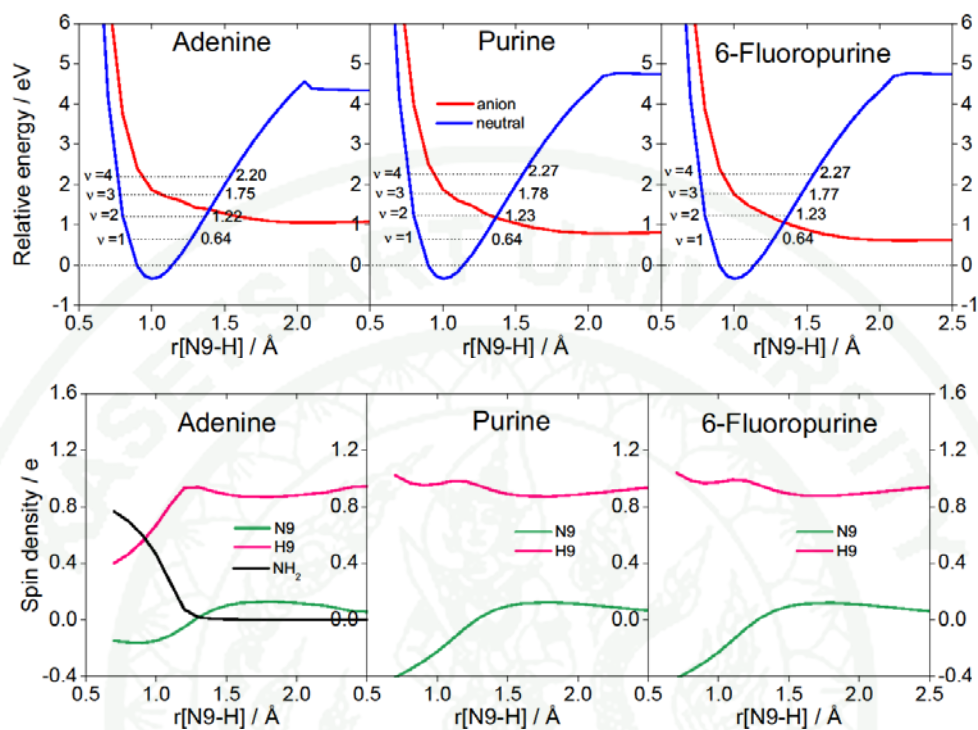


**Figure 42** Upper panel: Adiabatic potential energy curves with zero-point energy (ZPE) correction of ground state of neutral adenine (Ad), purine (Pu) and 6-fluoropurine (6-fPu) molecules (blue line) and their corresponding anions (excess electron in the  $\sigma^*$  MO, red line) obtained from UB3LYP/cc-pVTZ calculations. Lower panel: Spin density of anions.

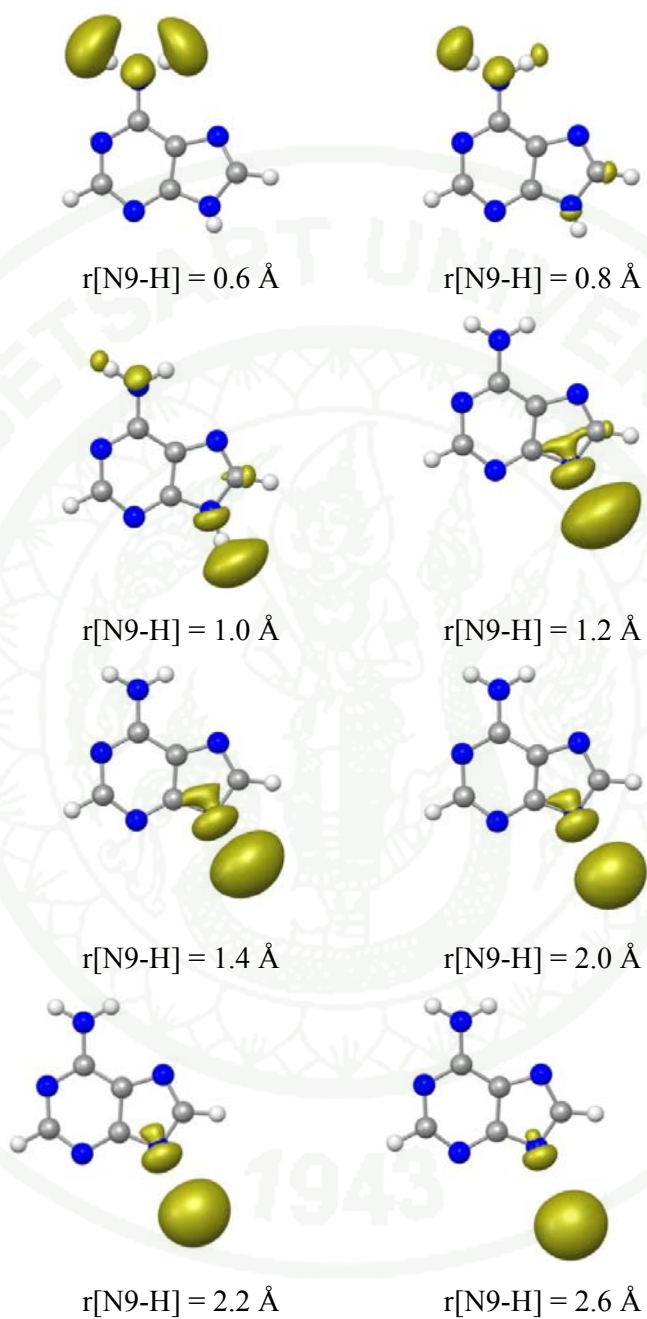


**Figure 43** Spin density surface (isovalue =  $0.004 e/\text{\AA}$ ) of adenine anion obtained from UB3LYP/cc-pVT calculations.

This study theoretically investigates in the details of electron attacking on purine and its derivatives (adenine and 6-fluoropurine) which then causes bond breaking. The results of this dissociative electron attachment (DEA) reaction can be summarized as the followings. An excess electron is trapped to purines via electrostatic (charge-charge) interaction because of a large dipole moment of purines. The corresponding anions are dipole-bound state (DBS) anions. From the calculations, the HOMO wavefunction density of DBS anions is outside the molecular framework leading their structure similar to their corresponding neutral. Due to the charge-charge interaction, DBS anions are expected to be more stable than the neutral in the magnitude of meV. However, the method and basis set used in this study gives the underestimated electron affinity energy of adenine by factor of 10 when compared to experimental value. Then the excess electron trapped in the DBS state tunnels to the antibonding  $\sigma^*$  valence orbitals which then cause the bond breaking. According to the experiment of Denifl (2007), this work concentrates on the N-H/C-H bond breaking giving the dehydrogenated anion and hydrogen atom as products. The G2MP2 calculations show that hydrogen atom at N9 position dissociates most easily and needs the electron energy of 0.54 eV (6-fluoropurine), 0.72 eV (purine), 0.94 eV (adenine) which are in good agreement with experimental values. It is shown that the different electron-energy requirement of similar molecules is due to the different electrical fields of the purines caused by the substituent group at the C6 site. The  $-\text{NH}_2$  group donates electron density into the ring while the electron-withdrawing  $-\text{F}$  does the opposite, facilitating to the attachment of the extra electron. Analyses of electronic properties calculated at UB3LYP/cc-pVTZ level of theory show that there are four main factors to control which N-H/C-H bond dissociation is easier. Electrostatic potential (ESP) reveals that the excess electron prefers to attack purines in the positive ESP regions at which electron density is low. The positive ESPs are around the N9 and C8 region for all purines and at the  $\text{NH}_2$  group of adenine. This phenomenon is considered as site-selective behavior. The energy of virtual  $\sigma^*$  molecular orbitals (MOs) mostly controls the ease of N-H/C-H bond breaking. It is found that the virtual  $\sigma^*$  MOs corresponding to the N-H bond are lower in energy than those of the C-H bond, hence, the N-H bond cleavage is easier than the C-H bond.

Electronegativity of atoms also confirms this. These cause the bond-selectivity of the DEA reaction. In addition, the ease of bond breaking should consider the stability of product dehydrogenated anion which can be explained in the term of electron affinity (EA) of dehydrogenated radical. To address the microscopic mechanism of the dissociation process, especially for the hydrogen loss N9 position, adiabatic neutral and anionic potential energy surfaces along the N9-H bond stretching are calculated at UB3LYP/cc-pVTZ level of theory. The results show that the first peak of DEA spectrum appears at 1.14, 1.17 and 1.22 eV, respective for 6-fPu, Pu and Ad.



## CONCLUSIONS

### **Mechanisms and energetic of the direct benzene-to-phenol conversion on Fe-ZSM-5 zeolite: M06 density functional calculation**

The direct benzene-to-phenol conversion on Fe-ZSM-5 has been studied via M06 functional. All structures were optimized at ONIOM(UM06:UFF) approach and the single point calculation at UM06 were performed to obtain the reliable energies. As the results, the adsorbed benzene is activated by  $\alpha$ -oxygen of the active Fe center via electrophilic substitution yielding the  $\sigma$ -adduct. The activation energy is calculated to be 9.99 kcal/mol. The  $\sigma$ -adduct further transforms into the hydroxo-phenoxo intermediate by either via the proton shuttle of the  $\sigma$ -adduct without barrier energy or via the 1,5-H shift of 2,4-cyclohexadienon with the barrier of 16.59 kcal/mol. 2,4-cyclohexadienon is produced from 1,2-H shift of the  $\sigma$ -adduct with barrierless. Finally, H of the hydroxo ligand of the hydroxo-phenoxo intermediate shifts to O of the phenoxo group to form phenol which is proposed to be a rate-determining step for the total reaction mechanism of benzene-to-phenol conversion when the phenol desorption is taken into account. The activation energy of this step is 45.67 kcal/mol which slightly higher than the phenol desorption energy of 42.14 kcal/mol.

### **Au(I) cation and Au(CN)<sub>2</sub><sup>-</sup> anion in liquid nitromethane: quantum chemical calculations and molecular dynamics simulations**

Energetic and geometric features of various gold(I)-nitromethane clusters, with Au(I) occurring as a free ion and in the Au(CN)<sub>2</sub><sup>-</sup> complex, respectively, were calculated and discussed in the light of the peculiar properties of Au(I). Ab-initio pair energy surfaces for Au<sup>+</sup>-NM, Au(CN)<sub>2</sub><sup>-</sup>-NM, K<sup>+</sup>-NM, K<sup>+</sup>-Au(CN)<sub>2</sub><sup>-</sup> and NM-NM were derived by fitting simple analytical functions to quantum chemically calculated energies. These functions were then used to perform a molecular dynamics simulation of one Au(I) cation in 499 nitromethane molecules for the free Au(I) system and one Au(CN)<sub>2</sub><sup>-</sup> and one K<sup>+</sup> ions in 459 nitromethane for the KAu(CN)<sub>2</sub>. The simulations

were performed in the NVT ensemble at room temperature. A comparative simulation with an older, generic NM-NM potential energy function was also performed for the Au(I)-NM case and gave nearly identical results with respect to the analyzed quantities. The first solvation shell around the free Au(I) cation consists of 9-10 nitromethane molecules with a distance of about 2.6 Å for the first shell to Au<sup>+</sup> about 4.6 Å for the second. The Au(CN)<sub>2</sub><sup>-</sup> anion is surrounded by 15-16 nitromethane molecules in the first solvation shell with a Au-C distance of 4.0 Å and 9.2 Å for the second solvation shell. An X-ray diffraction experiment on a diluted solution of KAu(CN)<sub>2</sub> in nitromethane was performed as well. The resulting RDF agrees well with the one obtained from the molecular dynamics simulation. The results show the especially strong binding between Au and NM in AuNM<sub>2</sub><sup>+</sup>. For higher values of n, the resulting geometries reflect the fact that the NM-NM interaction dominates over Au<sup>+</sup>-NM and Au(CN)<sub>2</sub><sup>-</sup>-NM interactions.

#### **Effect of substituent group on dissociative electron attachment of purines: quantum chemical study**

Dissociative electron attachment (DEA) on purine and its derivatives (adenine and 6-fluoropurine) has been studied by means of quantum chemical calculations. The system loses one hydrogen atom and the stable dehydrogenated anion. The energies required for removing the hydrogen atom from the purine ring are calculated with the G2MP2 extrapolation method. It is found that hydrogen atom at N9 dissociates most easily and needs the electron energy of 0.54 eV (6-fluoropurine), 0.72 eV (purine), 0.94 eV (adenine) which are in good agreement with experimental values. It is shown that the different electron-energy requirement of similar molecules is due to the different electrical fields of the purines caused by the substituent group at the C6 site. The -NH<sub>2</sub> group donates electron density into the ring while the electron-withdrawing -F group does the opposite, facilitating to the attachment of the extra electron. Adiabatic neutral and anionic potential energy surfaces are calculated at UB3LYP/cc-pVTZ level of theory. From these the vibrational energy levels of the N9-H bond stretching vibrations were calculated in order to obtain the energy levels for the dissociation process.

**LITERATURE CITED**

- Abdoul-Carime, H., J. Langer, M.A. Huels and E. Illenberger. 2005. Decomposition of purine nucleobases by very low energy electrons. **Eur. Phys. J. D** 35(2): 399-404.
- \_\_\_\_\_, S. Gohlke and E. Illenberger. 2004. Site-specific dissociation of DNA bases by slow electrons at early stages of irradiation. **Phys. Rev. Lett.** 92(16): 168103.
- \_\_\_\_\_, M.A. Huels, E. Illenberger and L. Sanche. 2003. Formation of negative ions from gas phase halo-uracils by low-energy (0-18 eV) electron impact. **Int. J. Mass Spectrom.** 228(2-3): 703-716.
- \_\_\_\_\_ and L. Sanche. 2002. Fragmentation of short single DNA strands by 1-30 eV electrons: dependence on base identity and sequence. **Int. J. Radiat. Biol.** 78(2): 89-99.
- \_\_\_\_\_, M.A. Huels, E. Illenberger and L. Sanche. 2001. Sensitizing DNA to secondary electron damage: Resonant formation of oxidative radicals from 5-halouracils. **J. Am. Chem. Soc.** 123(22): 5354-5355.
- Aflatooni, K., G.A. Gallup and P.D. Burrow. 1998. Electron attachment energies of the DNA bases. **J. Phys. Chem. A** 102: 6205-6207.
- Anusiewicz, I., M. Sobczyk, J. Berdys-Kochanska, P. Skurski and J. Simons. 2005. A theoretical model for indirect dissociative electron attachment. **J. Phys. Chem. A** 109(3): 484-492.
- Assefa, Z., K. Kalachnikova, R.G. Haire and R.E. Sykora. 2007. Hydrothermal synthesis, structural, Raman, and luminescence studies of  $\text{Am}[\text{M}(\text{CN})_2]_3 \cdot 3\text{H}_2\text{O}$

and  $\text{Nd}[\text{M}(\text{CN})_2]_3 \cdot 3\text{H}_2\text{O}$  ( $\text{M} = \text{Ag}, \text{Au}$ ): Bimetallic coordination polymers containing both trans-plutonium and transition metal elements. **J. Solid State Chem.** 180(11): 3121-3129.

Bassan, A., M.R.A. Blomberg and P.E.M. Siegbahn. 2003. Mechanism of aromatic hydroxylation by an activated  $\text{Fe}(\text{IV})=\text{O}$  core in tetrahydrobiopterin-dependent hydroxylases. **Chem. A Eur. J.** 9(17): 4055-4067.

Boekfa, B., S. Choomwattana, P. Khongpracha and J. Limtrakul. 2009. Effects of the zeolite framework on the adsorptions and hydrogen-exchange reactions of unsaturated aliphatic, aromatic, and heterocyclic compounds in ZSM-5 zeolite: A combination of perturbation theory (MP2) and a newly developed density functional theory (M06-2X) in ONIOM scheme. **Langmuir** 25(22): 12990-12999.

Boudaiffa, B., P. Cloutier, D. Hunting, M.A. Huels and L. Sanche. 2002. Cross sections for low-energy (10-50 eV) electron damage to DNA. **Radiat. Res.** 157(3): 227-234.

\_\_\_\_\_, \_\_\_\_\_, \_\_\_\_\_, \_\_\_\_\_ and \_\_\_\_\_. 2000a. Low-energy electrons induced DNA strand breaks. **M S-Med. Sci.** 16(11): 1281-1283.

\_\_\_\_\_, \_\_\_\_\_, \_\_\_\_\_, \_\_\_\_\_ and \_\_\_\_\_. 2000b. Resonant formation of DNA strand breaks by low-energy (3 to 20 eV) electrons. **Science** 287(5458): 1658-1660.

- Bryce, R.A., J.M. Charnock, R.A.D. Patrick and A.R. Lennie. 2003. EXAFS and density functional study of gold(I) thiosulfate complex in aqueous solution. **J. Phys. Chem. A** 107(14): 2516-2523.
- Burch, R. and C. Howitt. 1992. Direct partial oxidation of benzene to phenol on zeolite catalysts. **Appl. Catal. A-Gen.** 86: 139-146.
- Burrow, P.D., G.A. Gallup, A.M. Scheer, S. Denifl, S. Ptasinska, T. Mark and P. Scheier. 2006. Vibrational feshbach resonances in uracil and thymine. **J. Chem. Phys.** 124(12): 124310.
- Carpenter, J.E. and F. Weinhold. 1988. Analysis of the geometry of the hydroxymethyl radical by the different hybrids for different spins natural bond orbital procedure. **J. Mol. Struct.-Theochem** 169: 41-62.
- Chen, H.Y., E.M. El-Malki, X. Wang, R.A. van Santen and W.M.H. Sachtler. 2000. Identification of active sites and adsorption complexes in Fe/MFI catalysts for NO<sub>x</sub> reduction. **J. Mol. Catal. A-Chem.** 162(1-2): 159-174.
- Choi, S.H., B.R. Wood, A.T. Bell, M.T. Janicke and K.C. Ott. 2004. X-ray absorption fine structure analysis of the local environment of Fe in Fe/Al-MFI. **J. Phys. Chem. B** 108(26): 8970-8975.
- \_\_\_\_\_, \_\_\_\_\_, J.A. Ryder and A.T. Bell. 2003. X-ray absorption fine structure characterization of the local structure of Fe in Fe-ZSM-5. **J. Phys. Chem. B** 107(43): 11843-11851.
- Cimatu, K. and S. Baldelli. 2008. Chemical imaging of corrosion: Sum frequency generation imaging microscopy of cyanide on gold at the solid-liquid interface. **J. Am. Chem. Soc.** 130(25): 8030-8037.

- Cui, J.R. and L.F. Zhang. 2008. Metallurgical recovery of metals from electronic waste: A review. **J. Hazard. Mater.** 158(2-3): 228-256.
- Curtiss, L.A., K. Raghavachari and J.A. Pople. 1993. Gaussian-2 theory using reduced Moeller-Plesset orders. **J. Chem. Phys.** 98: 1293.
- Dalleska, N.F., B.L. Tjelta and P.B. Armentrout. 1994. Sequential Bond Energies of Water to  $\text{Na}^+$  (3s0),  $\text{Mg}^+$  (3s1), and  $\text{Al}^+$  (3s2). **J. Phys. Chem.** 98(15):4191–4195.
- de Visser, S. P., K. Oh, A.R. Han and W. Nam. 2007. Combined experimental and theoretical study on aromatic hydroxylation by mononuclear nonheme iron(IV)-oxo complexes. **Inorg. Chem.** 46: 4632-4641.
- \_\_\_\_\_ and S. Shaik. 2003. A proton-shuttle mechanism mediated by the porphyrin in benzene hydroxylation by cytochrome P450 enzymes. **J. Am. Chem. Soc.** 125: 7413-7427.
- Denifl, S., F. Zappa, A. Mauracher, F.F. da Silva, A. Bacher, O. Echt, T.D. Mark, D.K. Bohme and P. Scheier. 2008. Dissociative electron attachment to DNA bases near absolute zero temperature: Freezing dissociation intermediates. **Chemphyschem** 9(10): 1387-1389.
- \_\_\_\_\_, P. Sulzer, D. Huber, F. Zappa, M. Probst, T.D. Mark, P. Scheier, N. Injan, J. Limtrakul, R. Abouaf and H. Dunet. 2007. Influence of functional groups on the site-selective dissociation of adenine upon low-energy electron attachment. **Angew. Chem.-Int. Ed.** 46(27): 5238-5241.
- \_\_\_\_\_, S. Ptasinska, G. Hanel, B. Gstir, M. Probst, P. Scheier and T.D. Mark. 2004a. Electron attachment to gas-phase uracil. **J. Chem. Phys.** 120(14): 6557-6565.

- \_\_\_\_\_, \_\_\_\_\_, M. Probst, J. Hrusak, P. Scheier and T.D. Mark. 2004b. Electron attachment to the gas-phase DNA bases cytosine and thymine. **J. Phys. Chem. A** 108(31): 6562-6569.
- \_\_\_\_\_, B. Sonnweber, G. Hanel, P. Scheier and T.D. Mark. 2004c. Threshold electron impact ionization studies of uracil. **Int. J. Mass Spectrom.** 238(1): 47-53.
- \_\_\_\_\_, S. Matejcik, B. Gstir, G. Hanel, M. Probst, P. Scheier and T.D. Mark. 2003a. Electron attachment to 5-chloro uracil. **J. Chem. Phys.** 118(9): 4107-4114.
- \_\_\_\_\_, S. Ptasinska, M. Cingel, S. Matejcik, P. Scheier and T.D. Mark. 2003b. Electron attachment to the DNA bases thymine and cytosine. **Chem. Phys. Lett.** 377(1-2): 74-80.
- Desfrancois, C., H. Abdoul-Carime and J.P. Schermann. 1996. Electron attachment to isolated nucleic acid bases. **J. Chem. Phys.** 104(19): 7792-7794.
- Deutsch, H., K. Becker, P. Defrance, U. Onthong, M. Probst, S. Matt, P. Scheier and T.D. Mark. 2003a. Calculated absolute cross section for the electron-impact ionisation of simple molecular ions. **Int. J. Mass Spectrom.** 223(1-3): 639-646.
- \_\_\_\_\_, P. Scheier, K. Becker and T.D. Mark. 2003b. Calculated cross-sections for the electron-impact detachment from negative ions using the Deutsch-Mark (DM) formalism. **Chem. Phys. Lett.** 382(1-2): 26-31.
- \_\_\_\_\_, \_\_\_\_\_, \_\_\_\_\_ and \_\_\_\_\_. 2003c. Calculations of partial electron-impact cross sections for the multiple ionization of fullerenes using a semi-empirical method. **Int. J. Mass Spectrom.** 223(1-3): 253-261.

- Dubkov, K.A., V.I. Sobolev, E.P. Talsi, M.A. Rodkin, N.H. Watkins, A.A. Shteinman and G.I. Panov. 1997. Kinetic isotope effects and mechanism of biomimetic oxidation of methane and benzene on FeZSM-5 zeolite. **J. Mol. Catal. A-Chem.** 123(2-3): 155-161.
- Evangelista, F.A., A. Paul and H.F. Schaefer. 2004. Radicals derived from adenine: Prediction of large electron affinities with a considerable spread. **J. Phys. Chem. A** 108(16): 3565-3571.
- Farges, F., J.A. Sharps and G.E. Brown. 1993. Local environment around gold(III) in aqueous chloride solutions - an EXAFS spectroscopy study. **Geochim. Cosmochim. Acta** 57(6): 1243-1252.
- Fellah, M.F., R.A. van Santen and I. Onal. 2009. Oxidation of benzene to phenol by N<sub>2</sub>O on an Fe<sup>2+</sup>-ZSM-5 cluster: A density functional theory study. **J. Phys. Chem. C** 113(34): 15307-15313.
- Feuerbacher, S., T. Sommerfeld and L.S. Cederbaum. 2004. Extrapolating bound state data of anions into the metastable domain. **J. Chem. Phys.** 121(14): 6628-6633.
- Fiegele, T., V. Grill, S. Matt, M. Lezius, G. Hanel, M. Probst, P. Scheier, K. Becker, H. Deutsch, O. Echt, A. Stamatovic and T.D. Mark. 2001. Electron and ion high-resolution interaction studies using sector field mass spectrometry: propane a case study. **Vacuum** 63(4): 561-569.
- Flosadottir, H.D., S. Denifl, F. Zappa, N. Wendt, A. Mauracher, A. Bacher, H. Jonsson, T.D. Mark, P. Scheier and O. Ingolfsson. 2007. Combined experimental and theoretical study on the nature and the metastable decay pathways of the amino acid ion fragment [M-H]. **Angew. Chem.-Int. Ed.** 46(42): 8057-8059.

Frisch, M.J., G.W. Trucks, H.B. Schlegel, G.E. Scuseria, M.A. Robb, J.R. Cheeseman, J.A. Montgomery Jr., T. Vreven, K.N. Kudin, J.C. Burant, J.M. Millam, S.S. Iyengar, J. Tomasi, V. Barone, B. Mennucci, M. Cossi, G. Scalmani, N. Rega, G.A. Petersson, H. Nakatsuji, M. Hada, M. Ehara, K. Toyota, R. Fukuda, J. Hasegawa, M. Ishida, T. Nakajima, Y. Honda, O. Kitao, H. Nakai, M. Klene, X. Li, J.E. Knox, H.P. Hratchian, J.B. Cross, V. Bakken, C. Adamo, J. Jaramillo, R. Gomperts, R.E. Stratmann, O. Yazyev, A.J. Austin, R. Cammi, C. Pomelli, J.W. Ochterski, P.Y. Ayala, K. Morokuma, G.A. Voth, P. Salvador, J.J. Dannenberg, V.G. Zakrzewski, S. Dapprich, A.D. Daniels, M.C. Strain, O. Farkas, D.K. Malick, A.D. Rabuck, K. Raghavachari, J.B. Foresman, J.V. Ortiz, Q. Cui, A.G. Baboul, S. Clifford, J. Cioslowski, B.B. Stefanov, G. Liu, A. Liashenko, P. Piskorz, I. Komaromi, R.L. Martin, D.J. Fox, T. Keith, M.A. Al-Laham, C.Y. Peng, A. Nanayakkara, M. Challacombe, P.M.W. Gill, B. Johnson, W. Chen, M.W. Wong, C. Gonzalez and J.A. Pople. 2004. **Gaussian Inc., Wallingford CT**

Gluch, K., S. Matt-Leubner, L. Michalak, O. Echt, A. Stamatovic, P. Scheier and T.D. Mark. 2004. High resolution measurements of kinetic energy release distributions of neon, argon, and krypton cluster ions using a three sector field mass spectrometer. **J. Chem. Phys.** 120(6): 2686-2692.

Gomez, I., E. Rodriguez and M. Reguero. 2006. New insights into the interconversion mechanism between phenol and its isomers. **J. Mol. Struct.-Theochem** 767(1-3): 11-18.

Gräfenstein, J., E. Kraka, M. Filatov and D. Cremer. 2002. Can unrestricted density-functional theory describe open shell singlet biradicals? **Int. J. Mol. Sci.** 3: 360-394.

- Groves, J.T., R.C. Haushalter, M. Nakamura, T.E. Nemo and B.J. Evans. 1981. High-valent iron-porphyrin complexes related to peroxidase and cytochrome-P-450. **J. Am. Chem. Soc.** 103(10): 2884-2886.
- Gu, J.D., Y.M. Xie and H.F. Schaefer. 2007. Electron attachment to DNA single strands: gas phase and aqueous solution. **Nucleic Acids Res.** 35(15): 5165-5172.
- Guo, Y., Z.Q. Liu, B. Zhao, Y.H. Feng, G.F. Xu, S.P. Yan, P. Cheng, Q.L. Wang and D.Z. Liao. 2009. Two  $[\text{Au}(\text{CN})_2]^-$ -bridged heterometallic coordination polymers directed by different 2,2'-bipyridyl-like ligands. **Crystengcomm** 11(1): 61-66.
- Gutowski, M., K.D. Jordan and P. Skurski. 1998. Electronic structure of dipole-bound anions. **J. Phys. Chem. A** 102(15): 2624-2633.
- Hay, P.J. and W.R. Wadt. 1985. Ab initio effective core potentials for molecular calculations potentials for K to Au including the outermost core orbitals. **J. Chem. Phys.** 82(1): 299-310.
- Hendricks, J.H., S.A. Lyapustina, H.L. de Clercq and K.H. Bowen. 1998. The dipole bound-to-covalent anion transformation in uracil. **J. Chem. Phys.** 108(1): 8-11.
- Hensen, E.J.M., Q. Zhu, M. Hendrix, A.R. Overweg, P.J. Kooyman, M.V. Sychev and R.A. van Santen. 2004. Effect of high-temperature treatment on Fe/ZSM-5 prepared by chemical vapor deposition of  $\text{FeCl}_3$  I: Physicochemical characterization. **J. Catal.** 221: 560-574.

- \_\_\_\_\_, \_\_\_\_\_ and R.A. van Santen. 2003. Extraframework Fe-Al-O species occluded in MFI zeolite as the active species in the oxidation of benzene to phenol with nitrous oxide **J. Catal.** 220: 260-264.
- Huber, D., M. Beikircher, S. Denifl, F. Zappa, S. Matejcek, A. Bacher, V. Grill, T.D. Mark and P. Scheier. 2006. High resolution dissociative electron attachment to gas phase adenine. **J. Chem. Phys.** 125(8): 084304.
- Hunig, I., C. Plutzer, K.A. Seefeld, D. Lowenich, M. Nispel and K. Kleinermanns. 2004. Photostability of isolated and paired nucleobases: N-H dissociation of adenine and hydrogen transfer in its base pairs examined by laser spectroscopy. **Chemphyschem** 5(9): 1427-1431.
- Iino, T., K. Ohashi, K. Inoue, K. Judai, N. Nishi and H. Sekiya. 2007. Infrared spectroscopy of  $\text{Cu}^+(\text{H}_2\text{O})_n$  and  $\text{Ag}^+(\text{H}_2\text{O})_n$ : Coordination and solvation of noble-metal ions. **J. Chem. Phys.** 126(19): 194302.
- Ivanov, A.A., V.S. Chernyavsky, M.J. Gross, A.S. Kharitonov, A.K. Uriarte and G.I. Panov. 2003. Kinetics of benzene to phenol oxidation over Fe-ZSM-5 catalyst. **Appl. Catal. A-Gen.** 249(2): 327-343.
- Jalbout, A.F. and L. Adamowicz. 2001a. Dipole-bound anions of adenine-water clusters. Ab initio study. **J. Phys. Chem. A** 105(6): 1033-1038.
- \_\_\_\_\_ and \_\_\_\_\_. 2001b. Dipole-bound anions to adenine-imidazole complex. Ab initio study. **J. Phys. Chem. A** 105(6): 1071-1073.
- Kachurovskaya, N. A. 2004. Computational study of benzene-to-phenol oxidation catalyzed by  $\text{N}_2\text{O}$  on iron-exchanged ferrierite **J. Phys. Chem. B** 108: 5944-5950.

- \_\_\_\_\_, G.M. Zhidomirov, E.J.M. Hensen and R.A. van Santen. 2003. Cluster model DFT study of the intermediates of benzene to phenol oxidation by N<sub>2</sub>O on FeZSM-5 zeolites **Catal. Lett.** 86(1-3): 25-31.
- Kalcher, J. 2001. Paradigms of dipole-bound negative ion states in diatomics with high spin multiplicity. **Croat. Chem. Acta** 74: 903.
- Kasuriya, S., S. Namuangruk, P. Treesukol, M. Tirtowidjojo and J. Limtrakul. 2003. Adsorption of ethylene, benzene, and ethylbenzene over faujasite zeolites investigated by the ONIOM method. **J. Catal.** 219(2): 320-328.
- Kharitonov, A.S., G.A. Sheveleva, G.I. Panov, V.I. Sobolev, Y.A. Paukshtis and V.N. Romannikov. 1993. Ferrisilicate analogs of ZSM-5 zeolite as catalysts for one-step oxidation of benzene to phenol. **Appl. Catal. A-Gen.** 98: 33-43.
- Kubanek, P., B. Wichterlova and Z. Sobalik. 2002. Nature of active sites in the oxidation of benzene to phenol with N<sub>2</sub>O over H-ZSM-5 with low Fe concentrations. **J. Catal.** 211: 109-118.
- Kumar, A. and M.D. Sevilla. 2008. The role of  $\pi$ - $\sigma^*$  excited states in electron-induced DNA strand break formation: A time-dependent density functional theory study. **J. Am. Chem. Soc.** 130(7): 2130-2131.
- Kumsapaya, C., K. Bobuatong, P. Khongpracha, Y. Tantirungrotechai and J. Limtrakul. 2009. Mechanistic investigation on 1,5-to 2,6-dimethylnaphthalene isomerization catalyzed by acidic beta zeolite: ONIOM study with an M06-L functional. **J. Phys. Chem. C** 113(36): 16128-16137

- Lee, H.M., M. Diefenbach, S.B. Suh, P. Tarakeshwar and K.S. Kim. 2005. Why the hydration energy of  $\text{Au}^+$  is larger for the second water molecule than the first one: Skewed orbitals overlap. **J. Chem. Phys.** 123(7): 074328.
- Li, X.F., L. Sanche and M.D. Sevilla. 2004. Low energy electron interactions with uracil: The energetics predicted by theory. **J. Phys. Chem. B** 108(17): 5472-5476.
- \_\_\_\_\_, M.D. Sevilla and L. Sanche. 2003. Density functional theory studies of electron interaction with DNA: Can zero eV electrons induce strand breaks? **J. Am. Chem. Soc.** 125(45): 13668-13669.
- Li, X., Z. Cai and M.D. Sevilla. 2002. DFT calculations of the electron affinities of nucleic acid bases: dealing with negative electron affinities. **J. Phys. Chem. A** 106: 1596-1603.
- Limtrakul, J., T. Nanok, S. Jungsuttiwong, P. Khongpracha and T.N. Truong. 2001. Adsorption of unsaturated hydrocarbons on zeolites: the effects of the zeolite framework on adsorption properties of ethylene. **Chem. Phys. Lett.** 349(1-2): 161-166.
- Martin, F., P.D. Burrow, Z.L. Cai, P. Cloutier, D. Hunting and L. Sanche. 2004. DNA strand breaks induced by 0-4 eV electrons: The role of shape resonances. **Phys. Rev. Lett.** 93(6): 068101.
- Megyes, T., S. Balint, T. Grosz, T. Radnai, I. Bako and L. Almasy. 2007. Structure of liquid nitromethane: Comparison of simulation and diffraction studies. **J. Chem. Phys.** 126(16): 164507.

- Morgan, L.A., J. Tennyson and C.J. Gillan. 1998. The UK molecular R-matrix codes. **Comput. Phys. Commun.** 114: 120.
- Namuangruk, S., P. Pantu and J. Limtrakul. 2004. Alkylation of benzene with ethylene over faujasite zeolite investigated by the ONIOM method. **J. Catal.** 225(2): 523-530.
- Nestmann, B. and S.D. Peyerimhoff. 1985. Calculation of the discrete component of resonance states in negative ions by variation of nuclear charges. **J. Phys. B: At. Mol. Phys.** 18: 615-626.
- Nilsson, K.B., I. Persson and V.G. Kessler. 2006. Coordination chemistry of the solvated  $\text{Ag}^{\text{I}}$  and  $\text{Au}^{\text{I}}$  ions in liquid and aqueous ammonia, trialkyl and triphenyl phosphite, and tri-n-butylphosphine solutions. **Inorg. Chem.** 45(17):6912-6921.
- Ohashi, K., K. Inoue, T. Iino, J. Sasaki, K. Judai, N. Nishi and H. Sekiya. 2009. A molecular picture of metal ion solvation: Infrared spectroscopy of  $\text{Cu}+(\text{NH}_3)(n)$  and  $\text{Ag}+(\text{NH}_3)(n)$  in the gas phase. **J. Mol. Liq.** 147(1-2):71-76.
- Onthong, U., T. Megyes, I. Bako, T. Radnai, T. Grosz, K. Hermansson and M. Probst. 2004. X-ray and neutron diffraction studies and molecular dynamics simulations of liquid DMSO. **Phys. Chem. Chem. Phys.** 6(9): 2136-2144.
- Pabchanda, S., P. Pantu and J. Limtrakul. 2005. Hydrolysis of methoxide species and regeneration of active site in Fe-ZSM-5 catalyst by the ONIOM method. **J. Mol. Catal. A-Chem.** 239(1-2): 103-110.

- Panajotovic, R., M. Michaud and L. Sanche. 2007. Cross sections for low-energy electron scattering from adenine in the condensed phase. **Phys. Chem. Chem. Phys.** 9(1): 138-148.
- Panjan, W. and J. Limtrakul. 2003. The influence of the framework on adsorption properties of ethylene/H-ZSM-5 system: an ONIOM study. **J. Mol. Struct.** 654(1-3): 35-45.
- Panov, G.I., A.K. Uriarte, M.A. Rodkin and V.I. Sobolev. 1998. Generation of active oxygen species on solid surfaces. Opportunity for novel oxidation technologies over zeolites. **Catal. Today** 41(4): 365-385.
- \_\_\_\_\_, A.S. Kharitonov and V.I. Sobolev. 1993. Oxidative hydroxylation using dinitrogen monoxide: a possible route for organic synthesis over zeolites **Appl. Catal. A-Gen.** 98: 1-20.
- \_\_\_\_\_, G.A. Sheveleva, A.S. Kharitonov, V.N. Romannikov and L.A. Vostrikova. 1992. Oxidation of benzene to phenol by nitrous-oxide over Fe-ZSM-5 zeolites **Appl. Catal. A-Gen.** 82: 31-36.
- \_\_\_\_\_, V.I. Sobolev and A.S. Kharitonov. 1990. The Role of iron in N<sub>2</sub>O decomposition on ZSM-5 zeolite and reactivity of the surface oxygen formed. **J. Mol. Catal.** 61(1): 85-97.
- Pantu, P., S. Pabchanda and J. Limtrakul. 2004. Theoretical investigation of the selective oxidation of methane to methanol on nanostructured Fe-ZSM-5 by the ONIOM method. **Chemphyschem** 5(12): 1901-1906.

- Park, Y.S., H. Cho, L. Parenteau, A.D. Bass and L. Sanche. 2006. Cross sections for electron trapping by DNA and its component subunits I: Condensed tetrahydrofuran deposited on Kr. **J. Chem. Phys.** 125(7): 074714.
- Ptasinska, S., S. Denifl, V. Grill, T.D. Mark, E. Illenberger and P. Scheier. 2005a. Bond- and site-selective loss of H- from pyrimidine bases. **Phys. Rev. Lett.** 95(9): 093201.
- \_\_\_\_\_, \_\_\_\_\_, \_\_\_\_\_, \_\_\_\_\_, P. Scheier, S. Gohlke, M.A. Huels and E. Illenberger. 2005b. Bond-selective H<sup>-</sup> ion abstraction from thymine. **Angew. Chem.-Int. Ed.** 44(11): 1647-1650.
- \_\_\_\_\_, \_\_\_\_\_, B. Mroz, M. Probst, V. Grill, E. Illenberger, P. Scheier and T.D. Mark. 2005c. Bond selective dissociative electron attachment to thymine. **J. Chem. Phys.** 123(12): 124302.
- \_\_\_\_\_, \_\_\_\_\_, P. Scheier, E. Illenberger and T.D. Mark. 2005d. Bond- and site-selective loss of H atoms from nucleobases by very-low-energy electrons (< 3 eV). **Angew. Chem.-Int. Ed.** 44(42): 6941-6943.
- Pyykko, P. 2005. Theoretical chemistry of gold. II. **Inorg. Chim. Acta** 358(14): 4113-4130.
- \_\_\_\_\_. 2004a. Gold, relativity and nanosized systems. **Gold Bull.** 37(1-2): 136-136.
- \_\_\_\_\_. 2004b. Theoretical chemistry of gold. **Angew. Chem. Int. Ed.** 43(34): 4412-4456.
- Reveles, J.U., P. Calaminici, M.R. Beltran, A.M. Koster and S.N. Khanna. 2007. H<sub>2</sub>O nucleation around Au<sup>+</sup>. **J. Am. Chem. Soc.** 129(50): 15565-15571.

- Rienstra-Kiracofe, J.C., G.S. Tschumper, H.F. Schaefer, S. Nandi and G.B. Ellison. 2002. Atomic and molecular electron affinities: Photoelectron experiments and theoretical computations. **Chem. Rev.** 102(1): 231-282.
- Rosi, M. and C.W. Bauschlicher. 1990. The binding-energies of one and 2 water-molecules to the 1st transition-row metal positive-ions: 2. **J. Chem. Phys.** 92(3):1876-1878.
- \_\_\_\_\_ and \_\_\_\_\_. 1989. The binding-energies of one and 2 water-molecules to the 1st transition-row metal positive-ions. **J. Chem. Phys.** 90(12): 7264-7272.
- Rungsirisakun, R., B. Jansang, P. Pantu and J. Limtrakul. 2005. The adsorption of benzene on industrially important nanostructured catalysts (H-BEA, H-ZSM-5, and H-FAU): confinement effects. **J. Mol. Struct.** 733(1-3): 239-246.
- Ryder, J. A., A.K. Chakraborty and A.T. Bell. 2003. Density functional theory study of benzene oxidation over Fe-ZSM-5 **J. Catal.** 220: 84-91.
- \_\_\_\_\_, \_\_\_\_\_ and \_\_\_\_\_. 2002. Density functional theory study of nitrous oxide decomposition over Fe- and Co-ZSM-5. **J. Phys. Chem. B** 106(28): 7059-7064.
- Sanche, L. 2005. Low energy electron-driven damage in biomolecules. **Eur. Phys. J. D** 35(2): 367-390.
- \_\_\_\_\_. 2003. Low-energy electron damage to DNA and its basic constituents. **Phys. Scr.** 68(5): C108-C112.
- \_\_\_\_\_. 2002a. Mechanisms of low energy electron damage to condensed biomolecules and DNA. **Radiat. Prot. Dosim.** 99(1-4): 57-62.

- \_\_\_\_\_. 2002b. Nanoscopic aspects of radiobiological damage: Fragmentation induced by secondary low-energy electrons. **Mass Spectrom. Rev.** 21(5): 349-369.
- Scheer, A.M., K. Aflatooni, G.A. Gallup and P.D. Burrow. 2004. Bond breaking and temporary anion states in uracil and halouracils: Implications for the DNA bases. **Phys. Rev. Lett.** 92(6): 068102.
- Scheier, P., H. Deutsch, K. Becker and T.D. Mark. 2004. Calculations of electron-impact cross sections for the fragmentation and dissociative ionization of fullerenes using a semi-empirical method. **Int. J. Mass Spectrom.** 233(1-3): 293-298.
- Schiedt, J., R. Weinkauff, D.M. Neumark and E.W. Schlag. 1998. Anion spectroscopy of uracil, thymine and the amino-oxo and amino-hydroxy tautomers of cytosine and their water clusters. **Chem. Phys.** 239(1-3): 511-524.
- Schmidbaur, H., S. Cronje, B. Djordjevic and O. Schuster. 2005. Understanding gold chemistry through relativity. **Chem. Phys.** 311(1-2): 151-161.
- Shafranyosh, II, M.I. Sukhoviya and M.I. Shafranyosh. 2006. Absolute cross sections of positive- and negative-ion production in electron collision with cytosine molecules. **J. Phys. B- At. Mol. Opt. Phys.** 39(20): 4155-4162.
- Shiota, Y., K. Suzuki and K. Yoshizawa. 2006. QM/MM study on the catalytic mechanism of benzene hydroxylation over Fe-ZSM-5. **Organometallics** 25(13): 3118-3123.
- \_\_\_\_\_, \_\_\_\_\_ and \_\_\_\_\_. 2005. Mechanism for the direct oxidation of benzene to phenol by  $\text{FeO}^+$ . **Organometallics** 24(14): 3532-3538.

- Simons, J. 2007. How Very Low-Energy (0.1-2 eV) Electrons Cause DNA Strand Breaks. **Adv. Quantum Chem.** 52: 171-188.
- \_\_\_\_\_. 2006. How do low-energy (0.1-2 eV) electrons cause DNA-strand breaks? **Acc. Chem. Res.** 39(10): 772-779.
- Skurski, P., M. Gutowski and J. Simons. 2000. How to choose a one-electron basis set to reliably describe a dipole-bound anion. **Int. J. Quantum Chem.** 80(4-5): 1024-1038.
- Sobolev, V.I., K.A. Dubkov, O.V. Panna and G.I. Panov. 1995. Selective Oxidation of Methane to Methanol on a FeZSM-5 Surface. **Catal. Today** 24(3):251-252.
- \_\_\_\_\_, G.I. Panov, A.S. Kharitonov, V.N. Romannikov, A.M. Volodin and K.G. Ione. 1993. Catalytic properties of ZSM-5 Zeolites in N<sub>2</sub>O decomposition - the role of iron. **J. Catal.** 139(2):435-443.
- Sommerfeld, T. 2005. Dipole-bound states as doorways in dissociative electron attachment. **J. Phys.: Confer. Ser.** 4: 245-250.
- \_\_\_\_\_. 2004. Intramolecular electron transfer from dipole-bound to valence orbitals: Uracil and 5-chlorouracil. **J. Phys. Chem. A** 108(42): 9150-9154.
- Sorescu, D.C., B.M. Rice and D.L. Thompson. 2001. Molecular dynamics simulations of liquid nitromethane. **J. Phys. Chem. A** 105(41): 9336-9346.
- \_\_\_\_\_, \_\_\_\_\_ and \_\_\_\_\_. 2000. Theoretical studies of solid nitromethane. **J. Phys. Chem. B** 104(35): 8406-8419.

\_\_\_\_\_, \_\_\_\_\_ and \_\_\_\_\_. 1999. Molecular packing and molecular dynamics study of the transferability of a generalized nitramine intermolecular potential to non-nitramine crystals. **J. Phys. Chem. A** 103(8): 989-998.

\_\_\_\_\_, \_\_\_\_\_ and \_\_\_\_\_. 1998. A transferable intermolecular potential for nitramine crystals. **J. Phys. Chem. A** 102(43): 8386-8392.

\_\_\_\_\_, \_\_\_\_\_ and \_\_\_\_\_. 1997. Intermolecular potential for the hexahydro-1,3,5-trinitro-1,3,5-s-triazine crystal (RDX): A crystal packing, Monte Carlo, and molecular dynamics study. **J. Phys. Chem. B** 101(5): 798-808.

Starokon, E.V., K.A. Dubkov, L.V. Pirutko and G.I. Panov. 2003. Mechanisms of iron activation on Fe-containing zeolites and the charge of alpha-oxygen **Top. Catal.** 23: 137-143.

Stepanian, S.G., A.F. Jalbout, C.S. Hall and L. Adamowicz. 2003. Uracil-adenine dimer connected by an excess electron. **J. Phys. Chem. A** 107(39): 7911-7914.

Sun, K., H. Xia, Z. Feng, R.A. van Santen, E. Hensen and C.Li. 2008. Active sites in Fe/ZSM-5 for nitrous oxide decomposition and benzene hydroxylation with nitrous oxide **J. Catal.** 254: 383-396.

Svozil, D., T. Frigato, Z. Havlas and P. Jungwirth. 2005. *Ab initio* electronic structure of thymine anions. **Phys. Chem. Chem. Phys.** 7: 840-845.

Swiderek, P. 2006. Fundamental processes in radiation damage of DNA. **Angew. Chem.-Int. Ed.** 45: 4056-4059.

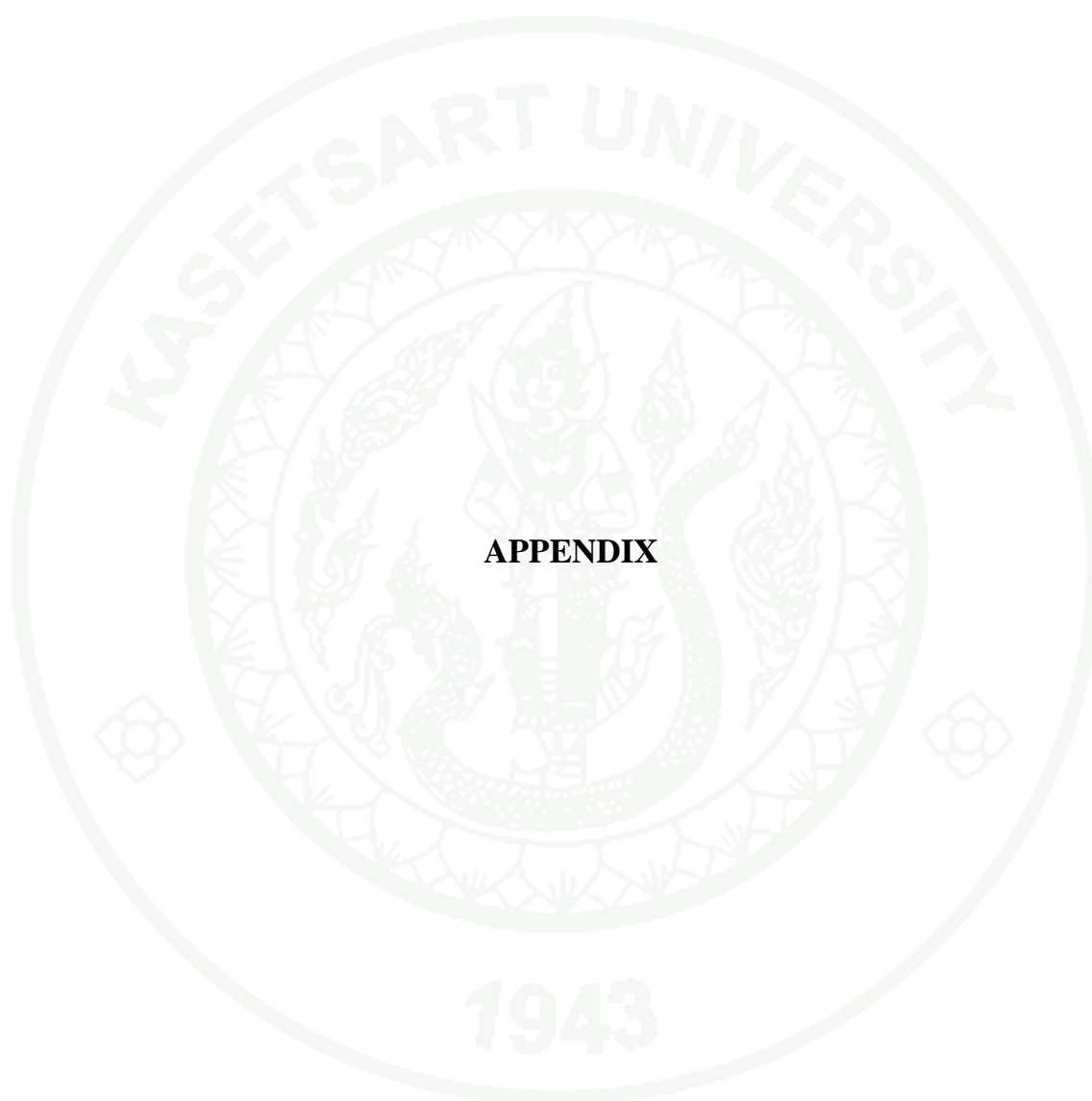
- Theodore, M., M. Sobczyk and J. Simons. 2006. Cleavage of thymine N3-H bonds by low-energy electrons attached to base  $\pi^*$  orbitals. **Chem. Phys.** 329(1-3): 139-147.
- Wesolowski, S.S., M.L. Leininger, P.N. Pentchev and H.F. Schaefer. 2001. Electron affinities of the DNA and RNA bases. **J. Am. Chem. Soc.** 123(17): 4023-4028.
- Whitehead, A., R. Barrios and J. Simons. 2002. Stabilization calculation of the energy and lifetime of metastable  $\text{SO}_4^{2-}$ . **J. Chem. Phys.** 116(7): 2848-2851.
- Wong, M.W. 1996. Vibrational frequency prediction using density functional theory. **Chem. Phys. Lett.** 256(4-5): 391-399.
- Yoshizawa, K., Y. Shiota and T. Kamachi. 2003. Mechanistic proposals for direct benzene hydroxylation over Fe-ZSM-5 zeolite. **J. Phys. Chem. B** 107(41): 11404-11410.
- \_\_\_\_\_, \_\_\_\_\_, Y. Kagawa and T. Yamabe. 2000a. Femtosecond dynamics of the methane-methanol and benzene-phenol conversions by an iron-oxo species. **J. Phys. Chem. A** 104(12): 2552-2561.
- \_\_\_\_\_, \_\_\_\_\_, T. Yumura and T. Yamabe. 2000b. Direct methane-methanol and benzene-phenol conversions on Fe-ZSM-5 zeolite: Theoretical predictions on the reaction pathways and energetics. **J. Phys. Chem. B** 104(4): 734-740.
- \_\_\_\_\_, \_\_\_\_\_ and T. Yamabe. 1999. Reaction pathway for the direct benzene hydroxylation by iron-oxo species. **J. Am. Chem. Soc.** 121(1): 147-153.

\_\_\_\_\_, \_\_\_\_\_ and \_\_\_\_\_. 1998. Methane-methanol conversion by  $\text{MnO}^+$ ,  $\text{FeO}^+$ , and  $\text{CoO}^+$ : A theoretical study of catalytic selectivity. **J. Am. Chem. Soc.** 120(3): 564-572.

Zhao, Y. and D.G. Truhlar. 2008a. Benchmark data for interactions in zeolite model complexes and their use for assessment and validation of electronic structure methods. **J. Phys. Chem. C** 112(17): 6860-6868.

\_\_\_\_\_ and \_\_\_\_\_. 2008b. Density functionals with broad applicability in chemistry. **Acc. Chem. Res.** 41(2): 157-167.

Zierhut, M., W. Roth and I. Fischer. 2004. Dynamics of H-atom loss in adenine. **Phys. Chem. Chem. Phys.** 6: 5178-5183.



**APPENDIX**

Dissociative electron attachment is one type of electron-molecule reaction. In the following, a brief overview of the various kinds of such reactions together with the basic concept of the quantum chemical techniques required for these systems is given.

**“Classical” Anions** are negatively charged molecules with one or more additional electrons occupying the lowest unoccupied molecular orbitals of the ground state (LUMOs) of a formerly neutral molecule with a positive electron affinity. They are also called valence anions. One can argue that despite being classical 'textbook' anions they are in some sense a minority because many other types of negatively charged species play important roles as well and are more reactive. Calculations of anions, in the ground state or in an excited state, with standard quantum chemical software pose no fundamental problems. Technically, rather large basis sets with small exponents are necessary because the charge extends to regions outside the molecule. For accurate calculations of certain properties, for example, for exact polarizabilities, it is necessary to augment the standard basis sets with auxiliary functions with small exponents. These exponents are often made up from a geometrical series  $\zeta_n = d \zeta_{n-1}$  with  $d < 1$ . Five basis functions with  $d = 0.1$  would be typical.

**Dipole-Bound States.** A molecule with a dipole moment larger than about 2 Debye can store a slow electron in a stable, dipole-bound state (DBS). The dipole-bound electron is essentially in a nonbonding orbital. The equilibrium structures of a neutral molecule and a dipole-bound anion are very similar (at least this is normally assumed) and to a good approximation their potential energy surfaces are shifted with respect to each other by a constant energy. Since an incoming electron is often first captured in a dipole-bound state, such anions are often doorways to dissociative electron attachment or other processes (Sommerfeld, 2005). Even for higher-energy situations where the electron is not residing for an extended time in a dipole-bound state, the concept can be useful in the sense of an “antenna” for electrons that are then channeled into other molecular orbitals (Sommerfeld, 2004). The calculation of dipole-bound states with standard quantum chemical software poses in principle no

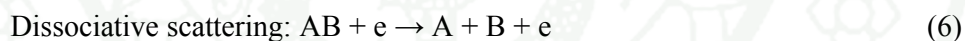
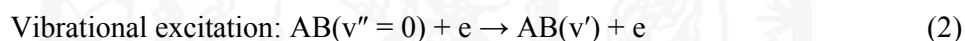
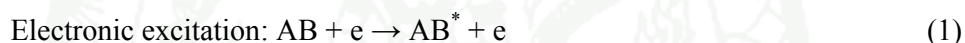
problem beyond the ones encountered for valence anions. A few technical aspects are, however, to be considered. Normal basis sets have basis functions at the positions of the atoms. For dipole-bound states, in addition to the requirement of small exponents, only very large basis sets and/or basis sets centered near the region of the dipole-bound electron which is in the region of the positive end of molecular dipole moment can describe its wave function or charge density flexibly and accurately. This sometimes poses numerical problems to the computer codes. The basis functions are nearly linearly dependent, which can lead to numerical instabilities in the matrix algebra used for finding the eigenvectors and eigenvalues of the states. Care must be taken, therefore, to use stringent threshold criteria, smaller than normal cutoff values, and generally the best possible numerical precision.

A dipole-bound state can sometimes be calculated by uncorrelated methods. In case of an electron bound to an open-shell molecule, however, often the energy of the system is not very accurately described by the electron-static multipole interaction. In these cases the wave function is more complicated since the so-called electron correlation energy becomes important. Appropriate methods like multi-configurational self-consistent field (MC-SCF) (where several Hartree-Fock-type wave functions are simultaneously optimized) are required to treat such systems accurately (Kalcher, 2001).

**Temporary Bound Anions** are not uncommon. Even if the attachment of an electron to a molecule is thermodynamically unstable, metastable anions can live for a long time. Such states are called resonances. The energy of resonances is higher than the fragmentation or dissociation threshold of the system, so they are thermodynamically unstable and will finally decay. Traditionally, **one** distinguishes Feshbach resonances (named after Herman Feshbach, an American physicist) and shape resonances. Both types of resonances are in principle easy to understand; Feshbach resonances are states of the system that would be stable if the fragmentation channel is closed. Feshbach resonances are similar to stable states. For example, a rare gas atom and a diatomic molecule can form a stable van der Waals complex. If, however, the diatomic molecule is vibrationally excited, coupling between the degrees

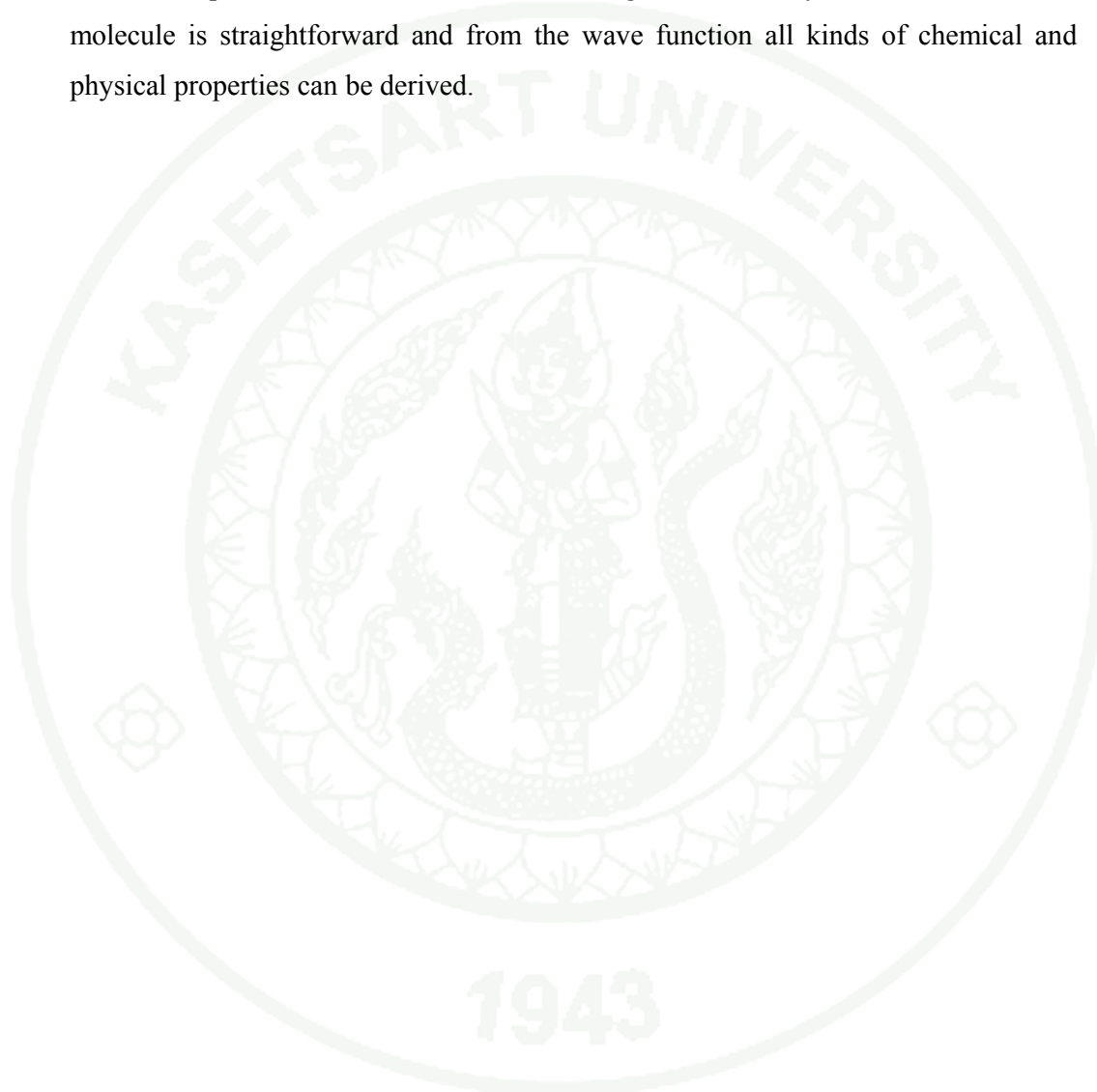
of freedom corresponding to the movement of the rare gas atom and the vibrations of the diatomic (normally more energy is stored in these than in the weak rare gas-molecule interaction) “switches” this bound state into a Feshbach resonance and is responsible for its finite lifetime. A typical shape resonance is the attachment of an electron to a valence orbital yielding an unbound state. Shape-type resonances are associated with **most** unoccupied orbitals of small molecules at their respective equilibrium structures because anion formation in general strongly changes the molecular geometry and symmetry.

For low energies some of the processes that can occur if an electron collides with a molecule are given below:



In (1) the energy of the incoming electron is used to promote an electron of AB into a formerly unoccupied molecular orbital, thus changing the overall electronic quantum numbers. In (2) the molecule uses this energy to move from the vibrational ground state to a higher vibrational state. In (3) the same change as in (2) happens to the rotational instead of the vibrational quantum number. Rotational excitations require much less energy than vibrations and (2) and (3) can happen simultaneously. Process (4) is perhaps the most interesting one. Anions have a very different potential energy surface from neutral systems and a complicated one, and therefore the attachment of an electron triggers dissociation (or other) reactions and this is further modulated by the electron energy. Process (5) occurs if there is no way to internally use the electron energy, and processes like (6) are omnipresent where electrons of suitably high energy destroy molecules on impact.

It is, therefore, very important to be able to calculate what electrons are doing in molecules, and a great amount of effort has been used towards this goal. This has led to the present situation where calculating the stationary wave function of a molecule is straightforward and from the wave function all kinds of chemical and physical properties can be derived.



**CURRICULUM VITAE**

**NAME** : Miss Natcha Injan

**BIRTH DATE** : December 9, 1979

**BIRTH PLACE** : Phetchabun, Thailand

**NATIONALITY** : Thai

**EDUCATION** :

1998 – 2002 Chiang Mai University, B.Sc. (Chemistry)

**SCHOLARSHIPS / AWARDS:**

1. The Commission on Higher Education, CHE (the University Development Commission, UDC)
2. The National Science and Technology Development Agency (NSTDA Chair Professor and NANOTEC Center of Excellence)
3. National Center of Excellence for Petroleum, Petrochemicals and Advanced Materials, NCE-PPAM
4. The Thailand Research Fund, TRF
5. The Kasetsart University Research and Development Institute, KURDI (Center of Nanotechnology)
6. The Graduate School of Kasetsart University

**PUBLICATIONS:**

- 1. Pyridine adsorbed on H-faujasite zeolite: The electrostatic effect of the infinite crystal lattice calculated from a point charge representation.**  
Natcha Injan; Narong Pannorad; Michael Probst, and Jumras Limtrakul.  
*International Journal of Quantum Chemistry* 105 (2005) 898-905.
- 2. Influence of functional groups on the site-selective dissociation of adenine upon low-energy electron.**  
Stephan Denifl, Philipp Sulzer, Dieter Huber, Fabio Zappa, Michael Probst, Tilmann D. Märk, Paul Scheier, Natcha Injan, Jumras Limtrakul, Robert Abouaf, and Henri Dunet. *Angewandte Chemie International Edition* 46 (2007) 5238-5241.
- 3. Calculation of processes relevant to reactions between nucleic acids and free electrons.**  
Michael Probst, Natcha Injan, Stephan Denifl, Fabio Zappa, Ingo Maehr, Manuel Beikircher, Sylwia Ptasinska, Jumras Limtrakul, Tilmann D Maerk, Andreas Mauracher, and Paul Scheier. *Chemical Engineering Communications* 195 (2008) 1371-1381.
- 4. Metastable dissociation of anions formed by electron attachment.**  
Fabio Zappa, Manuel Beikircher, Andreas Mauracher, Stephan Denifl, Michael Probst, Natcha Injan, Jumras Limtrakul, Arntraud Bacher, Olof Echt, Tilmann D. Mark, Paul Scheier, Thomas A. Field, and Karola Graupner.  
*ChemPhysChem* 9 (2008) 607-611.
- 5. Potential energy surface and molecular dynamics simulation of gold(I) in liquid nitromethane.**  
Natcha Injan, Tünde Megyes, Tamas Radnai, Imre Bako and Szabolcz Balint, Jumras Limtrakul, Daniel Spangberg, and Michael Probst. *Journal of Molecular Liquids* 147 (2009) 64-70.

**CONFERENCES / WORK SHOPS:**

- 1. QM/MM investigation of adsorption of benzene and toluene over alkali-exchanged Faujasite zeolite.**

Natcha Injan, and Jumras Limtrakul. The 227<sup>th</sup> ACS National Meeting, Anaheim, CA, United States, March 28 - April 1, 2004. (Poster Presentation)

- 2. ONIOM study of partial oxidation of methane to methanol on Co-ZSM-5 and Fe-ZSM-5 nanoporous catalysts.**

Natcha Injan, Suwat Pabchada, Boonruen Sunphet, and Jumras Limtrakul. The 229<sup>th</sup> ACS National Meeting, San Diego, CA, United States, March 13-17, 2005. (Poster Presentation)

- 3. Pyridine adsorbed on H-faujasite zeolite: The electrostatic effect of the infinite crystal lattice calculated from point charge representation.**

Natcha Injan, Narong Pannorad, Michael Probst, and Jumras Limtrakul. The 231<sup>st</sup> ACS National Meeting, Atlanta, GA, United States, March 26-30, 2006. (Poster Presentation)

- 4. Energetics and geometries of nucleic acid base pairs in the gas phase and in liquid helium.**

Natcha Injan, Michael Probst, Stephan Denifl, Fabio Zappa, Ingo Mähr, Manuel Beikircher, Sylwia Ptasińska, Jumras Limtrakul, Tilmann D. Märk, and Paul Scheier. The 47<sup>th</sup> Sanibel Symposium, St. Simons Island, Georgia, United States, February 22-27, 2007. (Poster Presentation)

- 5. Quantum chemistry of dissociative electron attachment to adenine.**

Michael Probst, Natcha Injan, Stephan Denifl, Fabio Zappa, Jumras Limtrakul, Tilmann Märk, Paul Scheier, Jan Urban, and Pavel Mach. The 47<sup>th</sup> Sanibel Symposium, St. Simons Island, Georgia, United States, February 22-27, 2007. (Poster Presentation)

- 6. Interaction of gold(I) and chloride(I) ions with nitromethane.**

Natcha Injan, Michael Probst, Jumras Limtrakul, Tünde Megyes, Imre Bako, Tamas Radnai, and Szabolcz Balint. The First Thailand National Nanotechnology Conference on Nanomaterials, Pharmaceuticals, Devices and Applications, Chiang Mai, Thailand, August 14-16, 2007. (Oral Presentation)